

LEIBNIZ UNIVERSITY HANNOVER

INSTITUTE OF PHOTOGRAMMETRY AND GEOINFORMATION



MASTER THESIS

Exploring Thermal Anomalies around Salt Diapirs by Satellite Observations

Author:

Swarnalatha Pasam

Matr.Nr: 10013380

Examiners:

Prof. Dr-Ing. Habil. Christian Heipke

Dr. Ing. Sanaz Vajedian

HANNOVER, DECEMBER 2020

STATEMENT OF AUTHORSHIP

Hereby, I declare that the work presented in this dissertation report entitled "Exploration of thermal anomalies around salt diapirs using Satellite observations", submitted to IPI institute, Leibniz University Hannover, for the award of the degree, Master of Science in Geodesy and Geoinformatics is my original work. Any references to previous or external works have been clearly stated and no further sources except those already mentioned were used. I state that this thesis with the same or similar form has not been admitted to any examination board before.

Hannover, 15/12/2020

Swarnalatha Pasam

Abstract:

Southwest edges of the Zagros Mountains are located in Iran and include salt domes with thick layers of halite minerals accumulated in closed basins. These are the important sources for oil exploration but the impermeable salt frequently traps petroleum beneath other rock layers which puts it at the risk from future oil exploration.

Land Surface Temperature (LST) is an essential factor in analyzing thermal variations, global climate changes, hydrological and agricultural processes, and urban land use/land cover. LST has been used in this study to detect temperature anomalies caused by the high thermal conductivity of salt. The strong thermal conductivity between salt and surrounding sediments sometimes can result in higher heat fluxes through salt diapirs and thus increased temperatures above salt domes which could cause the movement of salt glaciers at the surface. The movement of the salt flow occurs at nearly normal temperatures and leads to deformations because of the arid temperature at the salt glaciers of Iran.

This research presents an algorithm to retrieve LST from Landsat-8 Level-1 products using the thermal infrared sensor band 10. Many formulas and methods are considered that successfully estimate the LST to help us study the thermal variations. Along with LST from Landsat-8, MODIS daily LST and Sentinel-3 daily and 10-day LST products are also processed to find the thermal anomalies of the study area. For all these three satellite observations, the data is collected from March, 2017 to January, 2020. For each of the satellite products, the information of Longitude, latitude and LST are extracted and a multi temporal analysis is performed to analyze time series of LST anomalous changes. In addition to multi temporal analysis, the velocity of temperature change is calculated using the linear regression fit on the time series. Since three different satellite observations are processed to produce LST maps with different spatial, temporal resolutions, a data integration method based on Band pass decomposition is developed by passing band passed images to combine the different data using the filtering techniques and to improve the accuracy of LST calculated from Landsat-8.

Apart from using the Optical sensors to detect thermal variations, InSAR processing is done using the SAR images acquired from Sentinel-1 to interpret the deformation analysis. For processing S-1 images and generating interferograms, GMTSAR is used. And finally, InSAR time series analysis is performed by The Small baseline Subset Interferometry (SBAS) to monitor the deformation caused by the salt flow as a result of temperature change most of the time at the study area.

Table of Contents

List of Abbreviations	5
List of Symbols	8
1. Introduction:	9
1.1 Motivation:	11
1.2 Achievements:	12
2. Study Area:	13
2.1 Examples of Salt domes from Zagros Mountain:.....	14
2.1.1 Salt domes in the Zagros Mountain:	14
2.1.2 Jashak salt dome, Iran:	15
2.1.3: A close view of Jashak salt dome, Iran	15
2.2 Geological characteristics:	16
2.3 Climate:	18
3. Satellite Data:	19
3.1 Optical Data:	19
3.1.1 Landsat-8:	19
3.1.2 Sentinel-3:	24
3.1.3 Moderate Resolution Imaging Spectroradiometer (MODIS):.....	27
3.2 Radar Data:	33
3.2.1 Sentinel-1:	33
4. Methodologies:	34
4.1 Land Surface Temperature:	34
4.1.1 Data for LST retrieval:.....	35
4.1.2 Land Surface Temperature Calculation flowchart:	36
4.1.3 Procedure for LST estimation:	38
4.1.4 Challenges in LST retrieval:	43

4.2 Band Pass Decomposition:	44
4.3 InSAR time series analysis:	47
5. Results and Discussion	50
5.1 LST Results from LANDSAT-8 Data:	50
5.1.1 Calculation of TOA (Top of Atmospheric) reflectance:	50
5.1.2 Converting TOA to Brightness Temperature:	51
5.1.3 Estimated Land Surface Reflectance (LSR) for NDVI:	52
5.1.4 Calculated NDVI for emissivity estimation:	53
5.1.5 Estimated Land Surface Emissivity (LSE):	54
5.1.6 Land Surface Temperature:	55
5.2 Generation of LST maps:	55
5.2.1 LST maps from Landsat-8:	56
5.2.2 LST maps from MODIS data:	56
5.2.3 LST maps from Sentinel-3 data:	57
5.3 Time series analysis of generated LST maps:	59
5.3.1 Time series analysis of Landsat-8 LST maps:	59
5.3.2 Time series analysis of MODIS LST maps:	61
5.3.3 Time series analysis of Sentinel data:	63
5.4 Velocity of Temperature changes from MODIS and Sentinel-3:	69
5.5 Bias between Landsat-8 and MODIS:	70
5.6 Band pass decomposition:	72
5.6.1 Corrected LST Map	73
5.6.2 Corrected Velocity Map	73
5.6.3 Corrected Time series plots	75
5.7 InSAR time series:	76
5.7.1 SBAS time series of Deformation maps:	76
5.7.2 Velocity map:	77
5.7.3 Time series maps:	78
6. Conclusion:	79
7. Appendix:	81

7.1 Landsat Missions:	81
7.2 Sentinel Missions:	82
7.3 Sentinel-3 Instruments:	84
7.4 InSAR:	86
References:.....	91

List of Abbreviations

LST	Land Surface Temperature
MODIS	Moderate Resolution Imaging Spectro radiometer
NASA	National Aeronautics and Space Administration
ERTS	Earth Resources Technology Satellite
RBV	Return Beam Vidicon
MSS	Multi Spectral Systems
VHF	Very High Frequency
WRS	Worldwide Reference System
FOV	Field Of View
TM	Thematic Mapper
SLC	Scan Line Corrector
USGS	United States Geological Survey
OLI	Operational Land Imager
TIRS	Thermal Infrared Sensors
CCSDS	Consultative Committee for Space Data Systems
ESA	European Space Agency
AHr	Ampere Hour
NiH₂	Nickel Hydrogen
GSFC	Goddard Space Flight Centre
GMES	Global Monitoring for Environment and Security
EEA	European Environment Agency
CAMS	Copernicus Atmosphere Monitoring Service

HCHO	Formaldehyde
CHOCHO	Glyoxal
OLCI	Ocean and Land Colour Instrument
SLSTR	Sea and Land Surface Temperature Radiometer
SSP	Spatial Sampling Protocol
VIS	Visible Infrared Spectrum
SWIR	Short Wavelength Infrared
MWIR	Medium Wavelength Infrared
SAR	Synthetic Aperture Radar
InSAR	Interferometric Synthetic Aperture Radar
SRAL	SAR Radar Altimeter
DPU	Digital Processing Unit
RFU	Radio Frequency Unit
LRM	Low Resolution Mode
DEM	Digital Elevation Model
MWR	Micro Wave Radiometer
PDGS	Payload Data Ground Segment
GNSS	Global Navigation Satellite Systems
LRR	Laser Retro Reflector
EOS	Earth Observing Systems
TES	Temperature Emissivity Separation
ASTER	Advanced Spaceborne Thermal Emission and Reflection Radiometer
WVS	Water Vapour Scaling
CMG	Climate Modelling Grid
QC	Quality Control

SDS	Scientific Data Sets
ECV	Essential Climate Variables
LSE	Land Surface Emissivity
RTE	Radiative Transfer Equation
GCP	Ground Control Point
DN	Digital Number
TIFF	Tagged Image Format File
NDVI	Normalized Difference Vegetation Index
TOA	Top Of Atmosphere reflectance
BT	Brightness Temperature
LSR	Land Surface Reflectance
FFT	Fast Fourier Transform

List of Symbols

L_{λ}	TOA spectral radiance
M_L	Band-specific multiplicative rescaling factor from the metadata
A_L	Band-specific additive rescaling factor from the metadata
Q_{cal}	Quantized and calibrated standard product pixel values (DN)
T_B	Top of atmosphere brightness temperature
K_1	Band-specific thermal conversion constant from the metadata
K_2	Band-specific thermal conversion constant from the metadata
Q_{red}	Reflectivity in the red channel
a, b	Channel dependent regression coefficients
$\epsilon_{v,i}$	Vegetation emissivity at wavelength λ
$\epsilon_{s,i}$	Soil emissivity at wavelength λ
P_v	Fraction of vegetation
C_i	Surface roughness
F	Geometric Factor
σ	Boltzmann constant
h	Planck's constant
c	Velocity of light

1. Introduction:

The Land Surface Temperature (LST) is the radiative skin temperature of the land surface, as measured in the direction of the remote sensor (sentinel.esa.int). It is a fundamental aspect of climate and biology, affecting organisms and ecosystems from local to global scales. LST is identified as one of the most important Earth System Data Records by NASA and other international organizations (King, 1999). LST measures the emission of thermal radiance from the land surface where the incoming solar energy interacts with and heats the ground, or the surface of the canopy in vegetated areas. This quality makes LST a good indicator of energy partitioning at the land surface-atmosphere boundary and sensitive to changing surface conditions (Nemani et al., 1996; Wan et al., 2004; Lambin and Ehrlich, 1995; Mildrexler et al., 2009).

The temperature increase in Salt glaciers has the potential to dramatically alter the generation, movement, accumulation, and preservation of hydrocarbons and other fluids in the vicinity of salt structures. These fluid related processes alters the distribution in the salt structures and surrounding rocks, creating a complex feedback system amongst the evolving salt structure, the temperatures in the enveloping rocks, and the nearby fluid system (Cedeño, 2019). In early studies, the thermal effects of salt diapirs were modeled as perfectly cylindrical structures in a homogenous and isotropic sedimentary medium (M. Pollyea, 2018).

In this study, the exploration of thermal anomalies has been done using LST around the salt domes/diapirs because of the high thermal conductivity of salt. The strong thermal conductivity contrasts between salt rocks and the surrounding sediments result in higher heat fluxes through salt diapirs which thus impacts the thermal anomalies. This leads to increase in temperatures above salt domes, creating what has become known as the Salt Glaciers at the earth's surface (Jensen, 1983).

The LST retrieval from Landsat-8 Level-1 products is calculated using the Thermal Infrared Sensors (TIRS). TIRS is the newest thermal infrared sensor for the Landsat project, providing two adjacent thermal bands, which has a great benefit for the LST inversion. The data from Landsat -8 has been improved by series corrections and data reprocessing steps. The corrections include the improvement of radiance

conversion coefficients, calibration parameters for OLI bands and improvement in the radiometric offset coefficients for TIRS bands. The procedure for LST calculation is long but many algorithms are available. The technique used here for LST retrieval is taken from Ugur Avdan et al., 2016. It uses Brightness temperature from TIRS (band 10 or 11) and NDVI (band 4 and 5) from OLI bands. In particular, band 4 (Red wavelength/micrometers, 0.64–0.67) and 5 (near infrared (NIR) wavelength/micrometers, 0.85–0.88) and band 10 (thermal infrared sensor (TIRS) wavelength/micrometers, 10.60–11.19) was used as band 11 has larger calibration unreliability according to Landsat 8 User Hand book of USGS.

Along with LST from Landsat-8, MODIS daily global LST product with temperature values at 0.05 degree latitude/longitude climate model grids (CMG) and Sentinel-3 global LST with 5km spatial resolution are also processed for thermal variation analysis by generating LST maps for each date separately. For all these satellite observations, multi temporal time series analysis was performed from March, 2017 to March, 2020 to detect the trend of temperature variation and interactions in the long term. In addition to time series analysis, velocity maps and velocity profiles are also calculated for MODIS and Sentinel-3 to find the change in temperature using the linear regression fit. Since the high temperature causes salt flow at the surface, deformation analysis is also performed using SAR data (Sentinel-1). InSAR time series analysis is an effective tool to monitor the displacement of the earth's surface over a period of time.

Landsat TM/ETM+ thermal imagery provides spatial resolutions sufficient to map LST at fine scales (~100 m) but has a long repeat cycle of 16 days. For a good spatial resolution, even a small feature should be detected by the sensor in the satellite whereas temporal resolution is related to the time period between the images. Continuous monitoring efforts from Landsat-8 are further limited by cloud cover during times of image acquisition. MODIS LST products from NASA's Terra/Aqua platforms are available daily, with enhancing temporal sampling of temperature distributions, but are restricted to coarse spatial resolutions (~1 km). Although sentinel-3 has a great temporal resolution, it is limited by the coarse resolution of 5km.

As the aim of this study is to analyze the thermal anomalies using different satellite observations, a data integration method using band pass decomposition is developed to combine MODIS data and Landsat-8 data. As the study area is small covering only 30 to 35 kilometers, Sentinel-3 data with coarse resolution was not good enough to proceed for band pass decomposition because of the data gaps

present. In band pass decomposition, a series of band passed images with Gaussian filters have been generated for separately for Landsat-8 and MODIS data and combined with the band pass components. It is a type of method to enhance the accuracy of remotely-sensed imagery commonly by regression-type approaches.

Landsat, MODIS and Sentinel-3 SLSTR which have been used to observe thermal variations are optical products offered from Optical remote sensing. In the other hand, the Sentinel-1 data which has been used for the InSAR processing to observe the deformation analysis over the time is from Radar remote sensing. SAR data is acquired regardless of the weather condition and has active sensors which use their own energy to send signals to make the observations on the other hand; optical sensors depend on weather conditions and cannot take measurements during nights. Consequently, the weather needs to be free of clouds. SAR uses a wavelength of 1 cm to 1 m, while optical sensors use wavelengths near that of visible light, or 1 micron which makes it able to acquire images in various wavelength bands.

1.1 Motivation:

Salt diapirs began attracting serious scientific attention in the early part of the 20th century, mainly as a relevance to the petroleum industry. In the southern part of the Zagros Mountains alone, there are more than 130 salt domes which affected the structure of Zagros Mountains as one of the most significant simple folded systems in the world. All these salt structures cause anomalous temperature distributions throughout many sedimentary basins due to the 2 or 3 times higher thermal conductivity of salt as compared to other sedimentary rocks which result in increased temperatures above salt domes (Jensen, 1983).

Salt structures and their related mini basins are associated with complex and evolving fluid systems that reflect their structural and stratigraphic evolution. As salt has low viscosity and low density, they become easily ductile and mobile which causes the geological deformation (Frank J. Peel, 2014). For salt movement to start a sufficient load pressure is required to cause flow deformation of the salt and a disturbance is required to trigger the diapiric process. These disturbances or loads are often caused by tectonic events, for example folding or faulting that displaces one salt region relative to another, or by a thermal variations.

The earlier research work from Selig and Wallick, 1966, also states that thermal anomalies are present above, around, and below salt diapirs. An accurate understanding of these changes due to thermal anomalies is important for petroleum

and gas explorations, specifically how it suppresses the maturation of petroleum source rocks.

Once these salt domes break through the surface, it produces flowing glaciers of salt. The arid climate does not produce enough rain to dissolve the salt and carry it away which puts the salt domes at risk from future oil and natural gas exploration, as the impermeable rocks found in salt domes frequently trap petroleum and hydrocarbons beneath other rock layers (amusing.com). Salt domes in other regions, such as in the United States, Mexico, the North Sea in Germany and Romania are already significant sources of petroleum and has been trapped for many years now (britannica.com, amusing.com). For all these mentioned reasons, monitoring and detecting the thermal variations in this area is crucial. Making use of the available satellite observations with high spatial, temporal resolutions, it makes us much easier to continuously monitor them for long period of time.

1.2 Achievements:

To analyse the thermal anomalies and to monitor the deformation of a salt dome in the study area, many results have been achieved and are listed below.

- LST retrieval from Landsat-8 level-1 datasets.
- LST maps generation based on available optical satellite data (Landsat-8, MODIS, Sentinel-3 SLSTR) for three continuous years.
- Time series analysis of multi temporal LST maps to analyse thermal variation over the time separately for each satellite observation.
- Data integration of LST maps using Band pass decomposition from Landsat-8 and MODIS daily data.
- Deformation monitoring based on InSAR time series analysis

2. Study Area:

The study area is a salt dome which is located in the southwest part of Zagros Mountain, Iran. It is limited by coordinates: $27^{\circ} 85'-28^{\circ} 18'$ N and $54^{\circ} 80'-55^{\circ} 10'$. Figure (1) and Figure (2) represent the study area in close view. This area includes Zagros orogeny belt and Persian Gulf which have been formed on the north eastern part of Arabian plate (Razaghian, G, 2015). The folds on the Gulf coast form the foothills of the Zagros Mountains, which run north-north-westerly through Iran, and were formed when the Arabian shield butted up against the western Asian continental mass, the collision taking place only 5–10 million years ago (ipi.usra.edu).

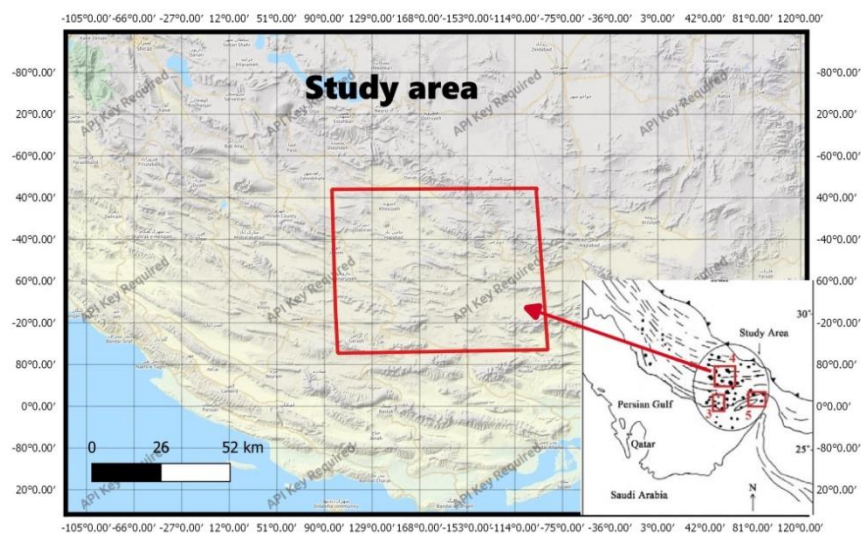


Figure (1): Study area



Figure (2): Study area in close view (Credit: amusingplanet.com)

2.1 Examples of Salt domes from Zagros Mountain:

To get the clear idea of how salt domes and salt glaciers look, some examples are presented here from the southwest part of Zagros Mountain.



Figure (3): Different Salt diapirs (1: Kalat, 2: Charak, 3: Darbast, 4: Bastak) on the plunging noses of charak, Gezzeh and Nakh anticlines around the study area (Razaghian, G, 2015).

2.1.1 Salt domes in the Zagros Mountain:

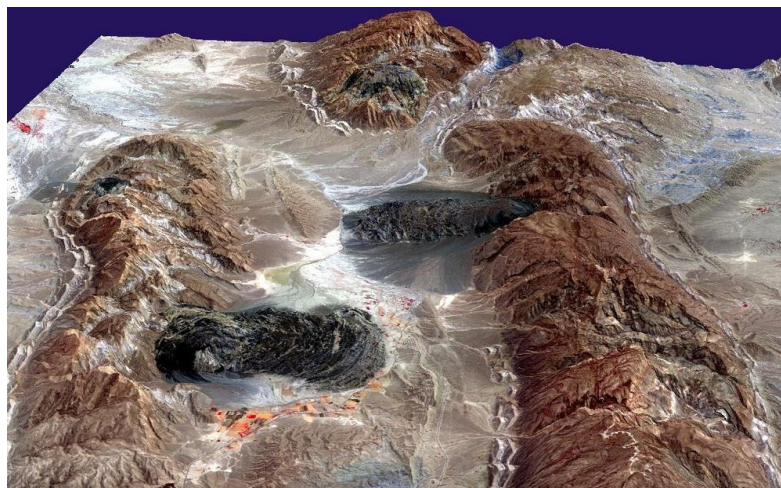


Figure (4): Salt domes (hills) and salt glaciers (dark areas) in the Zagros Mountains (Credit: amusingplanet.com)

2.1.2 Jashak salt dome, Iran:



Figure (5): Salt dome in Jashak, Iran (Credit: amusingplanet.com)

2.1.3: A close view of Jashak salt dome, Iran



Figure (6): A close view of Jashak salt dome, Iran (Credit: amusingplanet.com)

2.2 Geological characteristics:

Geological exploration started when the collision of the sedimentary rocks caused stress in the earth's crust but the erosion removed softer rocks, like mudstone which forms from the consolidated mud and siltstone which slightly coarser than the mudstone while leaving harder rocks such as limestone and dolomite, which contains calcium and magnesium. This differential erosion formed the ridges of the Zagros Mountains. The ridges and valleys on the Zagros Mountains extend hundreds of kilometers (earthobservatory.nasa). Thick layers of minerals such as halite (general table salt) accumulate in closed basins during alternating wet and dry climatic conditions and form Salt domes over geologic time, these layers of salt are buried under younger layers of rock.

The term salt diapir was introduced by a Romanian geologist Ludovic Mrazek who was the first to understand salt intrusion in plasticity. Salt Diapir is generally one to two kilometers or more in diameter. Salt domes form from the deposits of salt at marine basins because the density of the salt dome is lower than the rocks above it. They penetrate vertically upward along zones of structural weakness through denser overlying rocks because of density contrast between them. This process is called diapirism (lpi.usra.edu).

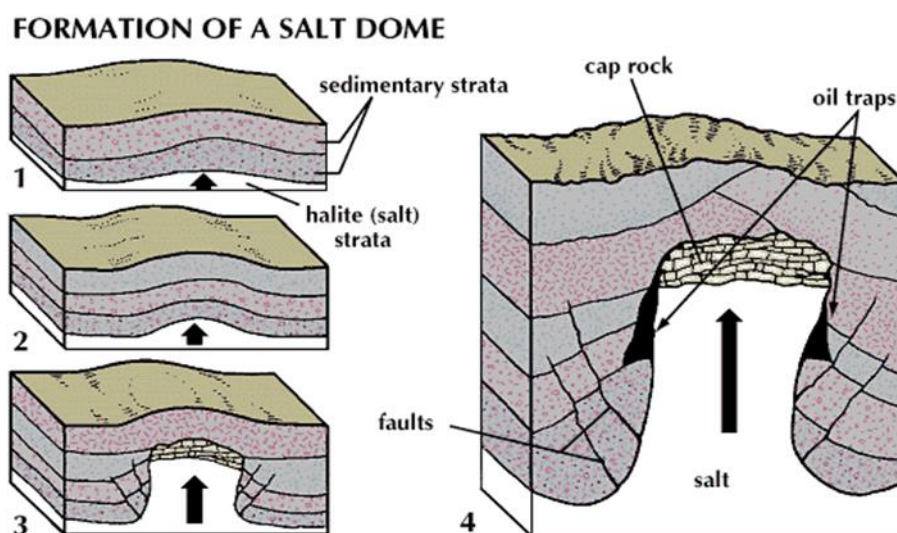


Figure (6): Formation of a Salt dome (Credit: Britannica.com)

Diapirism has three modes which are Reactive, Active and passive diapirism (S. Lord, 2018). The resulting structures from diapirism are called piercement structures. During that process, segments of existing strata can be disconnected and forced upwards. Salt domes also are frequently favourable sites for trapping hydrocarbons.

The three modes of diapirism are 1.Reactive 2.Active and 3.Passive.

Reactive Diapirism:

Salt layer is compressed by the overlain strata of a constant thickness and higher density. This process will not allow a diapir to form until external forces are applied. During the cases of external forces including faulting, uplifting, folding and tectonics, salt will break through and grow to form a diapir (S. Lord, 2018).

Active Diapirism:

Salt layer tends to break through and grow when the overburden is weak and thin (S. Lord, 2018).

Passive Diapirism:

Salt layer breaks through and continues to grow as the surrounding sediments continue to subside until the salt source is depleted. Once the salt source is depleted, the diapir stops growing and is buried by the surrounding sediments (S. Lord, 2018).

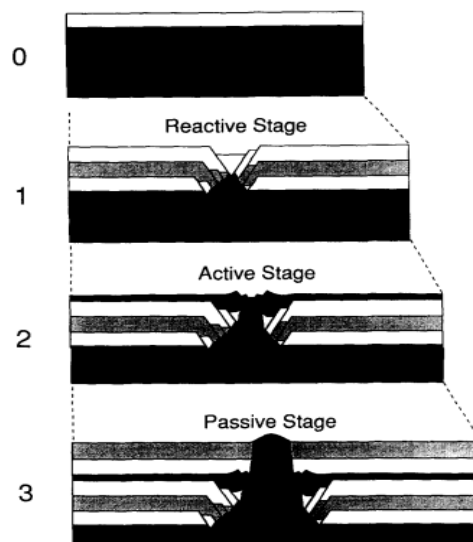


Figure (7): Modes of a salt diapir(S. Lord, 2018).

2.3 Climate:

The climate in this area is arid type. It is usually hot and dry but changes by the mountains to lower temperature and higher rainfall. In summer, the relative air humidity varies from 26 to 98% and annual average precipitation varies from 50 to 350 mm (Bosák, P, 1998). Temperature in this area is very random having the average annual temperature about 27 °C. The coldest month's average temperature being in January and February is about 16 ° C. The warmest months are July and August with temperatures about 36 °C. Some days of these months have more than 50°C(Bosák,P.1998).

3. Satellite Data:

3.1 Optical Data:

Optical remote sensing has been offering data for over four decades, providing consistent datasets with ease of availability. Optical products are commonly available as multispectral images (ranging from visible to infrared wavelengths) consisting of several bands of data, which can offer different information on land properties based on its spectral reflectance, as well as be used to check land cover through various indices like NDVI (Joshi, 2016). Spectral resolution is related to the Electromagnetic (EM) spectrum. A good spectral sensor has the ability to measure specific wavelengths in the EM spectrum. A multi spectral sensor with more than 100 bands has more spectral resolution than Landsat 8 with 11 bands. Making use of the optical data with high temporal resolution (e.g., Landsat, MODIS), performing a dense time series has an advantage of being able to capture both highly dynamic and gradual or long-term change processes, as well as overcoming gaps due to cloud cover. In this study, Landsat-8, MODIS and sentinel-3 datasets, which are all Optical datasets, have been used for the processing of LST. The following sections explain about the each satellite mission in detail (Joshi, 2016).

3.1.1 Landsat-8:

Landsat 8 was launched on February 11, 2013. It was developed jointly by NASA and the U.S Geological Survey (USGS). It is designed for a lifetime of five years and carries fuel for 10 years. The payload of Landsat 8 consists of two instruments (imaging sensors) – The Operational Land Imager (OLI) and Thermal Infrared Sensors (TIRS) as seen from Figure (9) and Figure (10). More details about this mission is explained in this section below as Landsat-8 data is used for the LST retrieval and processing.

There are eight Landsat satellite missions and the ninth one is going to be launched in the middle of 2021. A detailed explanation of all the Landsat missions is given in the section 7.1. With the goal to develop a first civilian satellite, The Department of the Interior, NASA, and the Department of Agriculture has decided to launch the Earth Resources Technology Satellite (ERTS-1) in 1972. This was later renamed as Landsat-1 satellite. This mission has collected the data on the forests, farms and

urban areas. Landsat satellites as earth observation satellites are continually providing the data related to earth's land surface from monitoring the Antarctic glaciers to monitoring deforestation (usgs.gov). Data products for all the Landsat satellites are available to download freely on Earthexplorer, Glovis, LandsatLook Viewer. Figure (8) shows from when to when, the Landsat missions have provided the data.

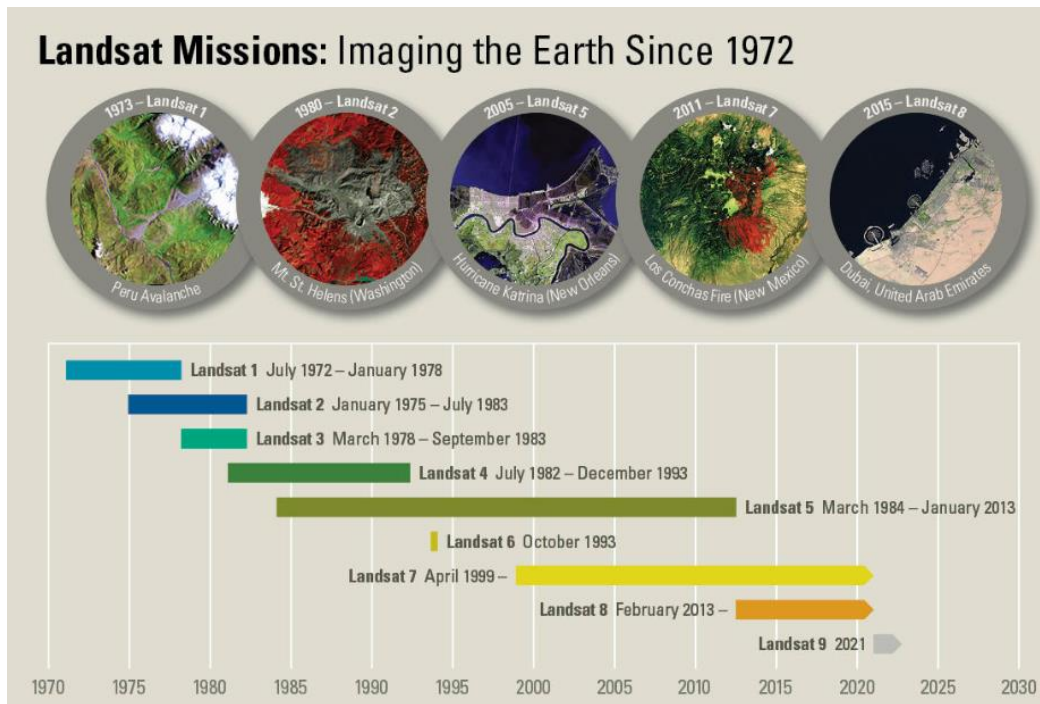


Figure (8): Landsat satellite missions since 1972 (Credit: usgs.gov)

Landsat 8 and its payloads:

The payload of Landsat 8 consists of two instruments (imaging sensors) – The Operational Land Imager (OLI) and Thermal Infrared Sensors (TIRS). Whereas the previous Landsat instruments use the same image sensor (Thematic Mapper) to acquire both thermal and reflective band images. The OLI, which images in the visible to short-wave infrared (0.4–2.5 μm) portion of the spectrum, and (TIRS), which images in the thermal region (10–12.5 μm). Data access to Landsat 8 is open to worldwide at free of cost. It provides 16 day earth coverage regularly and acquires 725 scenes per day which increases the probability of getting cloud free images. The objective of Landsat 8 is to provide timely, high quality visible and infrared images of all landmass and near-coastal areas on the Earth. It enables the detection and characterization of global land changes (usgs.gov).

Observatory Capabilities:

Scenes/Day	~650
SSR Size	3.14 Terabit, file-based
Sensor Type	Pushbroom (both OLI and TIRS)
Compression	~2:1 Variable Rice Compression
Image D/L	X-Band Earth Coverage
Data Rate	384 Mbits/sec, CCSDS Virtual Channels
Encoding	CCSDS, LDPC FEC
Ranging	GPS
Orbit	705 Km Sun-Sync 98.2° inclination (WRS2)
Crossing Time	~ 10:11 AM

Table (1): Landsat 8 Observatory Capabilities, Credit: usgs.gov

Landsat 8 Spacecraft facts:

state data recorder	3.14 terabit for data downlink
Power	provided by a single 9 x 0.4 meter solar array and one 125 Ampere-Hour (Ahr), Nickel-Hydrogen (NiH2) battery
Weight	2,071 kg (4,566 lbs) fully loaded with fuel (without instruments)
Length	3 m (9.8 ft)
Diameter	2.4 m (7.9 ft)
Data rate	384 Mbps on X-band frequency; 260.92 Mbps on S-band frequency

Table (2): Landsat 8 spacecraft facts, Credit: usgs.gov

Both the Landsat 8 satellite payload sensors, TIRS and OLI are push broom sensors and function simultaneously. However, when either of them doesn't work, they are capable of working independently. Generally, when the spacecraft is integrated with its two different sensors, it is called an Observatory (usgs.gov).

Operational Land Imager (OLI):

OLI was built by the Ball Aerospace & Technologies Corporation and collects images using nine spectral bands with different wavelengths ranging from 0.43 to 1.38 as shown in Table (3). It has over 190 km of wide swath with 30m resolution for all the bands except the panchromatic band (15m) covering the earth's landscape to observe land uses like forests, farms and urban areas with sufficient resolution (usgs.gov).

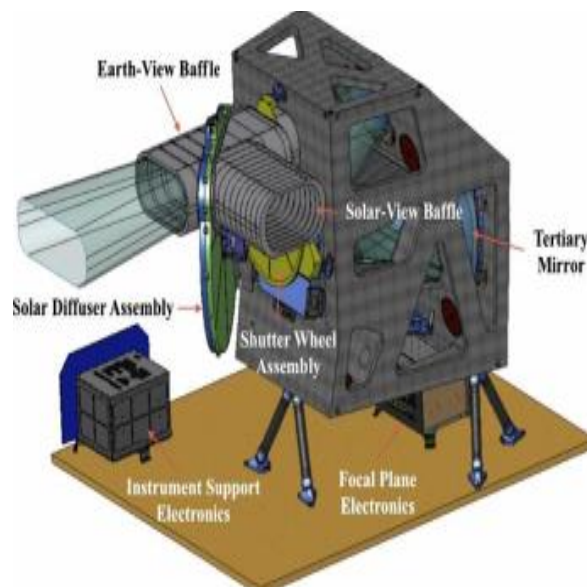


Figure (9): Operational Land Imager (Credit: usgs.gov)

Thermal Infrared Sensors (TIRS) :

TIRS was built by the NASA Goddard Space Flight Centre (GSFC) and has two bands (10 and 11) which collect Land Surface Temperature at 100m resolution with wavelengths from 10.6 to 12.51 but, the products provided are resampled to 30m resolution images. In TIRS bands, the colors of pixels represent information about the kind of temperature. For example, dark pixels represent cool temperatures and light pixels represent hot temperatures. Most importantly, TIRS bands provide the knowledge about water irrigation use in arid lands and heat units in urban areas (usgs.gov).

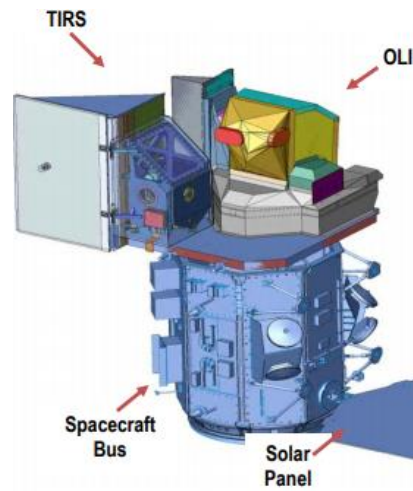


Figure (10): An illustration of Landsat 8 Observatory (Credit: usgs.gov)

Landsat 8 Bands with Wavelength and Resolution:

Bands	Wavelength (micrometers)	Resolution (meters)
Band 1 - Coastal aerosol	0.43-0.45	30
Band 2 - Blue	0.45-0.51	30
Band 3 - Green	0.53-0.59	30
Band 4 - Red	0.64-0.67	30
Band 5 - Near Infrared (NIR)	0.85-0.88	30
Band 6 - SWIR 1	1.57-1.65	30
Band 7 - SWIR 2	2.11-2.29	30
Band 8 - Panchromatic	0.50-0.68	15
Band 9 - Cirrus	1.36-1.38	30
Band 10 - Thermal Infrared (TIRS) 1	10.6-11.19	100
Band 11 - Thermal Infrared (TIRS) 2	11.50-12.51	100

Table (3): Landsat 8 bands with their wavelengths and resolutions

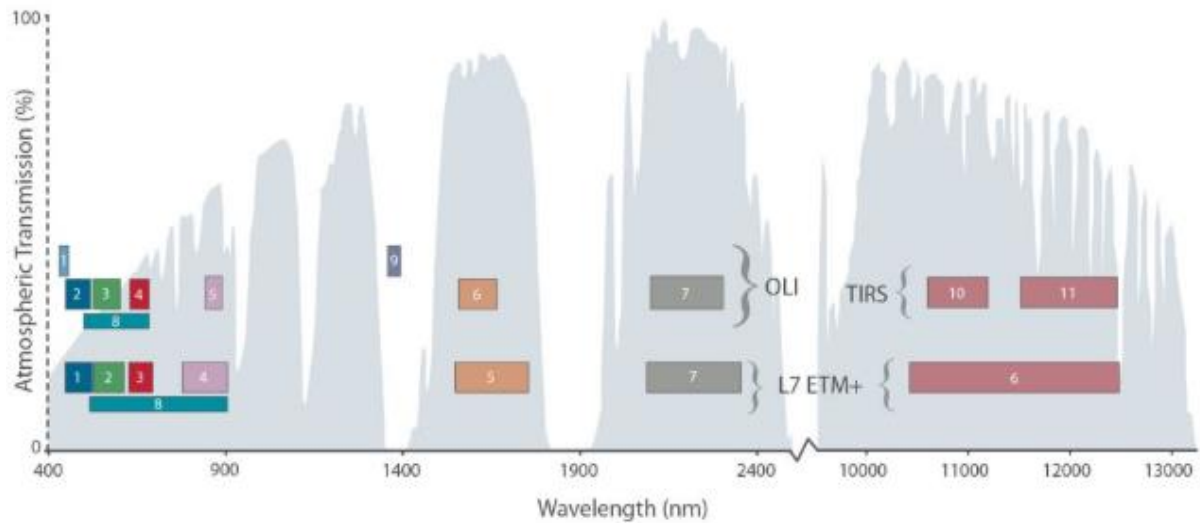


Figure (11): Landsat 8 bands with wavelength (Credit: usgs.gov)

3.1.2 Sentinel-3:

European Space Agency (ESA), on behalf of the Global Monitoring for Environment and Security (GMES) initiative is developing a series of Earth Observation Missions. Sentinel missions are a part of GMES initiative. The aim of the Sentinel missions is to replace the current older Earth observation missions which have reached retirement. Each mission focuses on different aspects like Atmospheric, Oceanic, and Land monitoring of Earth Observation. Unlike Sentinel-1 and Sentinel-2, each Sentinel-3 satellite carries multiple payload instruments for multiple applications. All the sentinel missions are given with explanation in the section 7.2. The objectives of sentinel-3 include: Measuring sea-surface topography, sea-surface height and significant wave height, Measuring ocean and land-surface temperature, Measuring ocean and land-surface colour, Monitoring sea and land ice topography, Sea-water quality and pollution monitoring, Inland water monitoring, including rivers and lakes, Aid Ocean forecasts with acquired data, Climate monitoring and modeling, Land-use change monitoring, Forest cover mapping, Fire detection, Weather forecasting and Measuring Earth's thermal radiation for atmospheric applications (sentinel.esa.int).

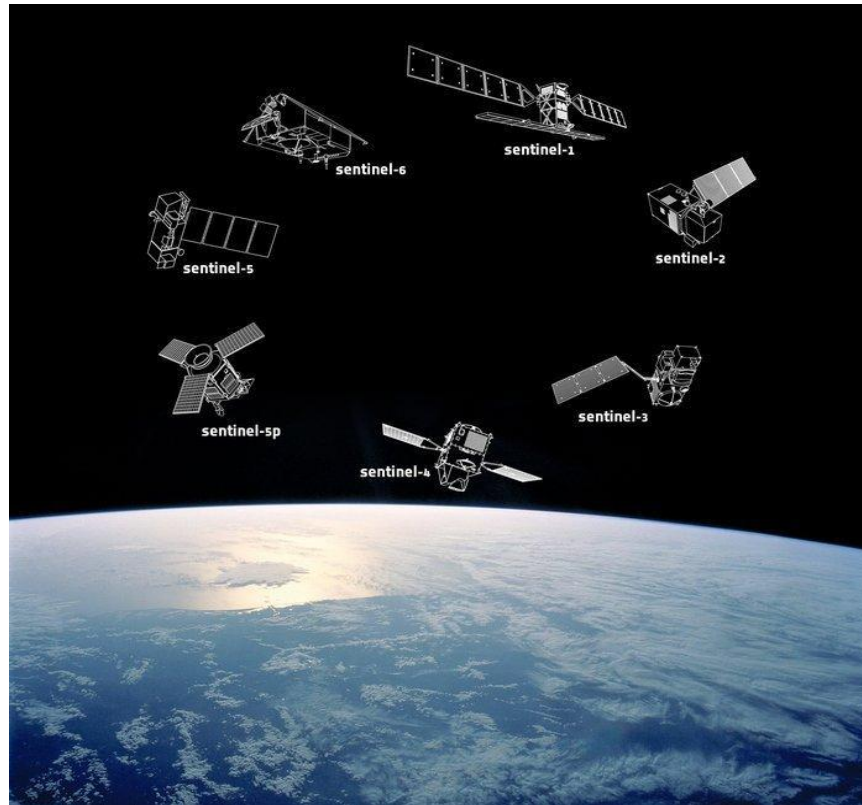


Figure (12): All sentinel missions (Credit: sentinel.esa.int).

Sentinel-3 instruments:

Sentinel-3 is a multi-instrument mission and operated jointly by ESA and UMETSAT to deliver operational ocean and land observation services with an operational life span of seven years. All the instruments of Sentinel-3 are presented with detailed explanation in the section 7.3. It comprises three different satellites (Sentinel-3A, Sentinel-3B and Sentinel-3C). These missions provide continuous data for ESA and ENVISAT and SPOT satellites. The main objective of sentinel-3 is to study sea surface topography, sea and land surface temperature, and ocean and land surface color with high accuracy and reliability to support ocean forecasting systems, environmental monitoring and climate monitoring (sentinel.esa.int). Figure (13) explains all the Sentinel-3 payload instruments and their position on the satellite.

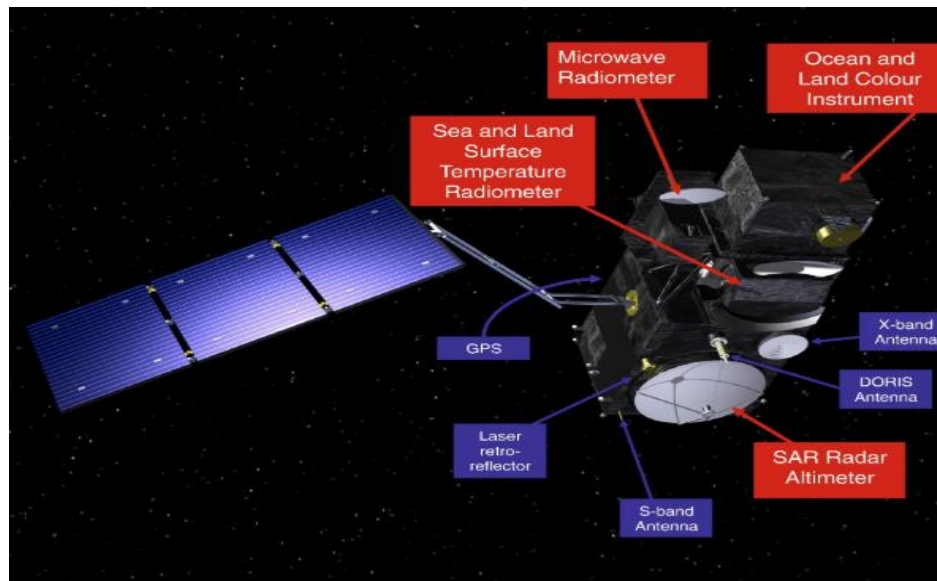


Figure (13): Sentinel-3 payload instruments, (Credit: sentinel.esa.int).

Sea and Land Surface Temperature Radiometer (SLSTR):

The main aim of the SLSTR instrument mission is to provide a reference Land Surface Temperature and Sea Surface Temperature dataset for climate data records. SLSTR has been developed to retrieve global coverage sea surface skin temperatures with zero bias and an uncertainty of ± 0.3 K for a 5° by 5° latitude–longitude area, having a temporal stability of 0.1 K/decade (sentinel.esa.int). It is a conical scanning imaging radiometer employing the along track scanning dual view (near-nadir and backward views) technique. All the technical details of this instrument are given in the below Table (4).

swath width	dual view scan, 1 420 km (nadir) / 750 km (backwards)
spatial sampling	500 m (VIS, SWIR), 1 km (MWIR, TIR)
spectrum	nine bands [0.55-12] μm
noise equivalent	50 mK (TIR) at 270 K
launch mass	90 kg
size	2.116 m ³
design lifetime	7.5 years

Table (4): Main characteristics of the SLSTR

Both SLSTR and OLCI are optical instruments that are used to provide data continuity for ENVISAT's AATSR and MERIS instruments and the swaths of the two instruments overlap, allowing for new combined applications (sentinel.esa.int).

Sentinel data:

Sentinel 3 Land Surface Temperature products are downloaded from Copernicus Global Land Service. It provides four different types of products. They are vegetation state, energy budget, water cycle and cryosphere. The Global Land Service has 3 types of LST collections under energy budget as mentioned below.

LST hourly data and LST 10 day data have been download for the task and processed for time series analysis. As hourly data is so much to process for 3 years, LST-hourly at 5AM data has been used for time series analysis and thermal variation analysis.

- LST: hourly LST from instantaneous observations
- LST10-DC: 10-day Land Surface Temperature with Daily Cycle
- LST10-TCI: Thermal Condition Index with a 10-day composite of Land Surface Temperature.

3.1.3 Moderate Resolution Imaging Spectroradiometer (MODIS):

MODIS is an important instrument onboard the Earth Observing Systems (EOS) Terra (EOS AM-1) and Aqua (EOS PM-1) satellites. Terra was launched on December 18, 1999, and Aqua was launched on May 4, 2002. These are designed to monitor the Earth's atmosphere, Ocean, and land surface with a set of visible, NIR, MIR, and thermal channels. Terra's orbit around the Earth is timed so that it passes from north to south across the equator in the morning, while Aqua passes south to north over the equator in the afternoon. Terra MODIS and Aqua MODIS acquire data in 36 spectral bands ranging in wavelength from 0.4 μm to 14.4 μm . Two bands are imaged at a nominal resolution of 250 m at nadir, with five bands at 500 m, and the remaining 29 bands at 1 km. Terra MODIS and Aqua MODIS have a ± 55 -degree scanning pattern at the EOS orbit of 705 km achieves a 2,330-km swath width and provides global coverage every one to two days. . It helps us to understand the global dynamics and processes occurring on the land, in the oceans, and in the lower atmosphere. MODIS is playing a vital role in the development of validated, global, interactive Earth system models able to predict global change

accurately enough to assist policy makers in making sound decisions concerning the protection of our environment (modis.gsfc.nasa.gov).

MODIS DATA:

There are many MODIS data products which are being used by scientists from a plenty of disciplines, including oceanography, biology, and atmospheric science to study global change. From MODIS Land products, LST products are found in two different forms of MODIS data (MOD11 and MOD21). MODIS Land Surface Temperature and Emissivity, Terra MOD11 and Aqua MYD11 products are used in this task and the other MODIS Land Surface Temperature and Emissivity is Terra MOD21 and Aqua MYD21 products. All the MODIS LST products are produced as a sequence of products through spatial and temporal transformations, to daily, eight-day and monthly global gridded products.

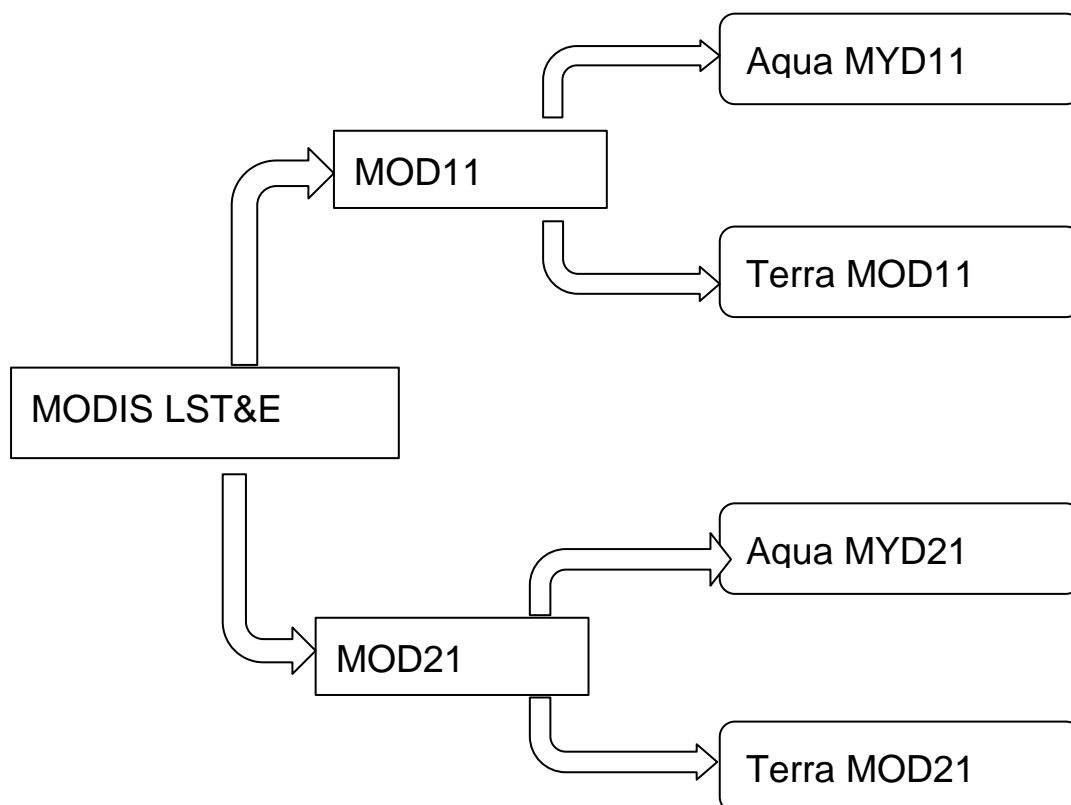


Figure (14): MODIS Land Surface Temperature product types

MOD21 products are based on the physics based algorithm to retrieve LST dynamically for the three MODIS thermal infrared bands (29, 31 and 32) at a spatial resolution of 1 km at nadir. The brief explanation of how the MOD21 algorithm formed is based on the Advanced Spaceborne Thermal Emission and Reflection Radiometer (ASTER) Temperature Emissivity Separation (TES) algorithm.

The algorithm uses full radiative transfer simulations for the atmospheric correction, and an emissivity model based on surface radiance data to retrieve both LST and spectral emissivity. The TES algorithm is combined with an improved Water Vapor Scaling (WVS) atmospheric correction scheme to stabilize the retrieval during very warm and humid conditions (Zhao-Liang Li, 2013). The results showed consistent accuracy of 1K level after all the validation and simulations on all land surface types including vegetation, water, and deserts.

The MOD21 product includes a swath Level-2 daily product, and daily and eight-day Level 3 gridded products in sinusoidal projection. MOD11 products are the Terra products which have been used here are retrieved at 1km pixels by the generalized split-window algorithm and at 6km grids by the day/night algorithm. In the split-window algorithm, emissivity in bands 31 and 32 are estimated from land cover types, atmospheric column water vapor and lower boundary air surface temperature are separated into tractable sub-ranges for optimal retrieval. In the day/night algorithm, daytime and nighttime LSTs and surface emissivity are retrieved from pairs of day and night MODIS observations in seven TIR bands. The product is composed of LSTs, quality assessment, observation time, view angles, and emissivities. All the MODIS LST products MOD11_L2, MOD11A1, and MOD11B1 had been validated at stage 1 with in situ measurements in more than 50 clear-sky cases in the temperature range of 263-331K and the column water vapor range of 0.4- 4cm and reprocessed into a new version every so often to provide the users with improved products. All the products of Terra MOD11 are shown in the Table (5) below to give a brief description of the products.

Earth Science Data Type (ESDT)	Product Level	Nominal Data Array Dimensions	Spatial Resolution	Temporal Resolution	Map Projection
MOD11_L2	L2	2030 or 2040 lines by 1354 pixels per line	1km at nadir	swath (scene)	None. (lat,lon referenced)
MOD11A1	L3	1200 rows by 1200 columns	1km (actual 0.928km)	daily	Sinusoidal
MOD11B1	L3	200 rows by 200 columns	6km (actual 5.568km)	daily	Sinusoidal
MOD11B2				eight days	
MOD11B3				monthly	
MOD11A2	L3	1200 rows by 1200 columns	1km (actual 0.928km)	eight days	Sinusoidal
MOD11C1	L3	360° by 180° (global)	0.05° by 0.05°	daily	equal-angle geographic
MOD11C2	L3	360° by 180° (global)	0.05° by 0.05°	eight days	equal-angle geographic
MOD11C3	L3	360° by 180° (global)	0.05° by 0.05°	monthly	equal-angle geographic

Table (5): Summary of the C6 MODIS LST data products (Credit: modis.gsfc.nasa.gov)

Among the products that have been mentioned in the table, MOD11C1 was selected to process the LST for time series analysis. MOD11C1 is a daily global LST product in a geographic projection.

It is created by assembling the MOD11B1 daily tiles together and resampling the Scientific Data Sets (SDSs) at 6km grids to the 0.05° spatial resolution of the Climate Modeling Grid (CMG) cells. The exact areal size of the equal angle grids varies with latitude, and it is 5.6km by 5.6km at the Equator. The LST values retrieved by the generalized split-window algorithm are used to supplement the LSTs retrieved by the day/night LST algorithm at grids where there is no valid pair of day and night observations (mostly in high-latitude regions). Due to this LST supplement, the spatial coverages of LSTs are larger than the spatial coverage of retrieved emissivities in the MOD11C products. There are 16 SDSs in the MOD11C1 product which are given in Table (6).

SDS Name	Long Name	Number Type	Unit	Valid Range	Fill Value	Scale Factor	Add Offset
LST_Day_CMG	Daily daytime CMG grid Land-surface Temperature	uint16	K	7500-65535	0	0.02	0.0
QC_Day	Quality control for daytime LST and emissivity	Uint8	none	0-255	0	NA	NA
Day_view_time	(local solar) Time of daytime Land-surface Temperature observation	uint8	hrs	0-120	0	0.2	0
*Day_view_angle	View zenith angle of daytime Land-surface Temperature	Uint8	deg	0-130	255	1.0	-65.0
LST_Night_CMG	Daily nighttime CMG grid Land-surface Temperature	uint16	K	7500-65535	0	0.02	0.0
QC_Night	Quality control for nighttime LST and emissivity	uint8	none	0-255	0	NA	NA
Night_view_time	(local solar) Time of nighttime Land-surface Temperature observation	uint8	hrs	0-120	0	0.2	0

*Night_view_angle	View zenith angle of nighttime Land-surface Temperature	uint8	deg	0-130	255	1.0	-65.0
Emis_20	Band 20 emissivity	uint8	none	1-255	0	.002	0.49
Emis_22	Band 22 emissivity	uint8	none	1-255	0	.002	0.49
Emis_23	Band 23 emissivity	uint8	none	1-255	0	.002	0.49
Emis_29	Band 29 emissivity	uint8	none	1-255	0	.002	0.49
Emis_31	Band 31 emissivity	uint8	none	1-255	0	.002	0.49
Emis_32	Band 32 emissivity	uint8	none	1-255	0	.002	0.49
Emis_20_night	Band 20 emissivity	uint8	none	1-255	0	.002	0.49
Emis_22_night	Band 22 emissivity	uint8	none	1-255	0	.002	0.49
Emis_23_night	Band 23 emissivity	uint8	none	1-255	0	.002	0.49
Emis_29_night	Band 29 emissivity	uint8	none	1-255	0	.002	0.49
QC_Emis	Quality control Emis	uint8	none	0-255	0	NA	NA
QC_Emis_night	Quality control Emis	uint8	none	0-255	0	NA	NA

Percent_land_in_grid	Percentage of Land in the Grid	uint8	none	0-100	0	1.0	0
----------------------	--------------------------------	-------	------	-------	---	-----	---

Table (6): Scientific Data Sets for MOD11C1 Products

3.2 Radar Data:

Radar remote sensing is gaining pace mostly in the last one or two decades. Especially, data from few number of spaceborne SAR systems like Spaceborne Imaging Radar-C/X-Band, Synthetic Aperture Radar (SIR-C/X-SAR), European Remote Sensing (ERS-1 and -2), Advanced Synthetic Aperture Radar (ASAR), Japanese Earth Resources Satellite (JERS-1), RADARSAT-1 and -2, Advanced Land Observation Satellite (ALOS-1) are commonly in use and applied at regional-scales. Most of the studies using Radar data is being used related to land cover, including improved land cover classifications, forest cover classifications, grassland monitoring, identification of degraded woodlands and mapping deforestation and successional forest dynamics. In the recent times, radar data have been exploited in combination with optical data for improved crop classifications and monitoring applications (Joshi, 2016).

3.2.1 Sentinel-1:

Sentinel 1 is the first mission of the Copernicus Program satellite constellation by the European Space Agency (ESA), launched in April 2014. The mission consists of two satellites S1A and S1B sharing the same orbital plane. Sentinel 1 satellites are active satellites and they use microwaves in the C-Band to capture topographic information of the earth surface. It has 4 imaging modes (StripMap, Interferometric Wide, Extra wide and Wave) with varying resolutions. Sentinel 1 satellite sensors measure the radar strength of the returned signal and the time it takes for a round trip of the signal to get the range location and brightness (or amplitude) of the pixels.

4. Methodologies:

4.1 Land Surface Temperature:

The Land Surface Temperature (LST) is the radiative skin temperature of the land surface, as measured in the direction of the remote sensor (sentinel.esa.int). LST is what satellite sees from top through atmosphere on earth surface. It might be snow, building, grass, etc. It is not the same as air temperature which is seen in the weather applications. LST is one of the Essential Climate Variables (ECVs) and an important factor in the land surface physical processes and global climate change (gcos.wmo.int). When LST is high, it increases the melting of glaciers at the Polar Regions and affects the vegetation. In the below Figure (15), LST is shown Worldwide for the month April, 2019 from the earth observatory NASA and data was collected using Moderate Resolution Imaging Spectroradiometer (MODIS) on NASA's Terra satellite.

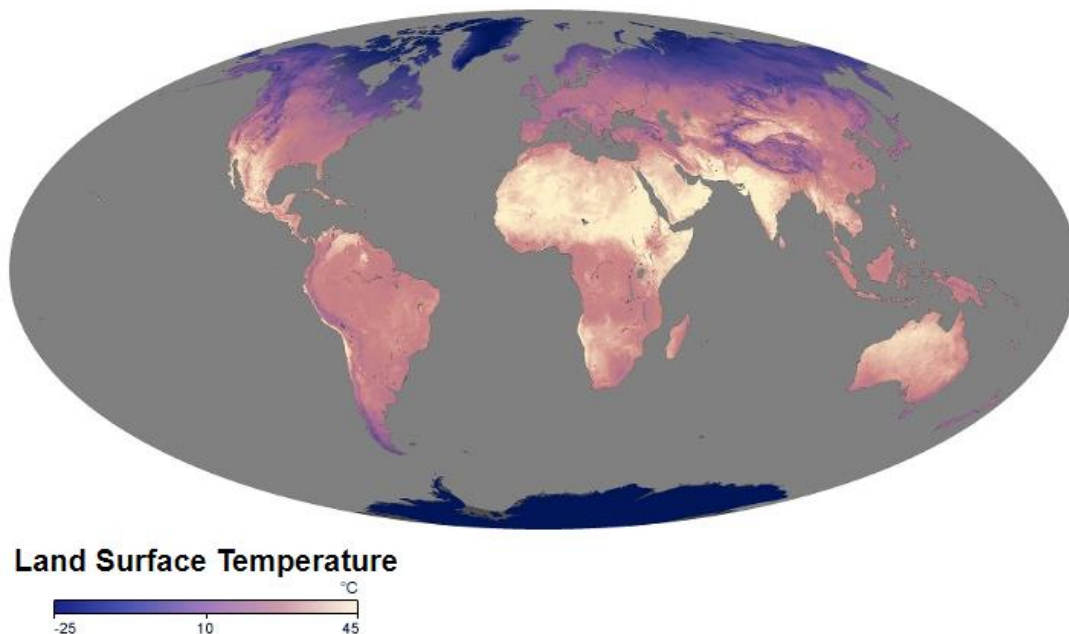


Figure (15): LST of overall world from the Earth observatory NASA

From the Figure (15), it can be observed that the equatorial places are warm throughout the year whereas Antarctica and Greenland are cold. These places are not much affected and remain constant while the mid to high latitude places LST change during the year.

4.1.1 Data for LST retrieval:

As mentioned earlier, Landsat 8 data is available free worldwide. It was ordered and downloaded from the website ([EarthExplorer - Home](#)) directly. There are other websites also available like <https://glovis.usgs.gov/> and <https://landsatlook.usgs.gov/>. USGS provides the data in Geotiff with metadata format which ends with _MTL.txt extension. An MTL file is the metadata file which includes the parameters of Unique Landsat scene identifier, WRS path and row information, Scene Center Time of the date the image was acquired, corner longitude and latitude in degrees and map projection values in meters, reflective, thermal, and pan band lines and samples, file names included, Image attributes including cloud cover, sun azimuth and elevation, and number of GCPs used, band minimum and maximum reflectance and radiance rescaling.

There are three Landsat collection levels of data available from USGS. Level 1 product consists of quantized and calibrated scaled Digital Numbers (DN) representing the multispectral image data which is delivered in 16-bit unsigned integer format. This data can be rescaled to TOA reflectance and/or radiance using radiometric rescaling factors given in the metadata file along with the TIFF images. Level 2 products are generated from level 1 and consist of surface reflectance and surface temperature science products. Level 3 products reduce the amount of time users spend on data processing and provide research-quality, applications-ready information on burned areas, surface water extent and snow cover(Source: USGS).

For the chosen study area, Landsat-8 Level-1 data from March, 2017 to March, 2020 was collected with Path 161 and Row 41. Table (7) gives the complete dates of the data that had been downloaded. The complete Level 1 product consists of 13 files, including OLI Bands 1-9 (one file per band) in Tagged Image Format Files (TIFF) , TIR Bands 10 & 11 (one file per band) in TIFF , a product-specific metadata file (MTL), and a Quality Assessment (QA) file. The Latitude and longitude is from 27° 80'-28° 20' N and 54° 70'-55° 20'.

Date of the Scene			
20170314	20180128	20190131	20200118
20170330	20180504	20190304	20200203
20170415	20180520	20190320	20200219
20170517	20180605	20190421	20200306
20170602	20180621	20190507	
20170618	20180707	20190523	
20170704	20180808	20190608	
20170720	20180824	20190624	
20170805	20180909	20190710	
20170821	20180925	20190811	
20170906	20181011	20190827	
20170922	20181112	20190912	
20171008	20181214	20191014	
20171024	20181230	20191030	
20171109		20191115	
20171125		20191201	
20171211			
20171227			

Table (7): Downloaded dates of the Landsat-8 Level-1 data products

4.1.2 Land Surface Temperature Calculation flowchart:

LST is estimated through Brightness Temperature from band 10 and 11 and Land Surface Emissivity (LSE) from NDVI of band 4 and 5. The complete procedure in steps is explained in the section 4.1.3. There are many algorithms to calculate LST. Some of the frequently used algorithms are Split-Window (SW) algorithm, Mono

Window (MW), Dual-Angle (DA), Single-Channel (SC), Sobrino and Mao, Root Mean Square Error. The flow chart of the estimation of LST using the Algorithm Avdan, 2016 is shown in Figure (16).

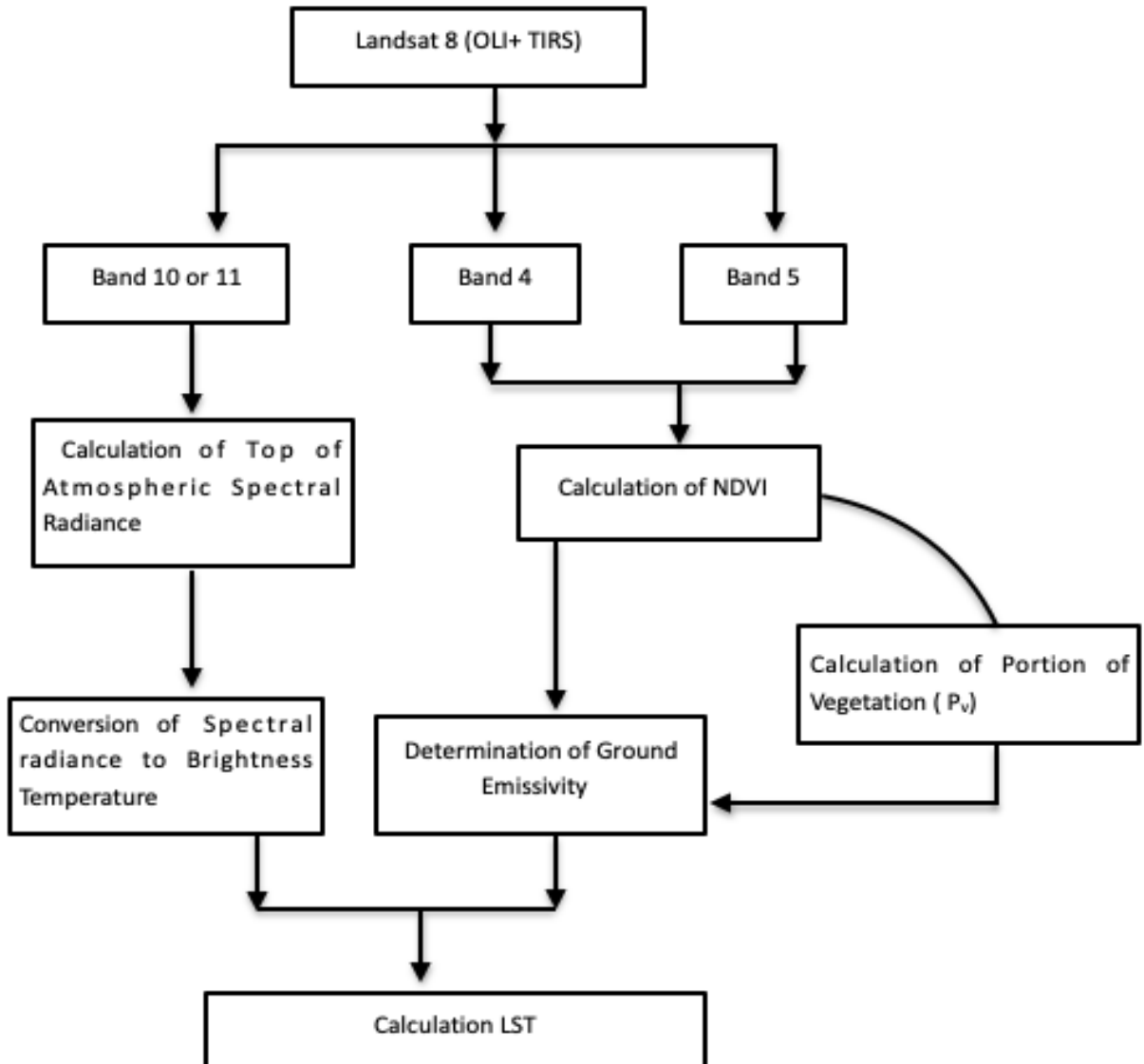


Figure (16): Flowchart of LST retrieval

4.1.3 Procedure for LST estimation:

LST retrieval algorithm uses spectral radiance and brightness temperature from the band 10 and normalized difference vegetation index (NDVI) from band 4 and 5 to get the emissivity through a portion of vegetation as inputs. This algorithm for LST retrieval is proven to be significant and close to in situ air temperature measurements (Avdan, 2016). The required metadata information in the Table (8) and formulae are mentioned in the latter section.

Metadata of the satellite images:

Thermal constant, band 10	
K1	1321.08
K2	777.89
Rescaling factor, band 10	
M_L	0.000342
A_L	0.1
Correction, band 10	
O_i	0.29

Table (8): Metadata values used in LST calculation

Step 1: Estimation TOA Spectral Radiance:

Before going to the calculation of TOA, there are some terms defined to get the clear idea of what TOA is.

Radiance is the radiation that is reflected from the clouds, surface and the neighboring pixels of surface. It depends not only on the orientation and position of the target but also on its intensity and direction. To put it in simple words, the light which travels through the atmosphere can change when it travels down to the earth because of scattering and diffusively reflects back because of the same scattering as shown in the Figure (17).

To define radiance and reflectance, one can say that radiance is the radiation that the instrument receives from the object that is being observed whereas the reflectance is the ratio of the amount of light coming from the target by the amount of

light striking the target. Radiance often has units of watt while reflectance has no units since it is a ratio and ranges from 0 to 1. These factors are corrected by converting the Digital Numbers (DN) to TOA spectral radiance (un-spider.org).

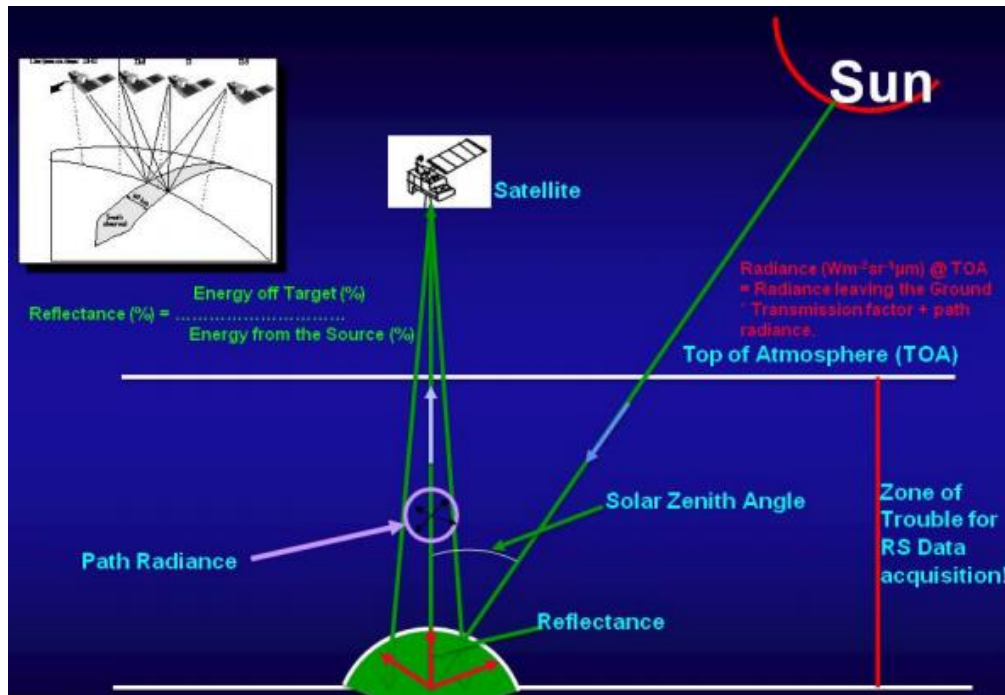


Figure (17): An illustration of Radiance, Reflectance, and TOA (Credit: un-spider.org)

Digital Number is a generic term for describing the pixel values. From the level-1 product, it is easy to rescale the DN values to TOA spectral radiance using the radiance rescaling factors from the metadata file. The input values as shown in Table (8) for band 10 was given based on the metadata and the formula used is taken from the USGS website.

$$L_{\lambda} = M_L Q_{\text{cal}} + A_L \quad (1)$$

Where,

L_{λ} = TOA spectral radiance (Watts/($\text{m}^2 * \text{srad} * \mu\text{m}$))

M_L = Band-specific multiplicative rescaling factor from the metadata (RADIANCE_MULT_BAND_x, where x is the band number)

A_L = Band-specific additive rescaling factor from the metadata (RADIANCE_ADD_BAND_x, where x is the band number)

Q_{cal} = Quantized and calibrated standard product pixel values (DN)

Step2: Converting TOA to Brightness Temperature:

Brightness temperature is a measurement of the radiance of the electromagnetic radiation travelling upward through the TOA to the satellite (remss.com). It is often measured in temperature units (kelvin/Celsius). After converting DN to radiance, the thermal bands have to be converted to temperature using the formula (2). To get the temperature in Celsius -273.15° C is subtracted. The values of K_1 and K_2 are taken from Table (8).

$$T_B = (K_2 / (\ln(K_1/L_\lambda) + 1)) - 273.15 \quad (2)$$

Where,

T_B = Top of atmosphere brightness temperature (celcius)

L_λ = TOA spectral radiance (Watts/($m^2 * srad * \mu m$))

K_1 = Band-specific thermal conversion constant from the metadata (K1_CONSTANT_BAND_x, where x is the thermal band number (10 in this case)).

K_2 = Band-specific thermal conversion constant from the metadata (K2_CONSTANT_BAND_x, where x is the thermal band number (10 in this case)).

Step 3: Calculation of Land Surface Reflectance (LSR) for NDVI:

Surface reflectance improves comparison between multiple images over the same region by accounting for atmospheric effects such as aerosol scattering and thin clouds, which can help in the detection and characterization of Earth surface change (usgs.gov). It is essentially a process of establishing and deducting atmospheric scatter reflectance from Top of Atmosphere reflectance (TOA). LSR here is calculated based on Dark Object Subtraction (DOS), which assumes that the signal to be processed is expressed in a radiance unit (μm).

Step 4: NDVI Calculation for emissivity estimation based on Surface reflectance:

The NDVI is a dimensionless index that describes the difference between visible and near-infrared reflectance of vegetation cover and can be used to estimate and understand the density of green on an area of land and to assess the changes in plant health.(Weier and Herring, 2000). NDVI value varies between -1 to +1. NDVI value close to -1 and 0 indicates the non-vegetated areas like barren soil, rock, water, clouds, snow and ice. NDVI close to +1 indicates the high density of vegetation.

The formula for NDVI calculation is,

$$NDVI = \frac{(NIR - VIS)}{(NIR + VIS)} \quad (3)$$

Where, NIR is reflectance in the near-infrared and VIS is reflectance in the visible red wavebands.

In Landsat 8, $NDVI = (Band\ 5 - Band\ 4) / (Band\ 5 + Band\ 4)$.

The reason to calculate NDVI is to estimate emissivity. There are many methods to calculate emissivity. But, here the NDVI threshold method is used as it can be used for any type of soil in the EM range of 10-12 μ m.

Step5: Estimation of proportion of vegetation:

Proportion of Vegetation is also called as Vegetation Fraction which is defined as the percentage of vegetation occupying the ground area in vertical projection. Changes in vegetation cover directly impact surface water and energy budgets through plant transpiration, surface albedo, emissivity, and roughness (Aman et al., 1992).

P_V is calculated using,

$$P_V = (NDVI - NDVI_S / NDVI_V - NDVI_S)^2 \quad (4)$$

Where,

NDVI of Soil ($NDVI_S$) = 0.2

NDVI of Vegetation ($NDVI_V$) = 0.5

Step6: Calculation of Land Surface Emissivity (LSE):

As mentioned, Land Surface Emissivity is a main factor in calculating LST. LSE measures the inherent characteristic of earth's surface. It measures its ability to convert thermal or heat energy into radiant energy (Avdan, 2016). There are three conditions to calculate LSE based on the type of soil. So, the threshold of NDVI is used to calculate LSE from space. This method is developed by Sobrino and Raissouni (2000). Due to the simplicity of this method, the NDVI threshold method has already been successful. It needs the values of emissivity of soil, emissivity of vegetation, surface roughness and proportion of vegetation.

$$\varepsilon_i = \left[\begin{array}{ll} a_i Q_{red} + b_i & \text{NDVI} < \text{NDVIs} (0.2) \\ \varepsilon_{v,i} P_v + \varepsilon_{s,i} (1 - P_v) + C_i & \text{NDVIs} \leq \text{NDVI} \leq \text{NDVlv} (0.5) \\ \varepsilon_{v,i} + C_i & \text{NDVI} > \text{NDVlv} \end{array} \right] \quad (5)$$

Where, a , b are channel dependent regression coefficients Q_{red} is the reflectivity in the red channel, and NDVIs is the NDVI corresponding to bare soil. $\varepsilon_{v,i}$ (TIRS Band 10 = 0.9863 and Band 11 = 0.9896) and $\varepsilon_{s,i}$ (TIRS Band 10=0.9668 and Band 11=0.9747) are the vegetation and soil emissivities at wavelength λ , respectively. Both of them can be measured in the field (Rubio, Caselles, and Badenas 1997; Rubio et al. 2003) or obtained from an emissivity database (Baldrige et al. 2009). P_v is the fraction of vegetation that can be derived either from the NDVI. NDVIs and NDVlv can be estimated from the histogram for the entire scene (Dash et al. 2005; Sobrino et al. 2008). While C_i is the surface roughness.

Surface Roughness is calculated using again emissivity of soil, emissivity of vegetation, proportion of vegetation and the new factor called geometric factor (F').

$$C_i = (1 - \varepsilon_{s,i}) \varepsilon_{v,i} F'(1 - P_v) \quad (6)$$

Geometric factor is estimated from the elevation using the Digital Elevation Model which ranges between 0 and 1 and $\varepsilon_{s,i}$, $\varepsilon_{v,i}$ are the emissivity values from band 10 with 0.9668 and 0.9863.

When $\text{NDVI} < \text{NDVIs}$, the relationship between the emissivities and the red reflectivities is assumed to be linear and the coefficients can be determined from laboratory measurements of the soil spectra.

When $\text{NDVIs} < \text{NDVI} < \text{NDVlv}$, surface roughness C_i can be expressed as a linear function of P_v (Sobrino and Raissouni 2000).

When $\text{NDVI} > \text{NDVlv}$, typical constant values of $\varepsilon_{v\lambda} = 0.985$ and $d\varepsilon_{\lambda} = 0.005$ are used in TIR bands (Sobrino et al. 2008).

Step7: Calculation of LST:

The LST is calculated using emissivity through NDVI method and Brightness temperature. It is computed as follows.

$$LST = \frac{T_B}{\{1 + [(\lambda BT/\rho) \ln \epsilon_\lambda]\}} \quad (7)$$

Where,

LST = Land Surface Temperature in Celsius ($^{\circ}\text{C}$)

T_B = Brightness temperature in Celsius ($^{\circ}\text{C}$) calculated from Formula (2)

λ = Wavelength of the emitted radiance ($\lambda = 10.895$)

ϵ_λ = emissivity calculated from Formula (5)

And ρ is estimated as

$$\rho = hc/\sigma \quad (8)$$

Where

σ = Boltzmann constant (1.38×10^{-23} J/K)

h = Planck's constant (6.626×10^{-34} J s)

c = velocity of light (2.998×10^8 m/s)

4.1.4 Challenges in LST retrieval:

The retrieval of LST is not easy from space and the direct estimation is not possible as there will be a combined effect of LST and LSE, or the atmospheric contamination. There are mainly two problems besides the below given problems. They are the separation of surface emissivity and temperature from radiance at ground level and atmospheric corrections. The other problems could be (sentinel.esa.int):

- Temperature variations with angles
- Sub-pixel in-homogeneities in temperature and cover
- Surface spectral emissivity at the channel wavelengths
- Atmospheric temperature and humidity variations
- Clouds and large aerosol particles such as dust.

The separation of surface emissivity and temperature is the problem of under determination. It is troublesome because the problem is mathematically unsolvable even for at-ground radiances. The radiative transfer equation (RTE) shows that the radiance emitted from the surface in the infrared region is a function of its temperature and its emissivity. If the radiance is measured at N wavelengths, there will always be $N + 1$ unknowns, corresponding to N emissivities at each wavelength and an unknown surface temperature (Zhao-Liang Li, 2013). The solution of a set of underdetermined equations described by measured radiances is the main difficulty in the retrieval of LST and LSE. The coupling of LST and LSE makes the determination of LSE require the simultaneous determination of LST and vice versa (Li and Becker 1993; Becker and Li 1995; Li, Petitcolin, and Zhang 2000).

In addition to this, atmospheric absorption, emission and surface reflection increase the problem. Despite this, if the emissivity is not equal to 1, it causes reduction of the surface emitted radiance (Dash et al. 2005).

In the end, the combined effect of non-unity emissivity and the atmosphere further complicates the retrieval of LST and LSE from the TOA measurements.

4.2 Band Pass Decomposition:

As mentioned in the section 1, to find the thermal variations in a time series using different scales of images, the best approach is to combine them using the filtering techniques both temporally and spatially. The choice of filter in this approach is subjective, having the main aim as highlighting the fine details around the study area over the same time scales. This is a multiscale approach to estimate variations in temperature. To begin with, band pass decomposition is done on both high resolution images and low resolution images into different length scales. Band-passed images are generated by applying a series of Gaussian filters with different spatial scales and taking the difference between two neighboring scales. Filter limits were chosen as the scale with integer powers of two (in units of integer numbers of pixels). To properly represent the amount of information carried in each channel, Shannon-Nyquist sampling theorem is applied to resample them. The resampled point sets from selected band-pass channels are used to estimate the transfer function (Lin, 2010).

There are basically three different kinds of filters: low pass, high pass and bandpass and filters. A low-pass filter attenuates high frequencies and retains low frequencies unchanged. The result in the spatial domain is equivalent to that of a smoothing filter as the blocked high frequencies correspond to sharp intensity changes, *i.e.* to the fine-scale details and noise in the spatial domain image. A high pass filter, on the other hand, yields edge enhancement or edge detection in the spatial domain,

because edges contain many high frequencies. Areas of rather constant gray level consist of mainly low frequencies and are therefore suppressed.

A bandpass attenuates very low and very high frequencies, but retains a middle range band of frequencies. Band pass filtering can be used to enhance edges (suppressing low frequencies) while reducing the noise at the same time (attenuating high frequencies). In ideal band pass filters, frequencies within the given range are passed through without attenuation and frequencies outside of the given range are completely removed. This behavior makes ideal band pass filters very sharp. The centered Fast Fourier Transform (FFT) is filtered by the following function, where D_L is the lower bound of the frequency band, D_H is the upper bound of the frequency band, and $D(u,v)$ is the distance between a point (u,v) in the frequency domain and the center of the frequency rectangle (I3harrisgeospatial.com).

$$H(u,v) = \begin{cases} 1 & \text{if } D_L \leq D(u,v) \leq D_H \\ 0 & \text{otherwise} \end{cases} \quad (9)$$

As gaussian is used as a band pass filter here, the transition between unfiltered and filtered frequencies is very smooth.

The centered FFT is filtered by one of the following functions, where D_0 is the center of the frequency band, W is the width of the frequency band, and $D=D(u,v)$ is the distance between a point (u,v) in the frequency domain and the center of the frequency rectangle(I3harrisgeospatial.com).

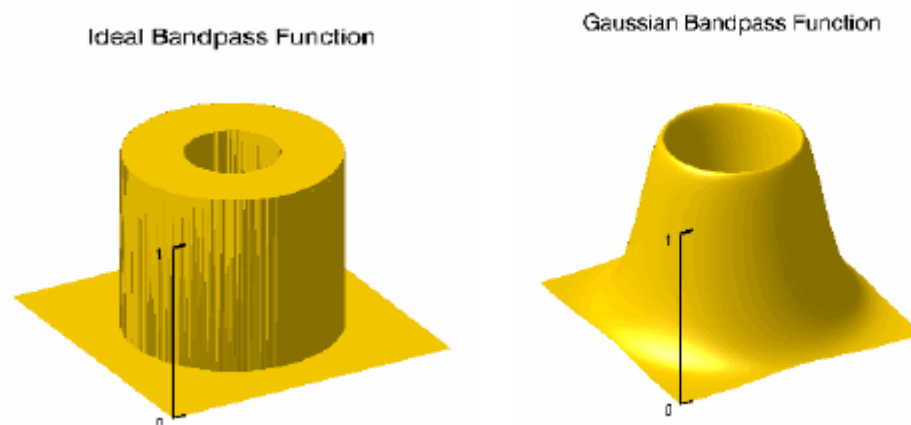


Figure (18): A visual representation of An ideal bandpass filter and Gaussian bandpass filter (I3harrisgeospatial.com)

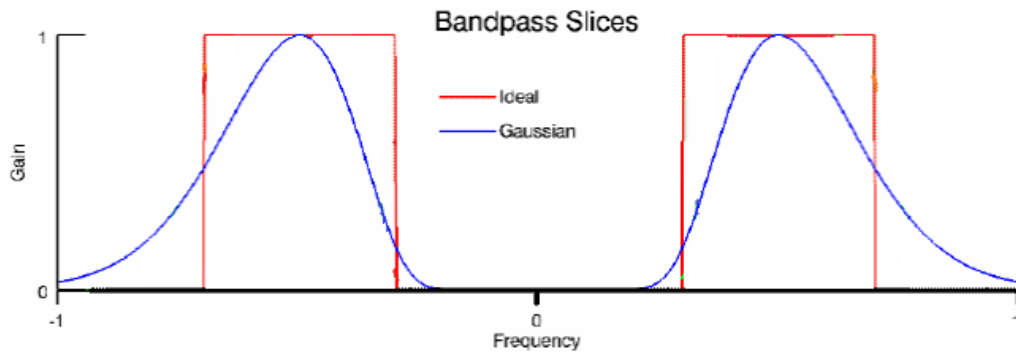


Figure (19): A visual representation of An ideal band pass filter and Gaussian band pass filter (l3harrisgeospatial.com)

To estimate the transfer function, resampled points from selected band pass channels are needed. These sample points are calculated by using the Shannon-Nyquist sampling theorem. It describes how to sample a signal or waveform in such a way as to not lose information and gives what sample rate to use to prevent aliasing from happening. Aliasing arises when the wrong sampling rate is used. It fails to reconstruct the original signal, causing it to appear as a completely different wave of a lower frequency. Shannon-Nyquist sampling theorem combats this problem by taking the sampling frequency equal to the twice of the highest frequency component (Dalibor, 2015).

$$f_{\text{sample}} > 2f_{\text{max}} \quad (10)$$

Band pass decomposition steps are explained in the form of flowchart in Figure (20). Firstly, both MODIS data has low resolution and Landsat-8 which has high resolution are taken and band pass decomposition is performed as explained before. The result of Band pass decomposition will be a series a band passed images with one low pass image and high pass image. Low pass image from the MODIS and band pass and high pass images from Landsat-8 are considered so that no details from MODIS will be missed. From the combination of Low pass image, band pass images, and high pass image, a corrected LST map of Landsat-8 if formed.

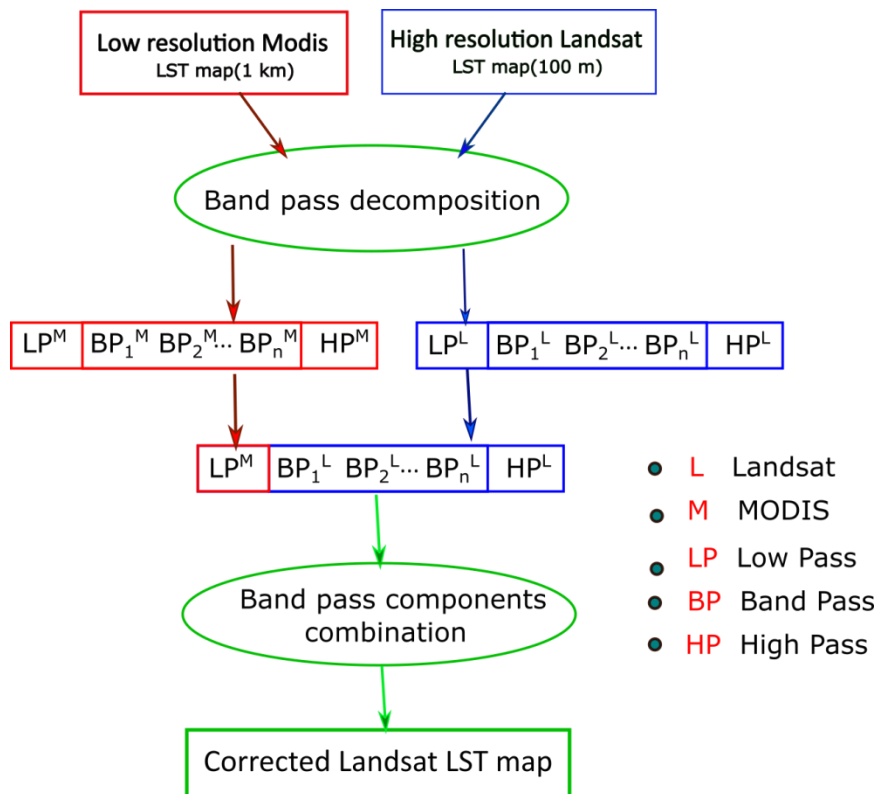


Figure (20): A flowchart of Band pass decomposition

4.3 InSAR time series analysis:

InSAR is the best technique to detect and monitor a regional-scale ground deformation at two times in the same area with a centimetre of accuracy. InSAR phase measurements detect changes between two SAR acquisitions, which are generally referred to as master and slave acquisitions. Sentinel-1 data is collected to observe the time dependent deformation in the study area and ? Interferograms were processed from the year 2017 to 2020. For processing of S-1 images and generating interferograms, GMTSAR is used. GMTSAR is an open source (GNU general public license) InSAR processing system. It supports InSAR processing on the following satellite images: ERS-1/2, Envisat, ALOS-1, TerraSAR-x, COSMOS SkyMed, Radarsat-2, Sentinel-1a/b, and ALOS -2. The difference between GMTSAR and other InSAR systems such as ROI PAC, Gamma, and DORIS is that in GMTSAR processing, there is a need for orbital accuracy of sub-meters. Furthermore, processing a large set of images can be automated without human

intervention. As mentioned above, GMTSAR is based on the Generic Mapping Tools (GMT) (Sandwell et al., 2016).

GMT is an open source collection of programs which manipulates and displays geographic data sets (Wessel et al., 1998; Wessel et al. 2013).

To study the temporal behavior of the study area over time, the effective way is the generation of time-series that allows us to observe the displacement on the earth's surface (Berardino et al., 2002). There are many algorithms available for the time series analysis, as it is an important tool for monitoring and measuring the displacement of the Earth's surface. For this task, Small Baseline Subset (SBAS) introduced by Berardino et al., 2002 has been used. It is a network of interferograms with small temporal and spatial baselines (Berardino et al., 2002; Schmidt and Bürgmann, 2003). The SBAS method effectively reduces the decorrelation phenomena by analyzing high coherence distributed scatterers based on small baseline interferograms combination. The master and slave pairs for these interferograms are selected using the average baseline parameters (Osmanoğlu,2016).

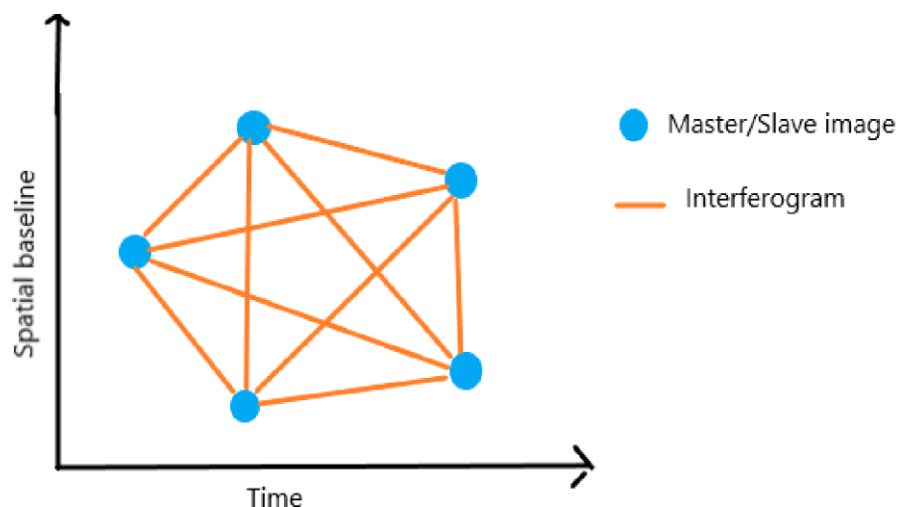


Figure (21): Spatio temporal Interferogram network, SBAS

As shown Figure (21), it combines multiple unwrapped interferograms to generate a time series. The spatial baseline describes the distance between the sensor positions at different acquisitions in the orbit and the temporal baseline indicates the time difference between the acquisitions respectively. Later the interferograms are generated between the connected pairs and they are flattened and filtered, and the unwrapped phases are produced as shown in Figure (22).

SBAS Algorithm

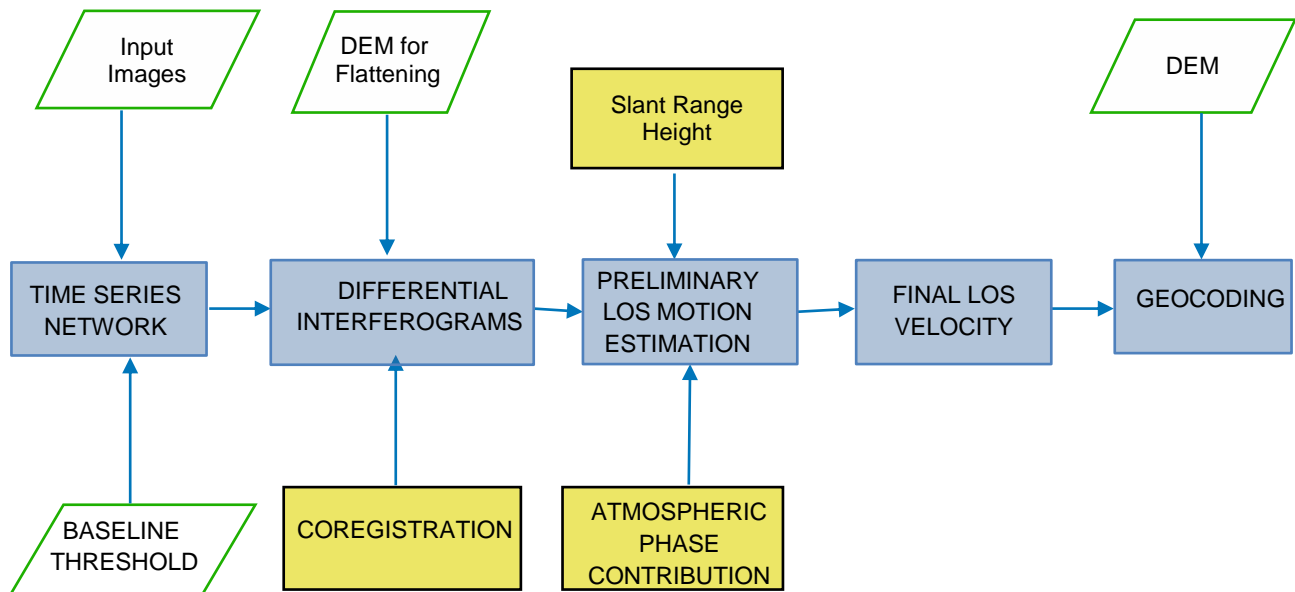


Figure (22): Small Baseline Subset Interferometry (SBAS) algorithm steps

The interferogram flattening is done using the input DEM. The related displacement products such as date by date values, velocity and acceleration and height (new slant-range DEM) are created. The atmospheric corrections are projected onto the cartographic system. In the end, the results are projected onto the cartographic system.

5. Results and Discussion

5.1 LST Results from LANDSAT-8 Data:

As explained in the previous section 4.2.1, LST retrieval has been done using the Landsat-8 level-1 products (Top of Atmosphere (TOA) Reflectance). The results of all the steps from section 4.1.3 are presented here in the form of plots.

5.1.1 Calculation of TOA (Top of Atmospheric) reflectance:

LST retrieval using TOA reflectance has the advantage that no correction/conversion e.g., atmospheric correction, angular effects and topographic corrections is necessary and the actual radiometric measurements can be used for retrieval.

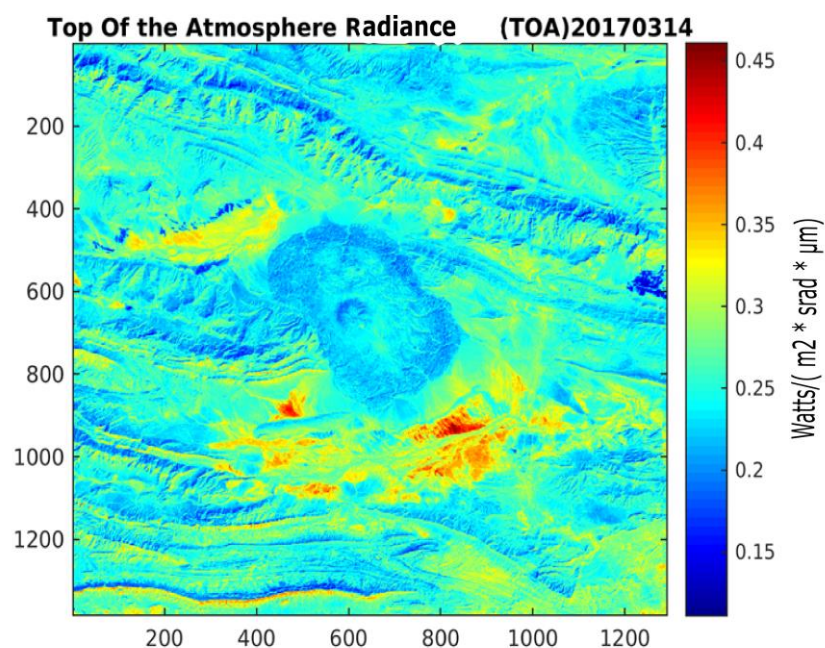


Figure (22): Calculation of TOA (Top of Atmospheric) reflectance

TOA from Figure (22) is produced for the date 2017/March/14 and shows that TOA values are varying between 0.15 and 0.45. Only at some places around the study area has high TOA values and remaining are either low or medium TOA radiance values depending on the properties of the objects reflected from surface. The topography in this figure is clearly visible and showing the TOA radiance due to variability of vegetation properties and surface. This is also affected by the source of the radiation, which is the sun in case of optical imagery.

5.1.2 Converting TOA to Brightness Temperature:

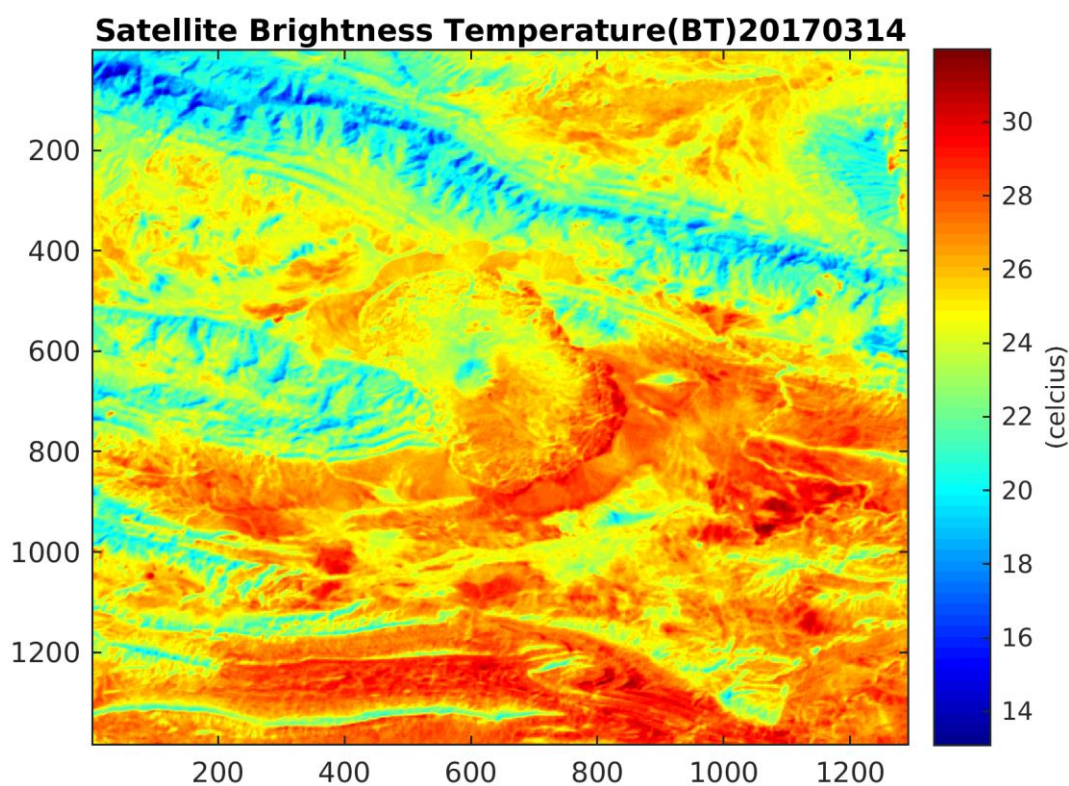


Figure (23): Converted TOA to Brightness Temperature

Figure (23) represents the Brightness temperature for the date 14/March/2017 and has temperature values in Celsius ranging from 14° to 30°. The low temperatures are seen from mountainous areas and water areas. As it is from the mid of March, the temperature values are neither high nor low but as an exception some place have high temperatures of more than 30°.

5.1.3 Estimated Land Surface Reflectance (LSR) for NDVI:

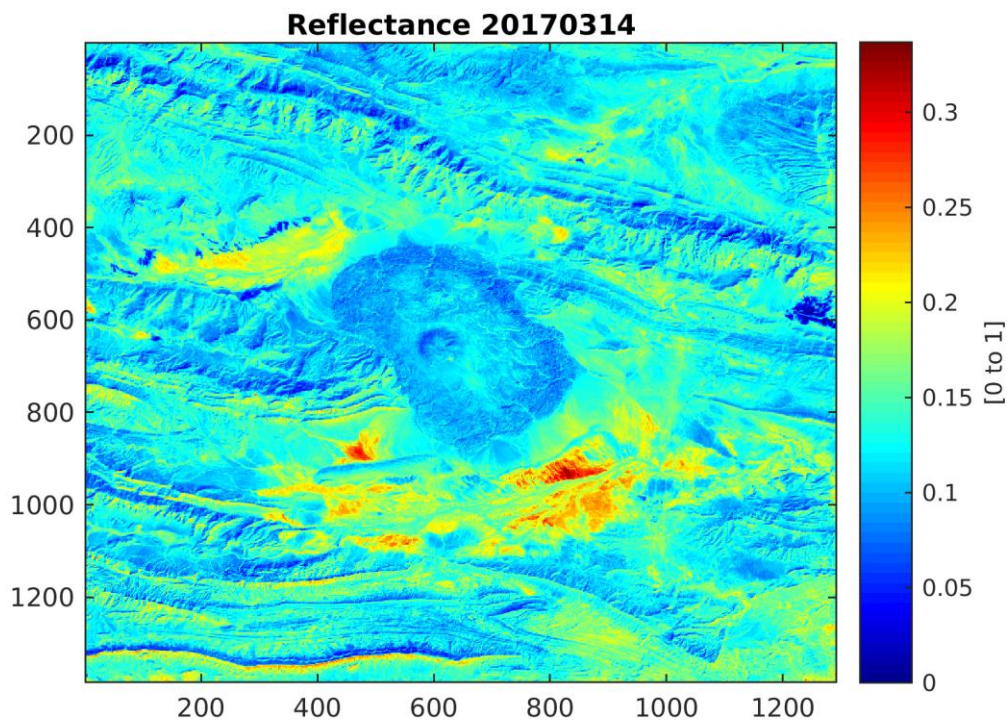


Figure (24): Estimated Land surface reflectance

As spectral reflectance is a measure of how much energy (as a percent) a surface reflects at a specific wavelength, it depends on the object properties and wavelengths. Clouds and other properties cannot effect the surface reflectance values. Usually, for high vegetated areas and snow areas have high surface reflectance values between in the near-infrared between 0.7 and 1.3 μm whereas water has low reflectance values. As the study area is arid type, it has low surface reflectance values between 0 and 0.3 μm .

5.1.4 Calculated NDVI for emissivity estimation:

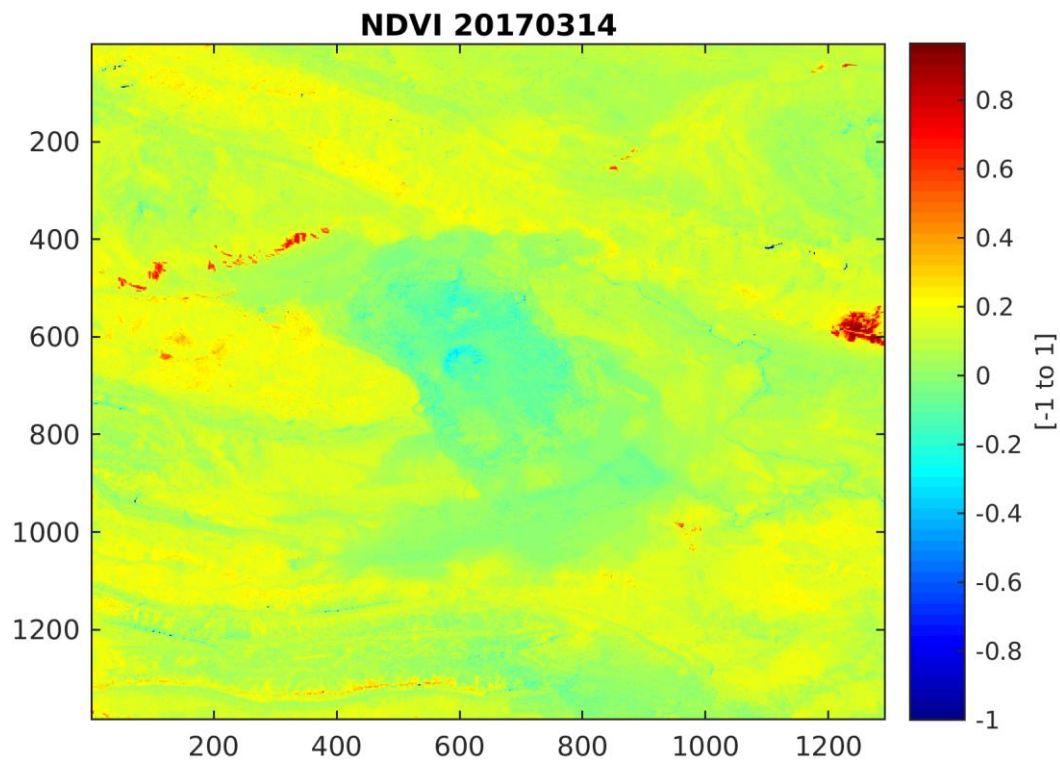


Figure (25): Calculated NDVI

Usually, low values of NDVI between 0.1 and below correspond to barren areas of rock, sand, or snow. Moderate values between 0.2 and 0.3 represent shrub and grassland whereas high values between 0.6 and 0.8 represent temperate and tropical rainforests. Study area in this case is indicating values mostly between -0.2 and 0.25 which indicates grass land and shrub as it is produced for the month of March as shown in Figure (25).

5.1.5 Estimated Land Surface Emissivity (LSE):

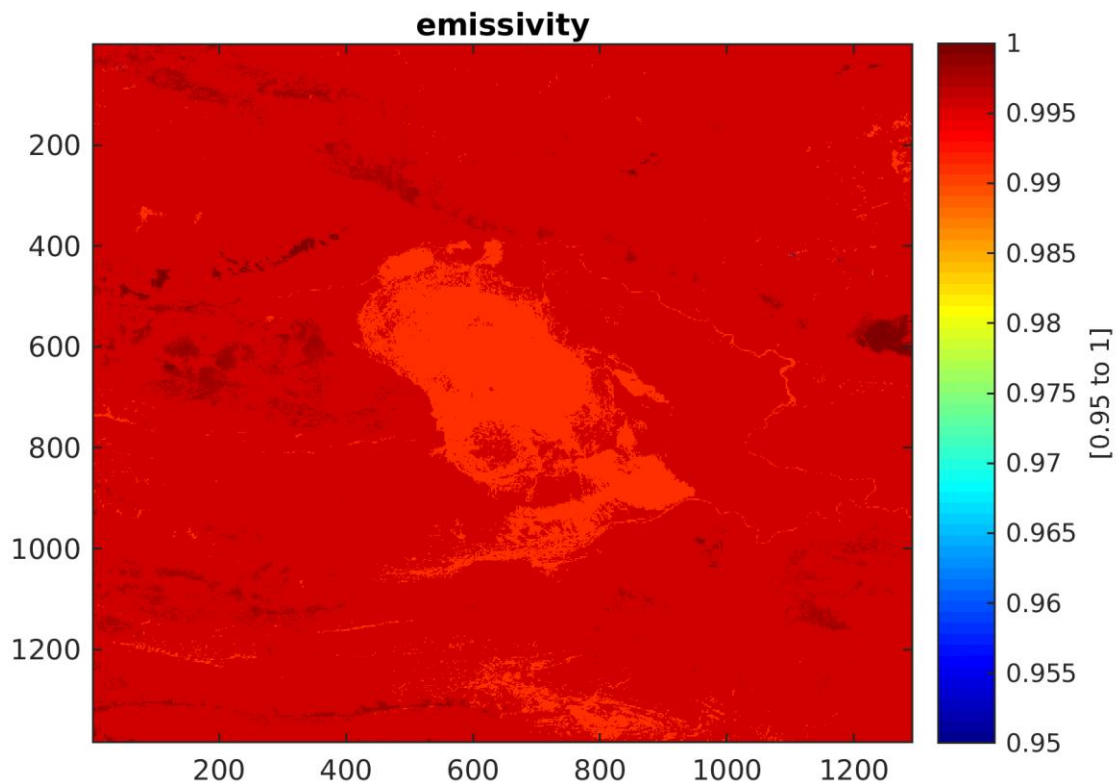


Figure (26): Estimated Land Surface Emissivity

Usually, the emissivity value of water and soil are assigned as 0.991 and 0.996. Emissivity 0 represents a perfect reflector and 1 represents a perfect emitter. It depends on the temperature of the surface as well as wavelength and angle. In this case, a priori LSE is assumed for band 10 of Landsat-8 to calculate the real LSE based on the range of NDVI values. As seen in the above Figure (26), it indicates values between 0.985 and 1 which represents that it is a high emissivity area.

5.1.6 Land Surface Temperature:

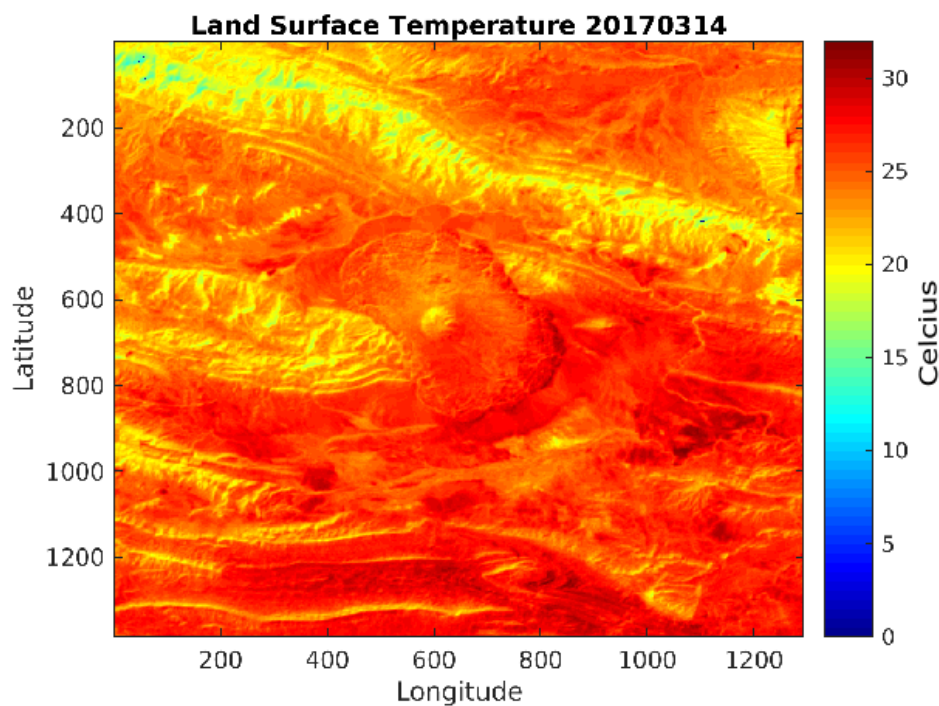


Figure (27): Estimated Land Surface Temperature representing from 03/March/2017.

Figure (27) represents LST map having the temperature values between 20° and 30° . There are moderate temperatures in the vegetated areas and mountainous area and high temperatures at the rock, soil areas and Urban area. The local temperature changes representing high values at some places and low values at some places may be due to the physical properties of the atmosphere and dynamical processes.

5.2 Generation of LST maps:

LST maps are generated for all the satellite observations and presented in this section. The knowledge of the LST maps provides information on the temporal and spatial variations of the surface equilibrium state. Only few LST maps from all the different satellite observations for three years are presented below.

5.2.1 LST maps from Landsat-8:

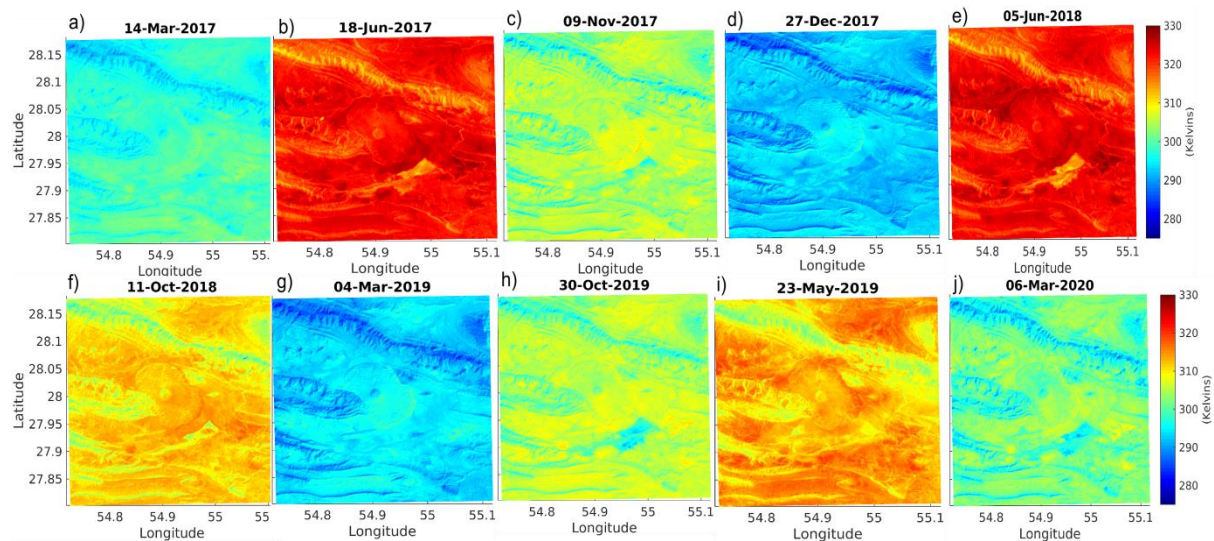


Figure (28): LST maps from Landsat-8 (Plot a is the LST map from 14/March/2017, plot b from 18/June/2017, plot c from 09/November/2017, plot d from 27/December/2017, plot e from 05/June/2018, plot f from 11/October/2018, plot g from 04/March/2019, plot h from 30/October/2019, plot i from 23/May/2019, plot j from 06/March/2020)

LST maps from Landsat-8 data shows very fine details of the study area because of its high resolution. All the LST maps are representing the different seasons with different temperature variations. It is seen from Figure (28) that, the LST maps of a and j which are from the month of March show the same temperature variations. Likewise, the plots of e and h from December are also similar. It can be observed that the month of June is the hottest month with high temperatures around 320K to 330K, whereas the December month with plots e and h show the less temperature around 300K to 310K.

5.2.2 LST maps from MODIS data:

After MODIS daily data was collected in .hdf format, all the data files were processed and latitude, longitude and LST daytime information was extracted. According to MODIS user guide, a scale factor of 0.02 is applied to the LST.

Since MODIS data is global, it has to be cropped according to the study area. The time series analysis was performed for the collected information of Lat, Lon and LST values. The plotted results are shown in the below Figure (29).

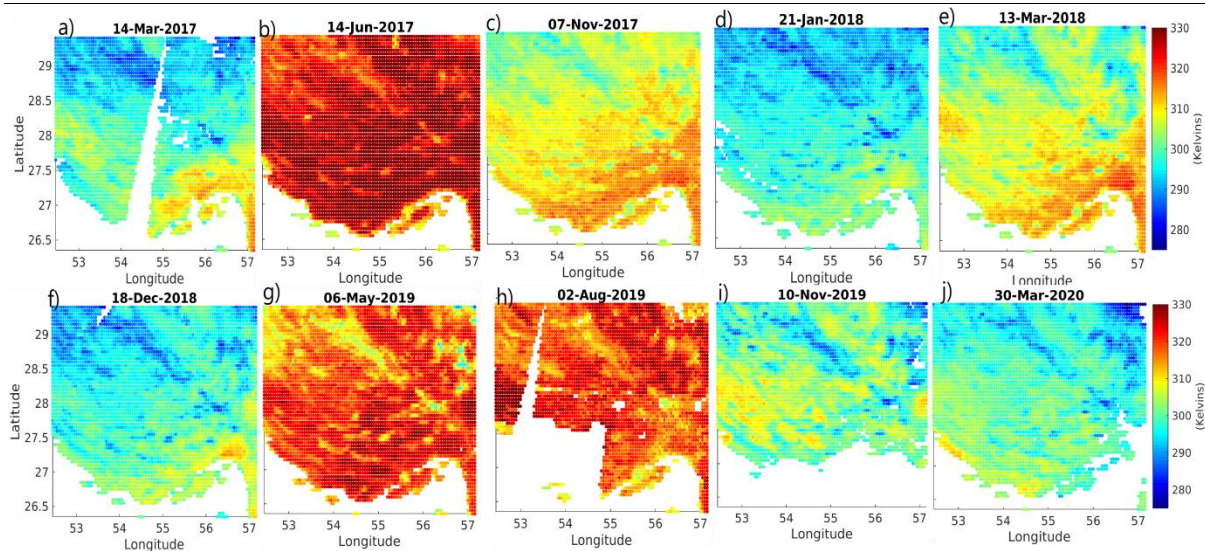


Figure (29): LST maps from MODIS daily (Plot a is the LST map from 14/March/2017, plot b from 14/June/2017, plot c from 07/November/2017, plot d from 21/January/2018, plot e from 13/March/2018, plot f from 18/December/2018, plot g from 06/May/2019, plot h from 02/August/2019, plot i from 10/November/2019, plot j from 30/March/2020)

MODIS LST maps are covering the large area around the study area because of its spatial resolution of 1km. As it is daily data, 995 LST maps were produced for three years but only few are presented in the Figure (29). It can be observed from the plots of d and g is that the hottest temperatures are present in the months of May, June, July, August. The plots of a, c, i and f from the months December, January, and February show the low temperatures while November from plot h shows the moderate temperatures. These values are not same for the whole month and changes day to day. For example, plot b from 11/November/2017 shows low temperatures on the top right corner of the study area than the plot h from 07/November/2019. All these local variations depend on the weather.

5.2.3 LST maps from Sentinel-3 data:

Sentinel-3 LST products have effective emissivity and atmospheric corrections which allows accurate LST retrievals using the SLSTR thermal bands but the disadvantage is to have spatial resolution of 5km. Likewise for Landsat-8 and MODIS, Sentinel -3 data was also downloaded for three years (2017 to 2020) in NetCDF (Network Common Data Form) with .nc extension. All datasets were read using ncread function and Latitude, Longitude, time, and LST information was collected.

As sentinel-3 is also global data, it was cropped according to study area and LST maps were produced.

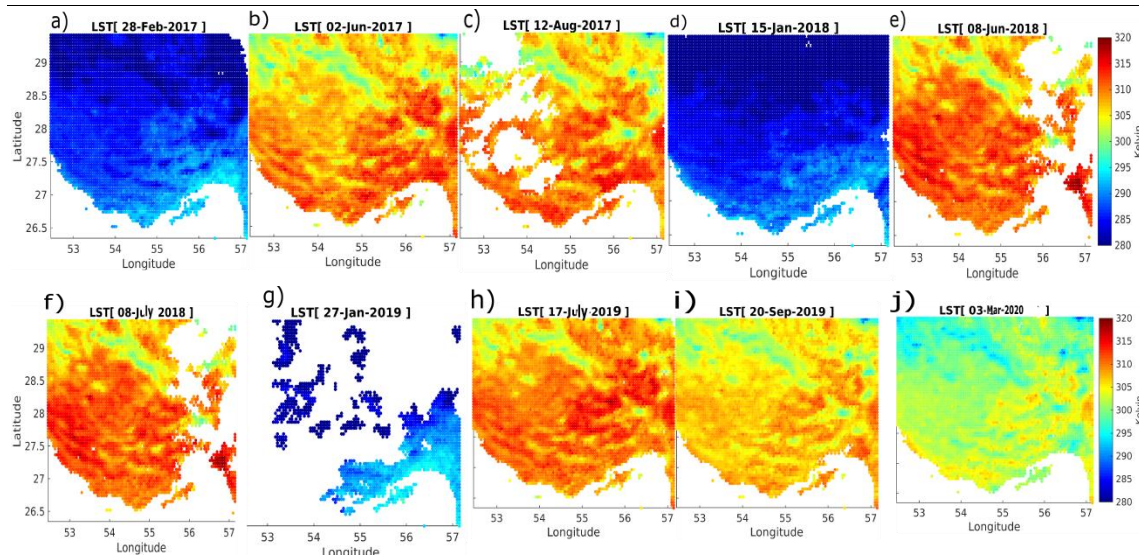


Figure (30): LST maps from Sentinel-3 daily data (Plot a is the LST map from 28/February/2017, plot b from 02/June/2017, plot c from 12/Augustr/2017, plot d from 15/January/2018, plot e from 08/June/2018, plot f from 8/July/2018, plot g from 27/January/2019, plot h from 17/July/2019, plot i from 20/September/2019, plot j from 3/March/2020

Sentinel-3 satellite has a high spectral resolution of OLCI instrument, it is suitable for a better characterization of the atmosphere, along with the dual view available in the SLSTR instrument, which allows a better atmospheric correction and also an improvement in the novel cloud screening procedures. However, the spatial resolution is not as good as Landsat-8 and Sentinel-3. In total, 1125 LST maps were produced for the past three years and Figure (30) represents few from them. The plots G and I from August month show the high temperatures and plot A shows the low temperature. It can be interpreted from the LST maps is that, when compared to MODIS and Landsat-8 there are few gaps or missing data in the Sentinel-3. Nonetheless, all these maps show the temperature changes similar to MODIS and Landsat-8 by showing the high temperature during the summer and low in winter.

5.3 Time series analysis of generated LST maps:

Time series analysis was performed to add much more value to the LST by analyzing multiple LST's and to capture the gradual or long-term change processes, as well as to overcome the gaps due to cloud cover. For each Satellite data, three points P1, P2 and P3 of Latitude and Longitude are taken around the study area to check for thermal variations.

5.3.1 Time series analysis of Landsat-8 LST maps:

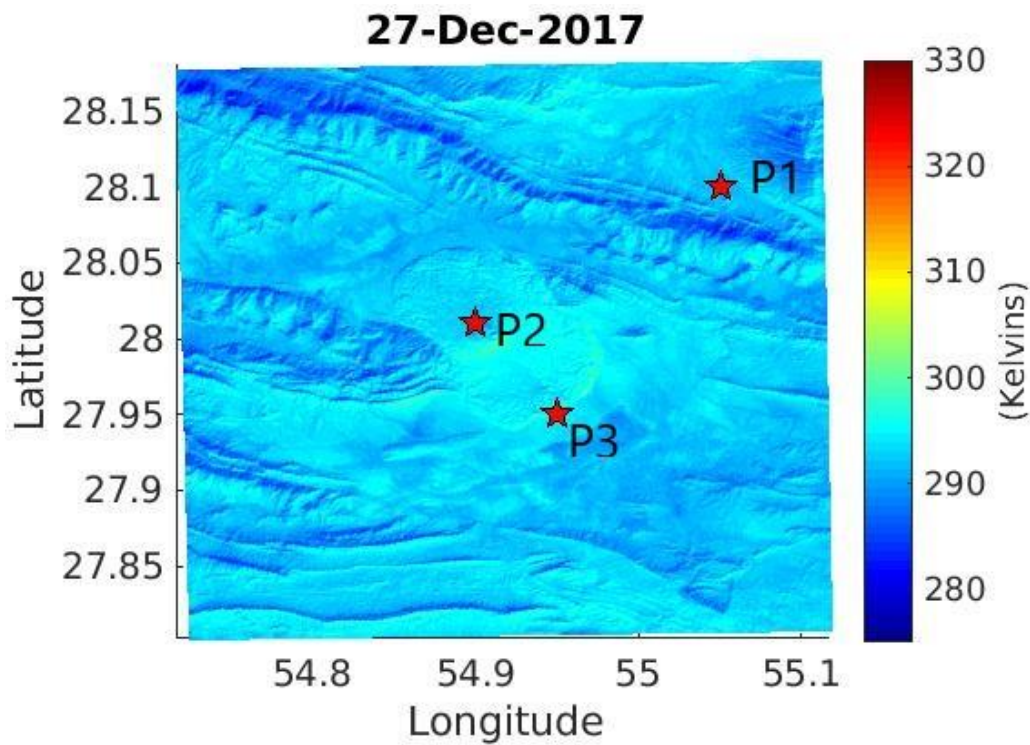


Figure (31): LST MAP from Landsat-8 data processed for the date of 27/December/2017 to check time series plots at P1, P2 and P3 of Latitude and Longitude.

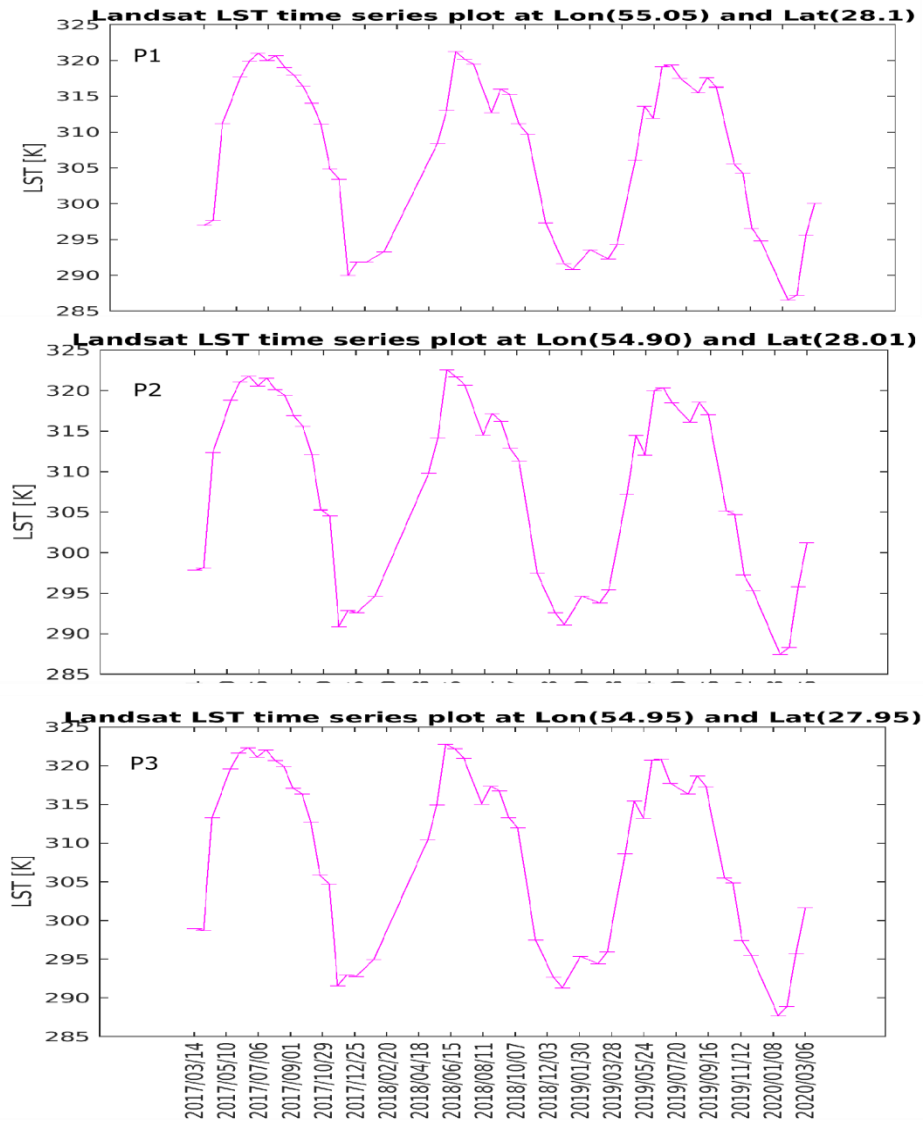


Figure (32): Time series of LST map from Figure (31). (P1 is the point at Latitude of 28.10 and Longitude of 55.05. P2 represents the point at Latitude of 28.01 and Longitude of 54.90. P3 is the point at Latitude of 27.95 and Longitude of 54.95.)

The resulted plots of time series analysis from landsat-8 data are showing the same seasonal trend over the three years but with the slightly decrease in temperature globally. Among the three points, 2 points (P2 and P3) are taken near to the salt dome and P1 is taken far from the salt dome to analyse the differences visually. It is observed from the Figure (32) that, the highest temperature from P1 in the year 2019 is around 323K whereas for P2 and P3, it is slightly less by 1°C. Distinctly, in 2020 year, all the points are showing decrease in temperature of 2°C from the previous year.

Though the spatial resolution of Landsat-8(OLI=30m/TIRS=100m) is better than MODIS (1km) and Sentinel-3(5km), the temporal resolution (16 days) is not very good. However, with the high spatial resolution, it makes a very good data set to

detect and analyze thermal variation keenly. In general, the ground-based instruments provide accurate estimates at point locations, which are not influenced by the atmospheric conditions. On the contrary, the satellite-based sensors provide an average estimate of LST. Between the two methods, the satellite-based one is much preferable if the understanding of the spatial distribution of the LSTs is required for an environmental issue of interest. But the main problem lies in the globally applicable thermal atmospheric corrections that are representative of global atmospheric variability, and the distribution of some critical parameters e.g. air temperature, water vapor and air pressure. The problem of the separation between emissivity and LST is also another important factor. The other reason is the assumed values of NDVI for soil and vegetation during the calculation of proportion of vegetation and surface roughness that are used to retrieve the LST.

Which is why, taking different available datasets to perform the analyses and comparison gives improved results close to ground based instruments. Apart from Landsat-8 data, operational satellite data like MODIS and Sentinel-3 were taken. The operational satellite products like MODIS LST from NASA's Terra/Aqua platforms are available daily, with greatly enhancing temporal sampling of temperature distributions. Sentinel-3 data is good for the cloudiest area as it is available for every hour and every 10 days. These satellites differ from each other in terms of their spatial and temporal resolutions. In general, if a satellite has high spatial resolution, then its temporal resolution is low or vice versa.

5.3.2 Time series analysis of MODIS LST maps:

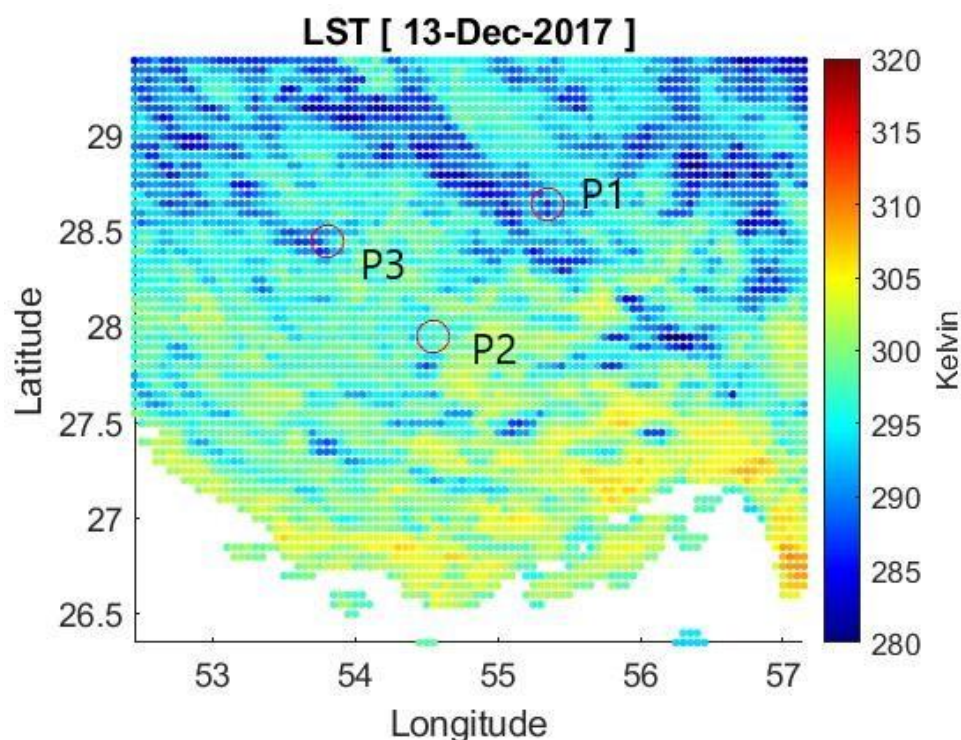


Figure (33): LST map of MODIS daily dataset from 13/December/2017. P1, P2 and P3 represent the points Latitude and Longitude.

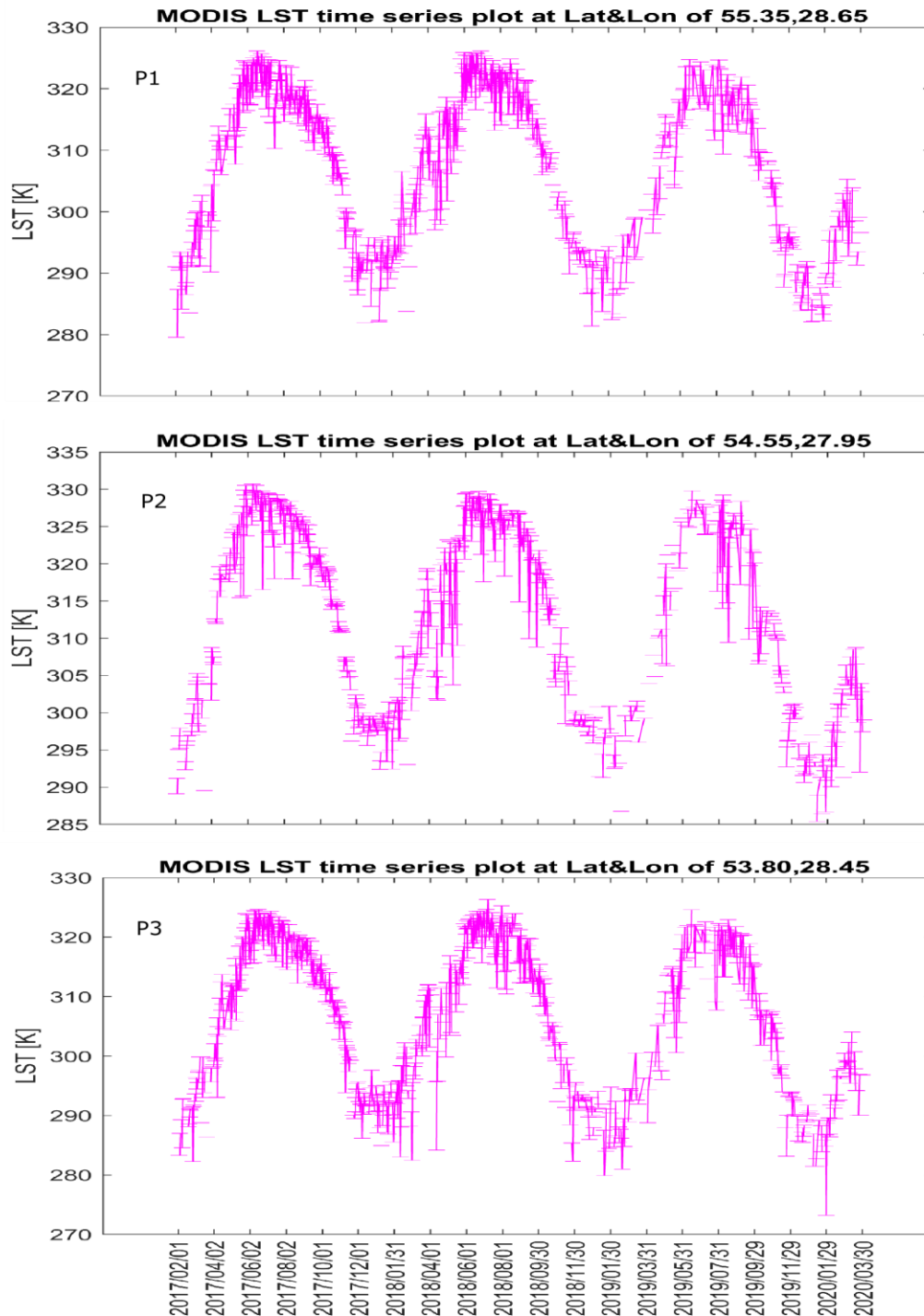


Figure (34): Time series plots of LST map from 13/December/2017 of MODIS daily data. (P1 is the point at Latitude of 28.65 and Longitude of 55.35. P2 represents the point at Latitude of 27.95 and Longitude of 54.55. P3 is the point at Latitude of 28.45 and Longitude of 53.80.)

The time series plots of P1, P2 and P3 points of Latitude and Longitude in Figure (33) of MODIS daily data are showing the seasonal trend with decrease in temperature globally like in Landsat-8. X-axis from P1, P2 and P3 from Figure (34) is representing vertical standard deviation error bars at each data point. The trend shows lower temperature in winter and higher temperatures in summer. As seen, P2 at Latitude of 27.95 and Longitude of 54.55 is showing the discontinuity of the data because of the presence of small ridges and valleys at the place compared to the other two points of Latitude and Longitude.

5.3.3 Time series analysis of Sentinel data:

For the time series analysis of Sentinel-3 data, both hourly data and 10-day data have been taken. Both have data for 24 hours a day. The following section explains how much missing data or gaps are present in the 24 hours of a day.

Sentinel-3 hourly data:

Sentinel-3 hourly data very advantageous as it is available hourly to overcome the issue of missing data/cloud cover. But the disadvantage is that it has 5km spatial resolution. Data was downloaded for the year of 2019 as shown in the Figure (35). Since the data is hourly data, the data acquisition for three years was time consuming. Generally, it is not possible to get the continuous data for 24 hours as there are clouds present at some point of the day. To check which time of the day has better continuity of data and less cloud coverage, the number of NaN values is calculated for each data set and plotted versus the time of the day as shown in Figure (35). This is done to avoid the download of all the data for all the hours in a day.

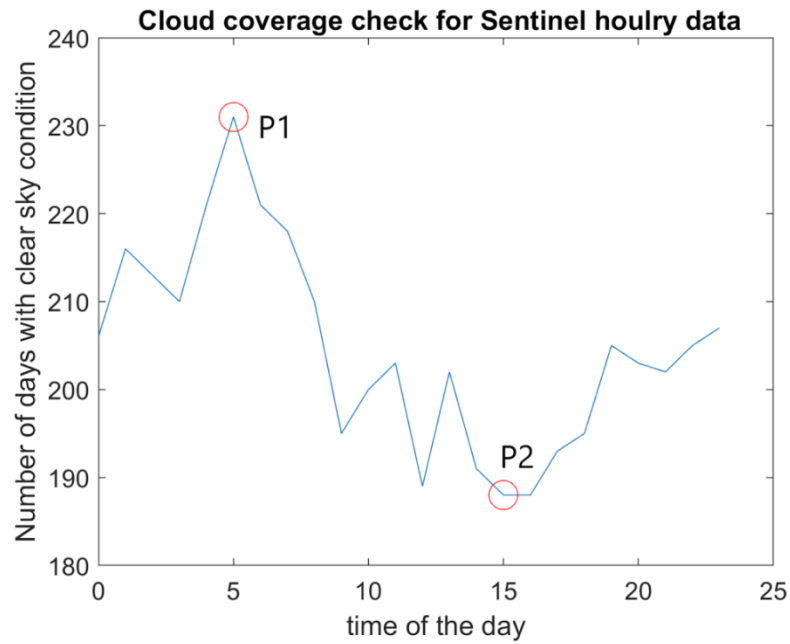


Figure (35): Sentinel hourly data representing number of days with more data availability w.r.t time of the day. P1 represents highest number of days with clear sky condition and P2 as lowest number of days with clear sky condition.

From the 35), it is shown that at P1(5AM), 230 days out of 235 days are with clear sky condition which means that the data availability is more at that time. P2 at 15 is showing the less data availability because of the cloud cover.

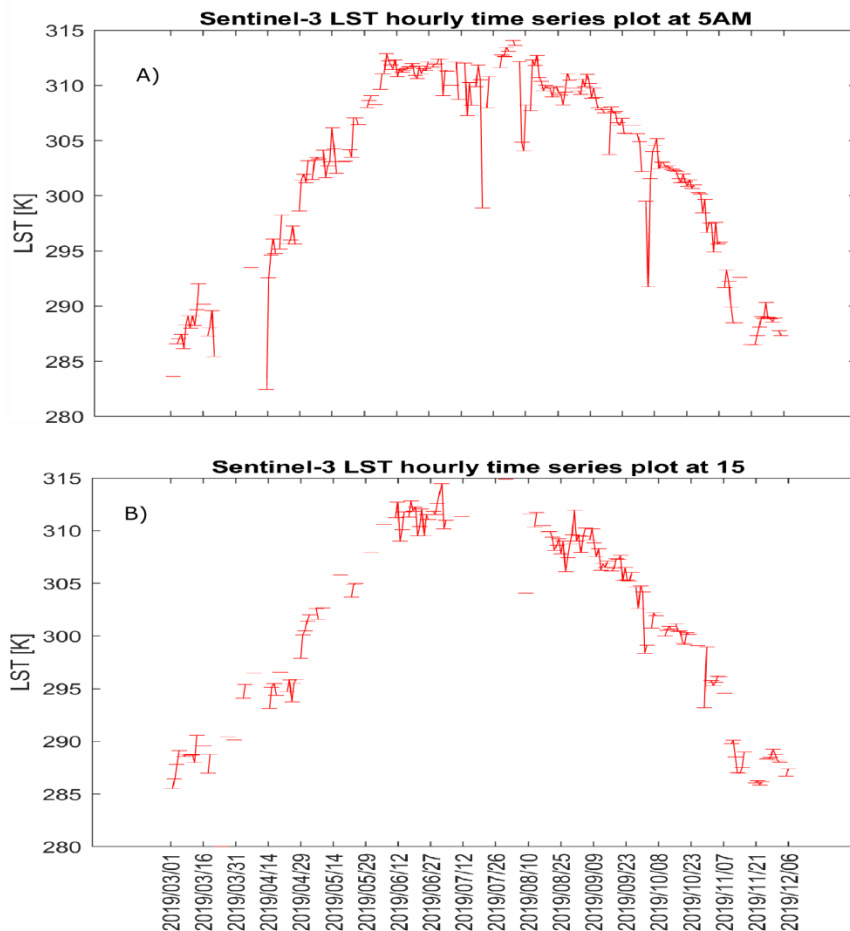
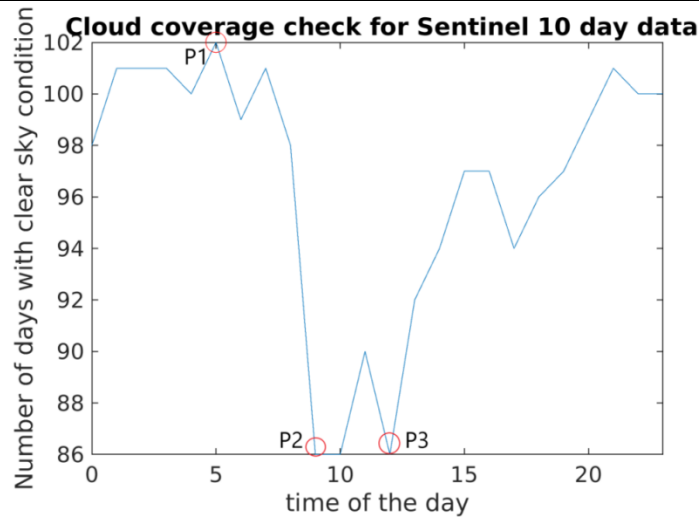


Figure (36): Time series of LST maps (a is the time series plot of LST at 5AM representing P1 from Figure (35). b is the time series plot of LST at 15 representing P2 from Figure (35)).

Figure (36) represents the time series plots plotted at 5 and 15, to show the difference visually. It can be seen clearly that the data availability from a is more than the data availability from b. This is because of the cloud cover when the satellite overpasses.

Sentinel-10 day data:

As the time series is to perform for three years, collecting the hourly data was a big challenge as it takes a long time to receive the ordered files. Instead, 10-day LST data from sentinel-3 with 24 hours was collected for three years. After the time series analysis and velocity calculation, it was realized that this data is not usable to check the thermal variation as there was not much LST data available around the study area. So again, the number of days with high data availability was calculated by considering the NaN values with respect to 24 hours. Surprisingly, 10-day LST data also showed more data availability at 5AM as shown in the Figure (37) below.



37): Sentinel 10 day data representing number of days with more data availability w.r.t time of the showing P1 as highest and P2 and P3 as lowest with clear sky condition

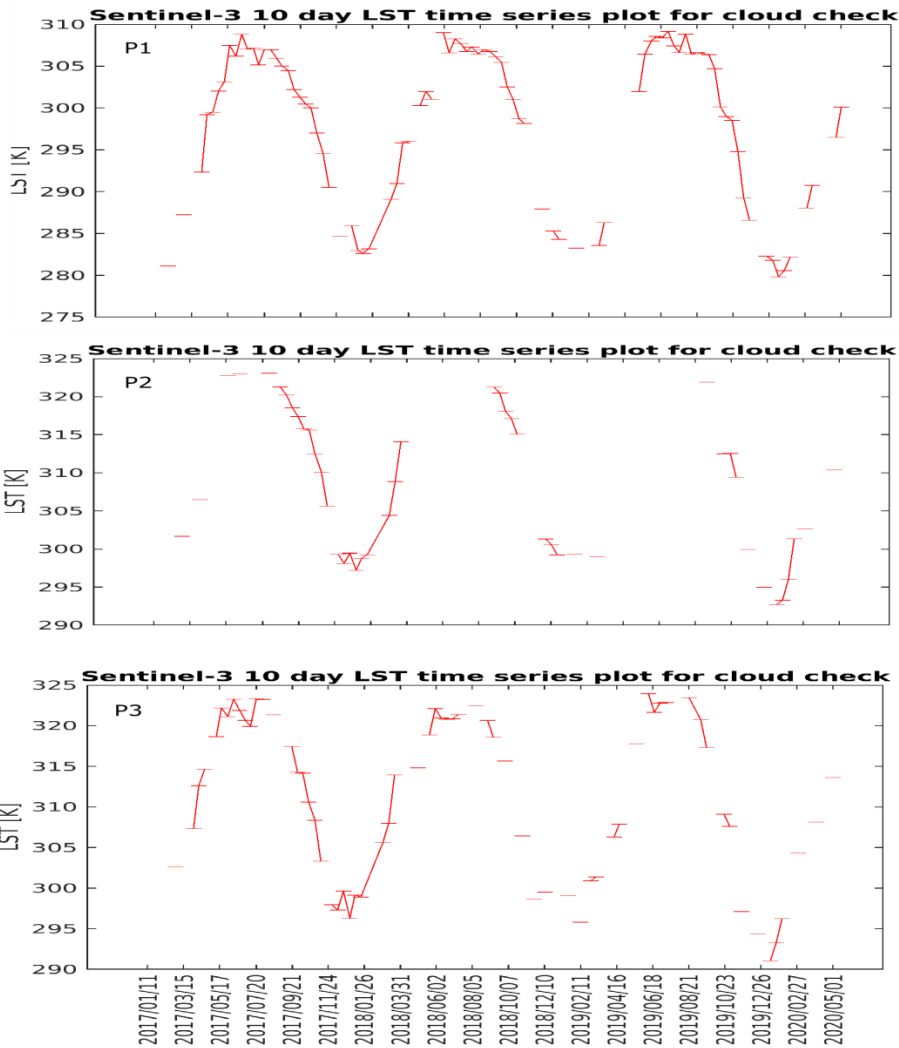


Figure (38): Time series of LST maps(P1 is the time series plot of LST at 5AM from Figure (35). P2 is the time series plot of LST at 9 from Figure (35). P3 is the time series plot of LST at 12 from Figure (35)).

Figure (38) is the time series plots of LST from Sentinel-3 10 day data. Time series plots for P1, P2 and P3 are shown and it is observed that the data availability is poor at 9 and 12 compared to 5AM. It can also be observed that the time series plot even at P1 (5AM) is also not continuous with data gaps present at more than 10 places over the three years. Because of this reason, Sentinel-3 10-day data is avoided to check for the thermal variations.

Sentinel daily LST data:

Sentinel-3 daily data is not available from the Copernicus Global Land Service. When checked for the high data availability during the day, both hourly data as well as 10-day data showed continuous data at 5AM, so it is selected as the best time of the day to get the data. So, daily LST data at 5AM for sentinel-3 was collected as it was effective in terms of data and time for the data acquisition.

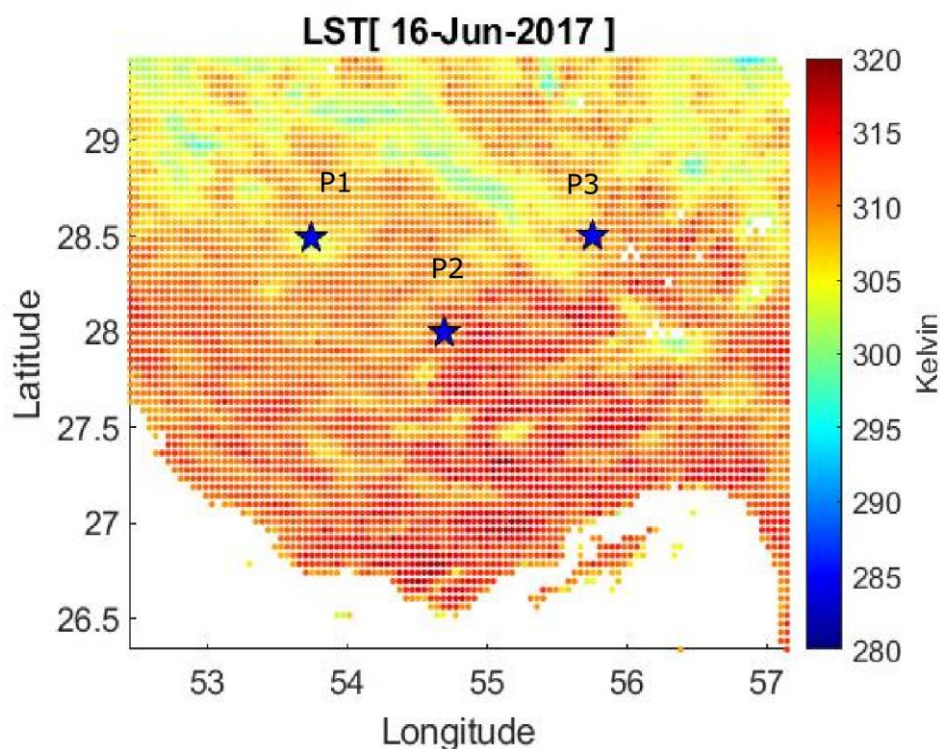


Figure (39): LST map of Sentinel-3 hourly data at 5 AM from 16/June/2017. P1, P2 and P3 represent the points of Latitude and Longitude.

The temperatures of LST map from Figure (39) are showing the values between 305K and 320K. As this is from the continental and arid climate, the summer starts

from the June month with slight decreasing of temperature. Less temperature is seen at some places in the LST map due to the vegetation of mountains.

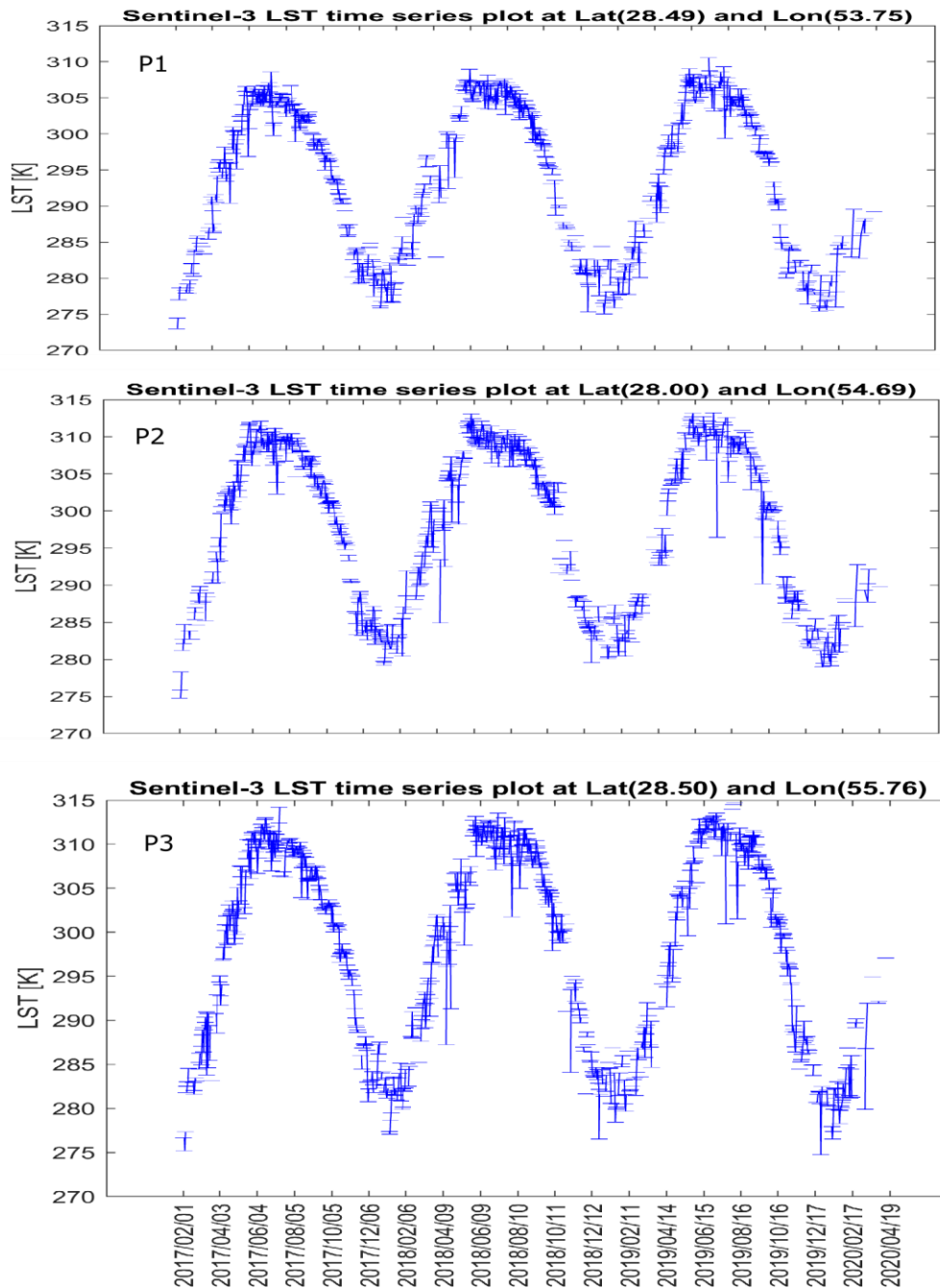


Figure (40): Time series of LST map from Figure (39). (P1 is the point at Latitude of 28.49 and Longitude of 53.75. P2 represents the point at Latitude of 28.00 and Longitude of 54.69. P3 is the point at Latitude of 28.50 and Longitude of 55.76.)

As it can be observed from the Figure (40), the time series plots of P1, P2 and P3 show the similar seasonal trend with few data gaps in between. In the year, 2018 at the month of October, both P2 and P3 show the missing data and same standard deviation for few data points but P1 shows the continuous data with different

standard deviation. As this data is obtained at 5Am for the three years, it may not be the best option to use this for the thermal variation with 5km spatial resolution.

5.4 Velocity of Temperature changes from MODIS and Sentinel-3:

The velocities of temperature change (m/year) were calculated for all datasets and plotted over the Longitude and Latitude. The velocity of temperature change represents the speed at which the LST changes over time. It is calculated using the linear regression fit on the time series by taking the observation equation as:

$$L = V \cdot t + b$$

Where L is the known dependent observation variable which is here LST,

V is the unknown velocity,

t is the time which is independent variable,

b is bias.

MODIS velocity map and profile

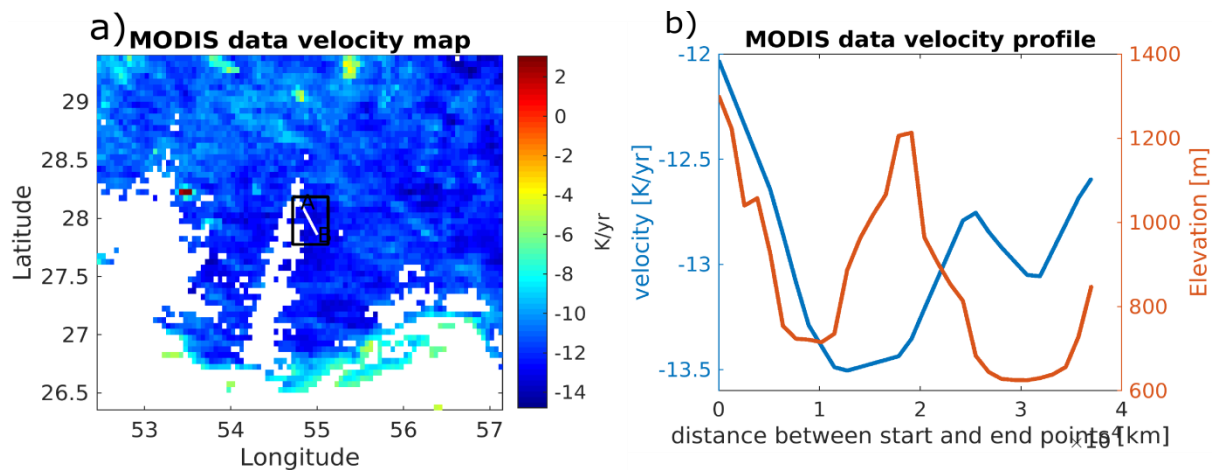


Figure (41): Velocity map (a) and velocity profile (b) of temperature change for MODIS daily data

Velocity values are calculated using linear regression and plotted over latitude and longitude. Negative velocities correspond to a negative LST trend and positive ones to a positive LST trend. The plot a in Figure (41) shows, great velocity change in temperature between -8km/year and -6km/year at the coastal area and also in the area where salt diapirs exist. It is seen from the plot b, that the velocity profile is plotted for the start and end point which are shown in the rectangle having the latitude from 27.857934 to 28.140503 and longitude from 54.802672 to 55.002825.

A is start point and B is the end point which are taken over the study area to observe the velocity. The velocity profile shows the continuity and trend similar to the DEM but there is no correlation between them. It means that there has been a great change in temperature.

Sentinel-3 velocity map and profile:

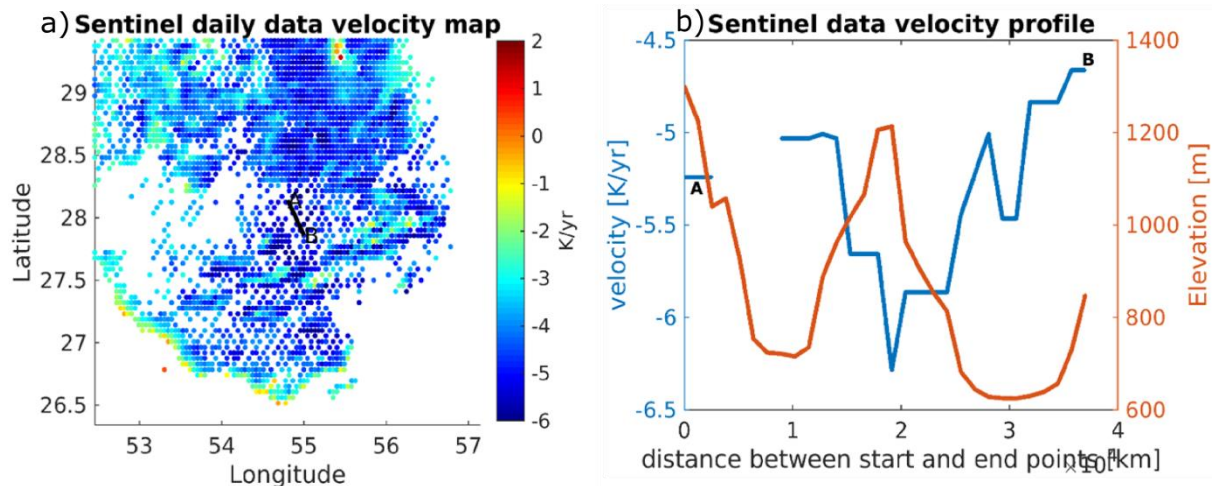


Figure (42): Velocity map (a) and velocity profile (b) of temperature change for Sentinel-3 LST data

The plot a in Figure (42) shows the velocity between -4 km/year and -1 km/year with lack of data in the study area. Negative velocities correspond to a negative LST trend and positive ones to a positive LST trend. Velocity profiles are drawn by calculating the Euclidean distance between the start point and end point represented by a line with A and B points in plot a with latitude from 27.857934 to 28.140503 and longitude from 54.802672 to 55.002825. It can be observed from plot b that the velocity profile has discontinuity due to the data gaps present over the salt dome. It has neither same trend as DEM or correlation between them.

5.5 Bias between Landsat-8 and MODIS:

Bias is calculated by taking the same reference point in MODIS and Landsat-8. Because of the data gaps, low spatial resolution (5km) and uncertainties, Sentinel-3 data is ignored for the thermal variations check and band pass decomposition. The Latitude and Longitude of the reference point is 27.95 and 54.95. The plots of uncorrected and corrected bias are shown in Figure (43).

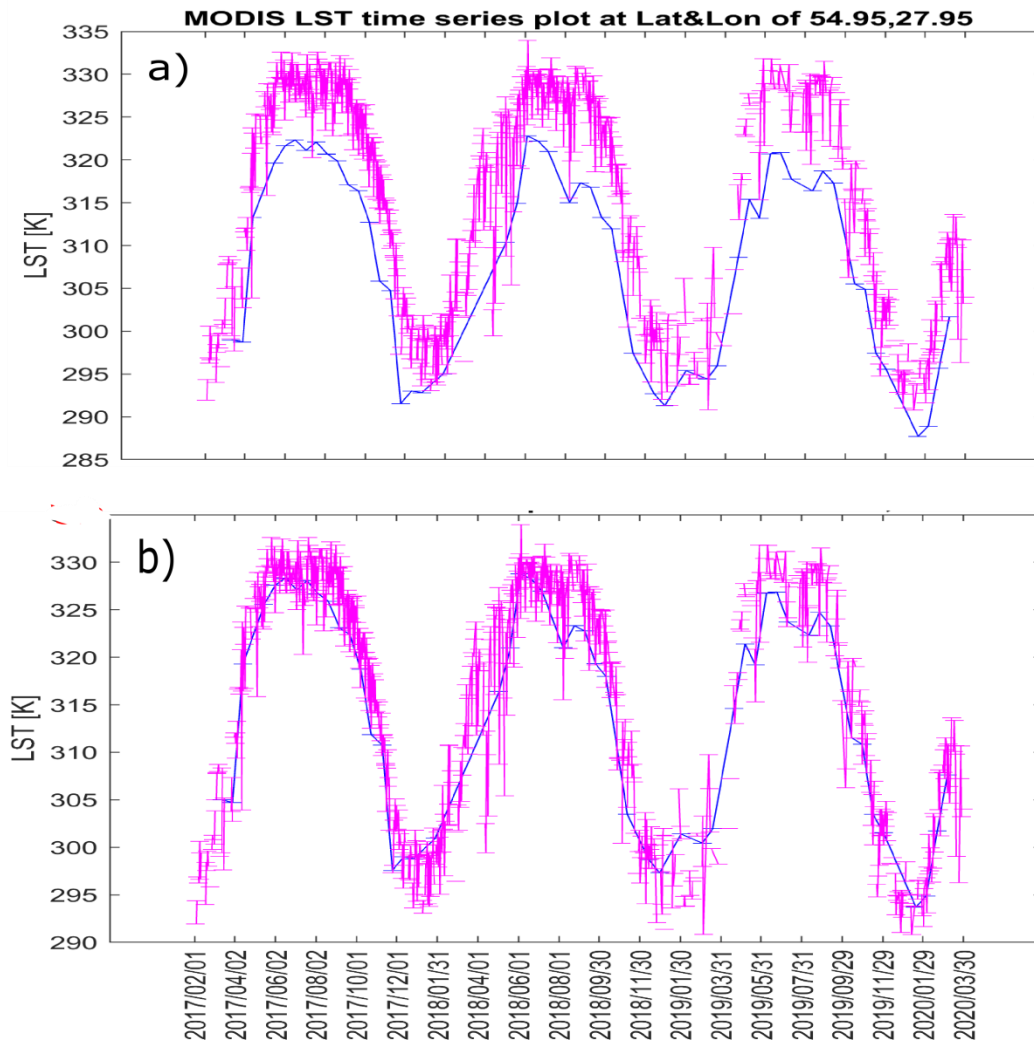


Figure (43): Bias between Landsat-8 and MODIS (A is uncorrected plot and B is corrected plot for bias)

Plot a in Figure (43) shows the time series plots of LST from Landsat-8 and MODIS. It can be seen that, there is bias between two of them but the trend is same showing the same seasonal effect. This bias is may be present due assumptions made while calculating LST for Landsat-8. MODIS data is taken as an accurate data, as the accuracy of daily MODIS LST products has been validated in more than 20 clear-sky cases with in situ measurement data collected in field. To remove the bias between them, $+6^{\circ}\text{C}$ manual temperature is added to Landsat -8 data. Plot b in 43) represents the correlated plot of MODIS and Landsat-8 after the removal of bias.

5.6 Band pass decomposition:

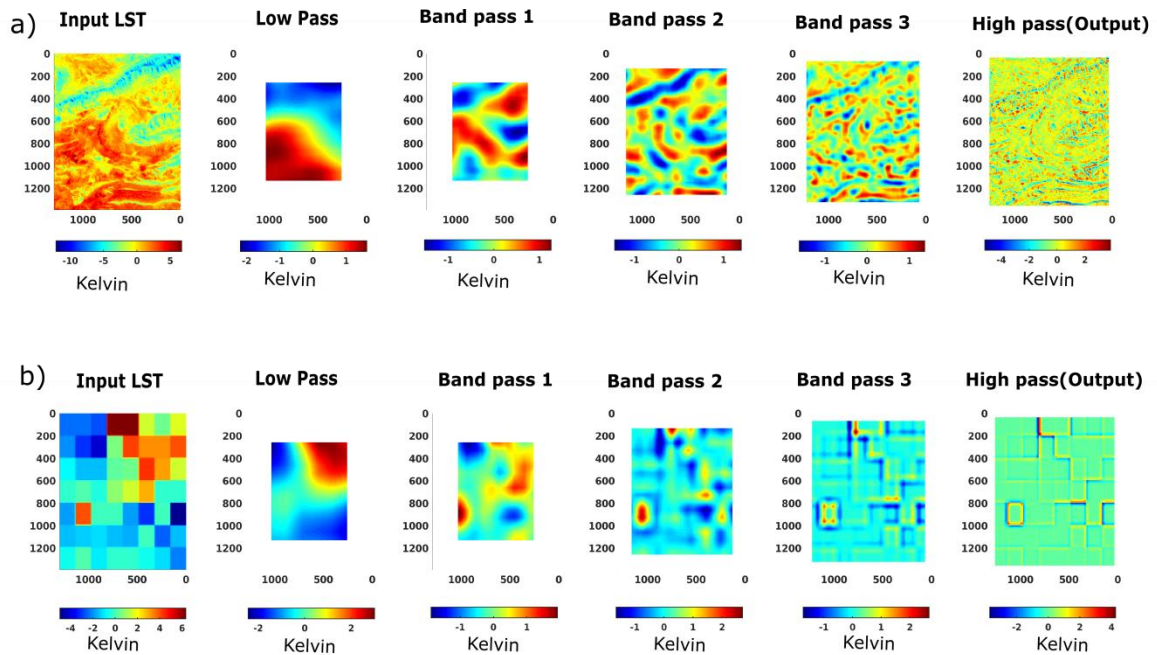


Figure (44): Band pass decomposition results from Landsat-8 (a) and MODIS (b)

The results of Band pass decomposition are represented for Landsat-8 and MODIS in Figure (44). For both Landsat and MODIS, 3 band passed images with Gaussian filter are generated along with one low pass image and one high pass image. The results from the Landsat are clear showing the fine details because of the fine resolution whereas MODIS are not showing the details of the study area because of the coarse resolution. In the next step, as the aim of the band pass decomposition is to combine the MODIS data and Landsat-8 data, Low pass image from Figure (44a) is replaced with the Low pass image from Figure (44b) and combined with the other band passed components. In this way, it is possible to preserve the details from MODIS and use the details from Landsat-8. In the final step, high pass image as a corrected LST map with accuracy almost equal to MODIS is produced with high resolution.

5.6.1 Corrected LST Map

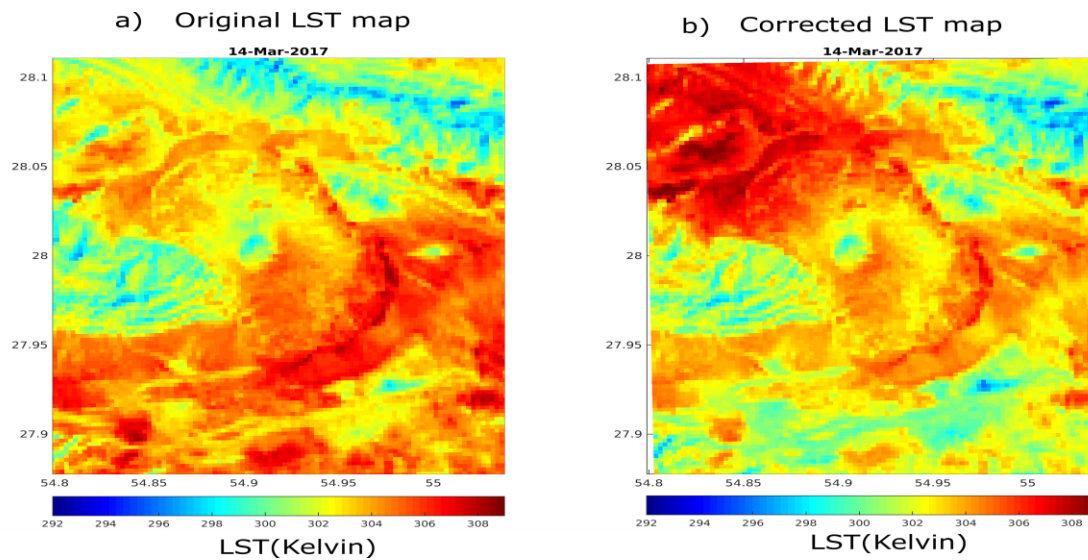


Figure (45): Original LST map (a) and corrected LST map (b)

In the above Figure (45), the difference between original LST map and corrected LST map is presented. Both these LST maps are produced for the date of 14/March/2017 to detect the differences clearly. It is observed that, the upper left corner of the corrected LST map has increased LST values than the original LST values while the lower right corner has decreased LST values than the original LST map.

5.6.2 Corrected Velocity Map

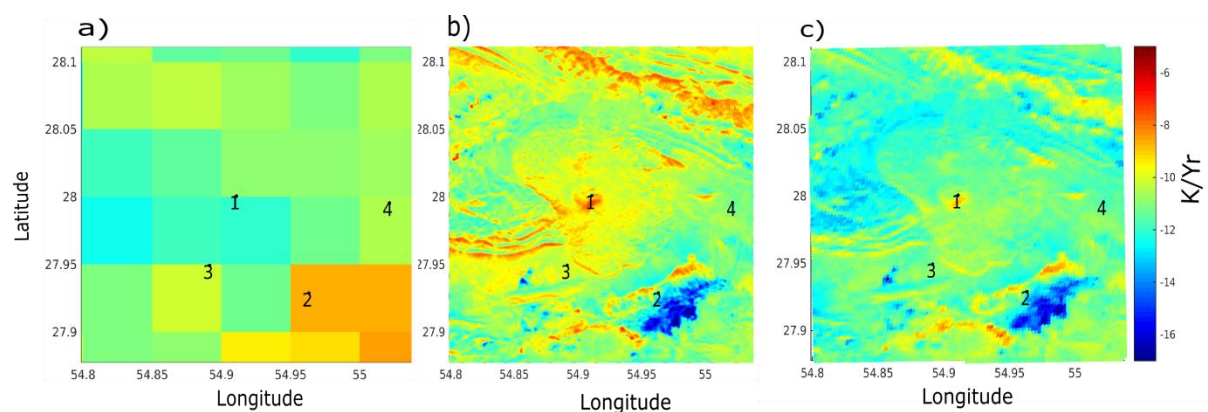


Figure (46): Velocity maps of MODIS (a), Landsat-8 (b), and corrected Landsat-8 (c) maps showing 4 points for the time series analysis.

Figure (46), plot a shows the velocity map of MODIS, which is cropped according to the Landsat-8 coordinates. This cropped region is shown in the rectangle in Figure (41) of MODIS velocity map. It is seen from plot a that, the area is pixelated when cropped into a small region and not showing any details of study area because of its coarse resolution. But the velocity map from Landsat-8 shown in plot b, shows very fine details including the topographical features. The corrected velocity map in plot c shows the similar variations as Landsat-8 velocity map but with the removed effects of topography. The high velocity change of temperature according to the velocity maps is lying between the -14K/yr and -8 K/yr . The points shown in the velocity maps are taken to perform the time series analysis of LST. These time series plots are shown in Figure (47)

5.6.3 Corrected Time series plots

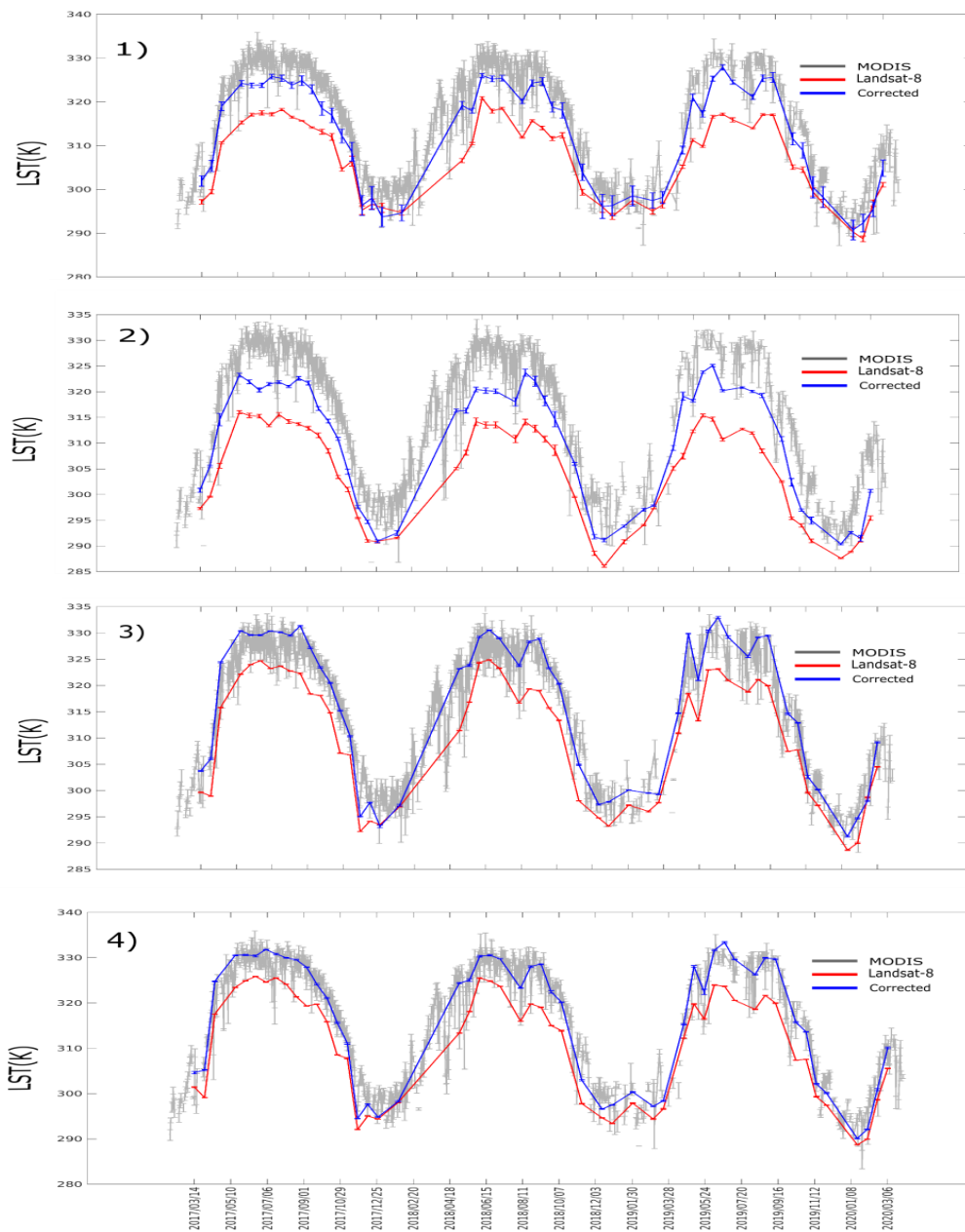


Figure (47): Time series analysis of LST from MODIS, Landsat-8, and corrected LST from bandpass decomposition (Plot 1 is the time series plot at Latitude of 28.00 and Longitude of 54.91, Plot 2 is at 27.92 and 54.96, Plot 3 is at 27.94 and 54.89, and Plot 4 is at 27.99 and 55.02 of Latitudes and Longitudes)

Figure (47) represents the time series plots of 4 points which are shown in Figure (46). It is to show the difference clearly between the time series plots of MODIS, Landsat-8 and corrected LST of Landsat-8. After the band pass decomposition, it is observed that the Landsat-8 data accuracy is increased and it is close to the MODIS data. It is because of the combination of low pass image from MODIS with the band pass and high pass images with Landsat-8. The Plot 1 and Plot 2 time series plots

from Figure (47), are taken in the study area show the difference in temperature values by $5^{\circ}\text{C}/5\text{K}$ and more standard deviation between MODIS time series and corrected LST of Landsat-8 time series, whereas the points P3 and P4 which are taken a little bit far from study area show neither difference between them nor standard deviation. The reason behind this is the thermal anomalies present in the salt dome. MODIS gives average LST data in one pixel for each 1km spatial area but the Landsat -8 gives LST data for every 100m thus there is a chance that the MODIS is missing the data.

5.7 InSAR time series:

5.7.1 SBAS time series of Deformation maps:

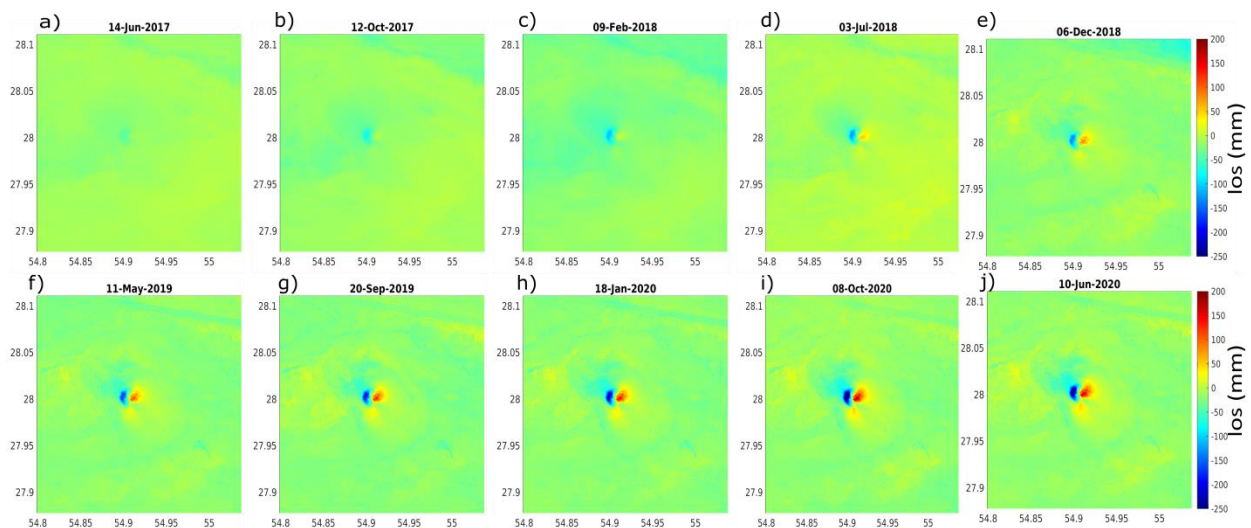
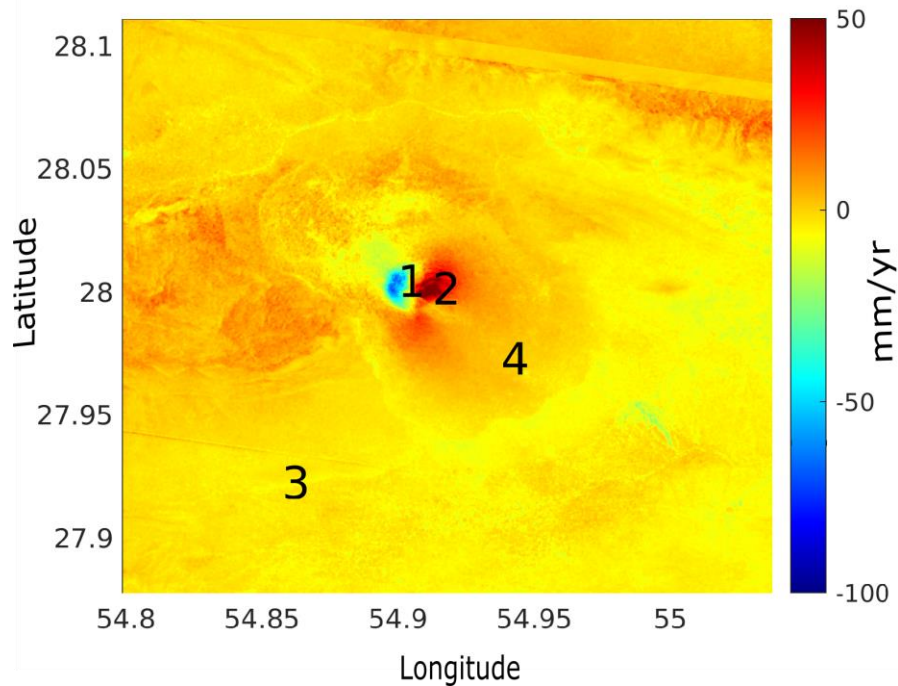


Figure (48): SBAS time series of Deformation maps in the direction of Line of Sight (LOS) (a is the deformation map produced from 14/June/2017, b from 12/October/2017, c from 09/February/2018, d from 03/July/2018, e from 06/December/2018, f from 11/May/2019, g from 20/September/2019, h from 18/January/2020, i from 08/October/2020 and h from 10/June/2020)

Deformation maps are produced in the direction of line of sight. Figure (48) contains the results of SBAS time series of deformation maps to analyse the deformation caused by the salt flow around the study area. Positive increase in deformation represents that uplift and negative increase represents subsidence. From these

figures, it is visible that the deformation is increasing each year. The red areas in the deformation maps correspond to the uplift while blue correspond to the subsidence.

5.7.2 Velocity map:



Figure(49): Velocity map of line of sight deformation representing 4 points for time series analysis

Velocity is estimated as the slope of the best fitting line to the displacement time-series. The velocity of deformation rate is high at the salt dome area (study area) showing subsidence at the marked point 1 with velocity change around -50mm/yr to -100 mm/yr and uplift at the marked point 2 with velocity change from 10mm/yr to 50mm/yr. The remaining area around the salt dome shows no velocity change of deformation rate.

5.7.3 Time series maps:

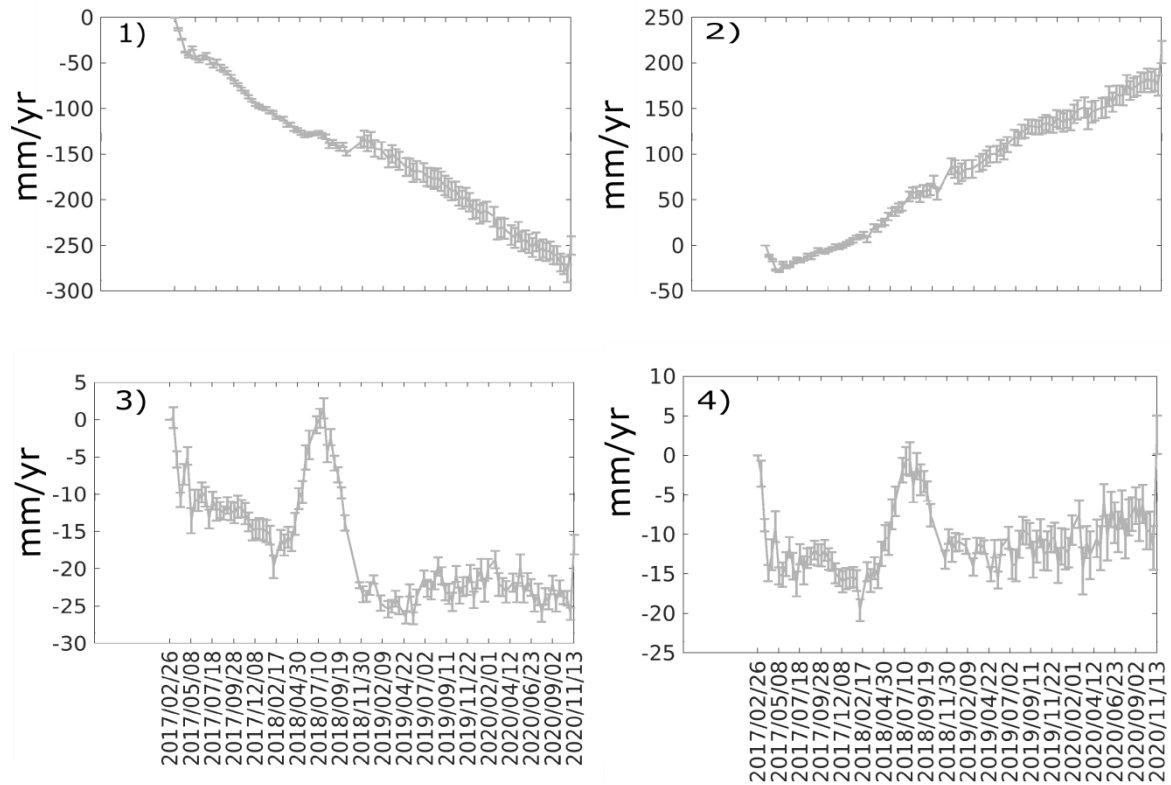


Figure (50): SBAS time series analysis of 4 points marked in Figure (49)

Figure (50) indicates the SBAS time series plots plotted for the marked points in Figure (49). Plot 1 shows the linear increase in left direction and interpreted as subsidence and plot 2 shows the linear increase in right direction which is interpreted as Uplift. Plot 3 and plot 4 show a sudden increase in deformation rate from 17/02/2018 to 30/11/2018 and became steady without any pumping effects till 13/11/2020. These changes in deformation are observed when the salt penetrates through the earth's surface creating a pressure which will lead to the tectonic processes of uplift/subsidence.

6. Conclusion:

The main aim of this study is to make use of the available satellite observations to analyze the thermal anomalies around the salt diapirs. The thermal anomalies are analyzed by utilizing Satellite based LST. The algorithm used in this study to retrieve the values of LST from Landsat-8 level-1 products gave the temperature values with a bias of + 6°C to the MODIS daily data products. This bias is due to the assumptions made on prior emissivity values while calculating the emissivity and the assumed values of NDVI of soil and NDVI of vegetation which are used to calculate the proportion of vegetation which later used for emissivity calculation. MODIS daily LST product is taken as a validated data as it has been validated in more than 20 clear-sky cases with in situ measurement data. It is worth noticing the fact that the spatial and temporal resolutions of the satellite play a crucial role in observing the thermal anomalies. As all LST data observations are optical satellite datasets, the differences in the distribution of spatial and temporal resolutions were sometimes driven by unfavorable observation environments during satellite overpasses such as high cloud cover and rapid changes in the weather resulting in the data gaps makes it difficult to analyze the thermal variations in long run with fine resolution.

LST maps and time series plots of LST maps show that Sentinel-3 LST data with 5km spatial resolution is providing the discontinuity in data. However, Landsat-8 and MODIS with fine and moderate resolutions gave the continuous data and showed the similar temperature changes and seasonal trend. From the time series analysis of MODIS, Landsat-8 and Sentinel-3, it is realized that the temperature is decreasing globally around the salt dome by 1°C each year.

The calculated velocity of temperature change from MODIS and Sentinel-3 shows more velocity change around the salt dome and the coastal areas and constant velocity in the remaining areas. Velocity profile drawn over the study area from A to B for MODIS data represented a similar trend as elevation data without any correlation. Even though the same Latitude and Longitude points (A and B) were chosen for the Sentinel-3 velocity profile, it failed to provide the continuous velocity profile because of the lack of data around the study area. This problem would have been solved by using the hourly LST data, but ordering and downloading takes more time particularly for the dense time series analysis like in this case. Velocity profile of MODIS showed high negative temperature change velocity around -12 K/year inside the study area and low negative temperature change velocity around -13 K/year around the study area. It is also interpreted that the temperature change velocity is directly proportional to the elevation data.

Band pass decomposition method which has been used to combine MODIS low spatial resolution data and Landsat-8 high spatial resolution data gave promising results by generating the corrected LST maps for all the Landsat-8 data and gave results with MODIS data accuracy where there is no salt activity.

Analyzing the time series of line of sight deformation maps at different location of the study area clarifies that there is an uplift deformation with the rate of 0.02 to 0.05 m/year and subsidence deformation with the rate of -0.05m/year 0.1mm/yr. This happens because of the 2 or 3 times high thermal conductivity of salt compared to the other sediments causing the salt to flow at normal temperature.

It is concluded that the optical data is more advantageous when provided with good spatial and temporal resolutions to analyze the thermal anomalies at region scale. Landsat-8 has fine resolution but direct LST products are not available and have to be retrieved. When LST is estimated, it has to be corrected with either in-situ temperature or with a reference data to be more accurate because of the separation problem of LSE and LST and topographic corrections.

7. Appendix:

7.1 Landsat Missions:

Landsat-1 was launched in July, 1972 and deactivated in January, 1978. It has two instruments namely, Return beam vidicon (RBV) and Multispectral systems (MSS) with S-band and Very high frequency (VHF) communications. It is a sun synchronous and near polar satellite, completes 14 orbits per day and with a repeat cycle of 18 days.

Landsat-2 was launched in January, 1975 and decommissioned in July, 1983. It is also a sun synchronous and polar satellite with two instruments like Landsat-1. It was a predecessor for Landsat-1 with the same specifications and the same instruments. All the data from Landsat-1 to 3 were acquired on Worldwide Reference System-1.

Landsat-3 is the same as Landsat-1 and Landsat-2 launched in March, 1978 and decommissioned in September, 1983. It is also a sun synchronous and polar satellite with 14 orbits per day and 18 days repeat cycle. The only difference is that the ground resolution has increased to 40m and RBV instrument has two cameras mounted side by side to operate in one spectral band while the MSS is maintained same as its predecessor.

Landsat-4 was launched in July, 1986 and decommissioned in June, 2001. Like the first three missions, it is also sun synchronous and near a polar satellite with altitude lesser than the predecessors. As it was in a lower orbit, it had a higher field of view (FOV) which resulted in acquiring the data in Worldwide Reference System-2. Unlike the first three missions, Landsat-4 had MSS and Thematic Mapper (TM) as instruments.

Landsat-5 was launched in March, 1984. It has set the Guinness book of world record as 'Longest Operating Earth Observation Satellite' for providing data for a long time and was decommissioned in June, 2013. It also has MSS and TM as instruments and specifications are the same like Landsat-4.

Landsat-6 was launched in October, 1993 as an improved version of Landsat-4 and Landsat-5 with sun synchronous and near polar satellite but unfortunately did not reach orbit.

Landsat-7 was launched in April, 1999. It acquires the data on Worldwide Reference System-2 and is sun synchronous near the polar satellite. Since 2003 because of the failure in Scan Line corrector (SLC), the acquired and delivered data has gaps. The below Figure (give number) gives clarity on how SLC works. SLC actually compensates for the forward motion of the satellite. It is expected to replace Landsat-7 by Landsat-9 when it is launched. It has Enhanced Thematic Mapper (ETM+) which includes eight spectral bands.

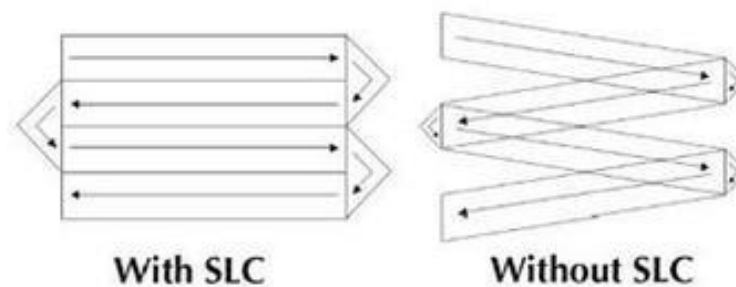


Figure (43): An illustration of how SLC works

Landsat-9 is expected to launch in mid-2021. It is being designed for 5 years of life time OLI and TIRS instruments. It will continue to provide the observations for global observations for monitoring, understanding, and managing Earth's natural resources.

7.2 Sentinel Missions:

- Sentinel-1: Sentinel-1 includes C-band imaging with different resolution (down to 5 m) and coverage (up to 400 km). It has dual polarisation capability, very short revisit times and rapid product delivery and also provides precise measurements of spacecraft position and attitude for each observation. It has the acquisition modes of Stripmap, Interferometric Wide Swath, Extra Wide Swath, and Wave. Sentinel-1A was launched in April, 2014 followed by Sentinel-1B which was launched in April, 2016. These two share the same orbital plane and have applications in Land and Ocean monitoring to acquire imagery regardless of weather and for emergency management.
- Sentinel-2: Sentinel-2 has a constellation of two satellites Sentinel-2A and Sentinel-2B. The first was launched in June, 2015 followed by the latter in March, 2017. They both are the same sun-synchronous orbit, phased at 180° to each other. These are polar-orbiting, all-weather, day-and-night radar

imaging missions for Land monitoring to obtain the imagery of vegetation, soil, and coastal areas.

- Sentinel-3: Sentinel-3 was launched in February, 2016 as a multi instrument mission to study marine observation and also to study the sea-surface topography, sea and land surface temperature, ocean, and land colour. More details about this mission is mentioned in the below section.
- Sentinel-5 precursor: It is also called Sentinel-5P. It's launched in October, 2017 to monitor our atmosphere. It provides the data related to the atmosphere like timely data on a multitude of trace gases and aerosols affecting air quality and climate.
- Sentinel-4: This mission is run by the ESA together with the European Environment Agency (EEA). It provides data with high spatial resolution and with a fast revisit time to monitor air quality trace gases and aerosols over Europe in support of the Copernicus Atmosphere Monitoring Service (CAMS). The key air quality parameters are NO₂ (nitrogen dioxide), O₃ (ozone), SO₂ (sulphur dioxide), HCHO (formaldehyde), CHOCHO (glyoxal), and aerosols.
- Sentinel-5: This mission is a part of the Copernicus programme and run by the European Commission (EC). Sentinel-5 is a low earth orbit mission with high temporal and spatial resolution with 29-day repeat cycle for monitoring atmospheric chemistry. The main applications are ozone and surface UV, air quality, and climate and data products being O₃, NO₂, SO₂, HCHO, CO, CH₄ and aerosol optical depth.
- Sentinel-6: Copernicus Sentinel-6A is expected to launch in November, 2020 while Sentinel-6B in 2025. It has a 10 day revisit time and life time of minimum 5.5 years with instruments including Poseidon-4 radar altimeter and a microwave radiometer. The main application of this is to continue the long-term record of sea-surface height measurements and to provide data for operational oceanography.

The missions SENTINEL-4, -5 and -5 precursor cover ozone and surface UV, air quality, and climate applications and provide coherent information on atmospheric variables in support of European policies. This serves as complementary elements of a constellation serving the specific needs of the Copernicus Atmospheric Monitoring Services (CAMS).

7.3 Sentinel-3 Instruments:

- SAR Radar Altimeter (SRAL): It is dual-frequency SAR altimeter and comprises one nadir-looking antenna, externally mounted on the satellite's +Zs Earth panel, and a central electronic chain composed of a Digital Processing Unit (DPU) and a Radio Frequency Unit (RFU). It is the main topographic instrument for topographic measurements of the ocean and inland water. SRAL includes measurement, calibration and support modes and the measurement modes are composed of two radar modes combined with two tracking modes

Radar Modes	Tracking Modes
Low-Resolution Mode (LRM): conventional altimeter pulse-limited mode based on a 3 Ku / 1 C / 3 Ku pulse pattern.	Closed-loop mode: autonomous positioning of the range window using the median algorithm.
SAR mode: high along track resolution mode composed of bursts of 64 Ku-band pulses surrounded by two C-band pulses.	Open-loop mode: range window position based on a priori knowledge of terrain altitude derived from a Digital Elevation Model (DEM).

Table (9): The SRAL measurement modes

The calibration modes are responsible for measurement of the internal instrument impulse response (by looping back a fraction of the transmit signal). It also derives the transfer function of the receiving chain which is calculated from the acquisition and averaging of thousands of noise samples.

- Ocean and Land Color Instrument (OLCI): It is based on the opto-mechanical and imaging design of ENVISAT's MERIS instrument. Uses a push-broom imaging spectrometer instrument and uses five cameras to provide a wide field of view.

swath width	1 270 km
spatial sampling	300 m @ SSP
spectrum	21 bands [0.4-1.02] μm
radiometric accuracy	2% abs, 0.1% rel
launch mass	153 kg
size	1.3 m ³
design lifetime	7.5 years.

Table (10): Main characteristics of the OLCI

- Microwave Radiometer (MWR) instrument: By providing wet atmosphere correction, MWR supports the SRAL in getting altimeter mission performance and measures water vapor, cloud water content and thermal radiation emitted by the Earth. This instrument is the one which measures brightness temperature which is used to calculate LST. This measures brightness temperature at 23.8 GHz and 36.5 GHz covering a bandwidth of 200 MHz in each channel. The lower frequency channel is mostly sensitive to atmospheric water vapor while the higher frequency channel is sensitive to cloud liquid water.
- Precise Orbit Determination: It is a part of the Copernicus Payload Data Ground Segment (PDGS) and in charge of the Precise Orbital Products and auxiliary data files. It's a package which includes a Global Navigation Satellite Systems (GNSS) instrument, a Doppler Orbit determination and Radio-positioning Integrated on Satellite (DORIS) instrument and a Laser Retro-Reflector (LRR).
- LRR (Laser Retro Reflector): LLR is a passive device used as a target for the laser tracking measurements performed by the ground stations. It is fixed on the earth panel of the satellite and consists of a hemispherical array of seven corner cubes. These cubes reflect back the signals coming from ground stations in the same direction. The hemispherical arrangement makes sure that at least one cube is visible to any station that has satellites in view aiming

to give the range measurements with millimeter accuracy, by measuring the propagation delay of a laser pulse from the station to the LRR and back.

- GNSS (Global Navigation Satellite System): GNSS receiver has an antenna, the harness and the receiver itself. It gives real time radial position data by taking into account the satellite control and open loop mode of the altimeter. It also proves the accurate on board timing. Sentinel-3A and Sentinel-3B can track up to eight satellites and two signal bands in parallel.

7.4 InSAR:

Synthetic aperture radar (SAR) is an active sensor that first transmits microwave signals and then receives back the signals that are returned, or backscattered, from the Earth's surface. A SAR signal contains amplitude and phase information. Amplitude is the strength of the radar response and phase is the fraction of one complete sine wave cycle (a single SAR wavelength). The phase of the SAR image is determined primarily by the distance between the satellite antenna and the ground targets.

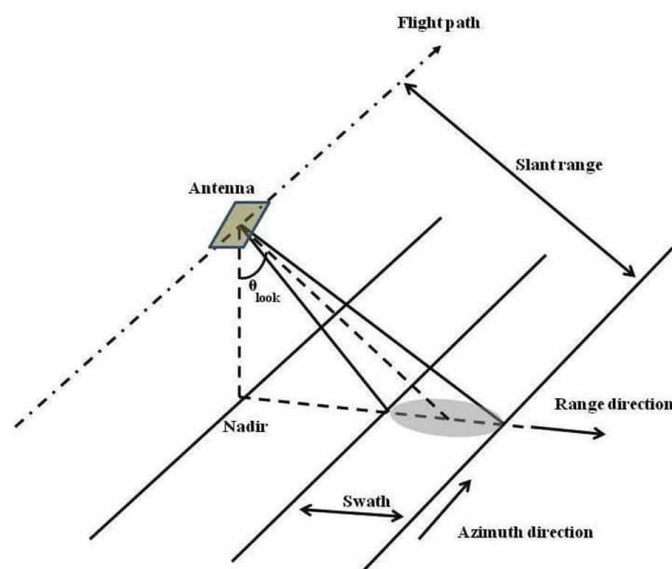


Figure (44): A typical side-looking radar pointing perpendicular to the flight direction. Credit: NASA.

Interferometric SAR (InSAR) exploits the phase difference between two complex radar SAR observations of the same area (one usually regarded as master and the

other slave), taken from slightly different sensor positions, and extracts distance information about the Earth's terrain. Both are combined to produce a phase interference image called an interferogram (Dixon, 1994; Massonnet, 1997; Zebker and Goldstein, 1986).

In simple words, an interferogram is a colorful representation of topography and change. SAR images consist of both magnitude (brightness) and phase values. Often the phase information is thrown away; however, if it is retained, the SAR image is described as being complex (Henderson and Lewis, 1998).

The phase in a complex SAR image is a coherent signal containing information about the distance between a resolution cell on the ground and the radar antenna, as well as information about the texture of terrain within a resolution cell. Using the phase information in the interferogram, it is possible to extract topographic height information (DEM), height change information, and fine scale temporal change measurements (Burgmann et al., 2000; Okeke, 2005).

However, the processing of InSAR data is still a challenging task. The important risks to the InSAR data quality are temporal decorrelation and atmospheric effects (Henderson and Lewis, 1998). Temporal decorrelation is indicated as low coherence image. For each selected image pair, several processing steps such as pre-processing, co-registration and resampling, computation of Interferogram, Phase unwrapping, and Geocoding have to be performed. The selection of the images can be made on the basis of baseline length and the time period between two image acquisitions which depends upon the application and the spatial resolution of the data. For example, in the case of ERS-1 and 2, the baseline may be taken as 150 to 300m for topographic applications, 30 to 50m for surface change detection and up to 5m for surface feature movement studies such as crustal deformations, lithospheric movements, movement of glaciers and etc. (Burgmann et al., 2000).

InSAR processing from both Single Look Complex (SLC) images include five steps as mentioned in the flow chart():

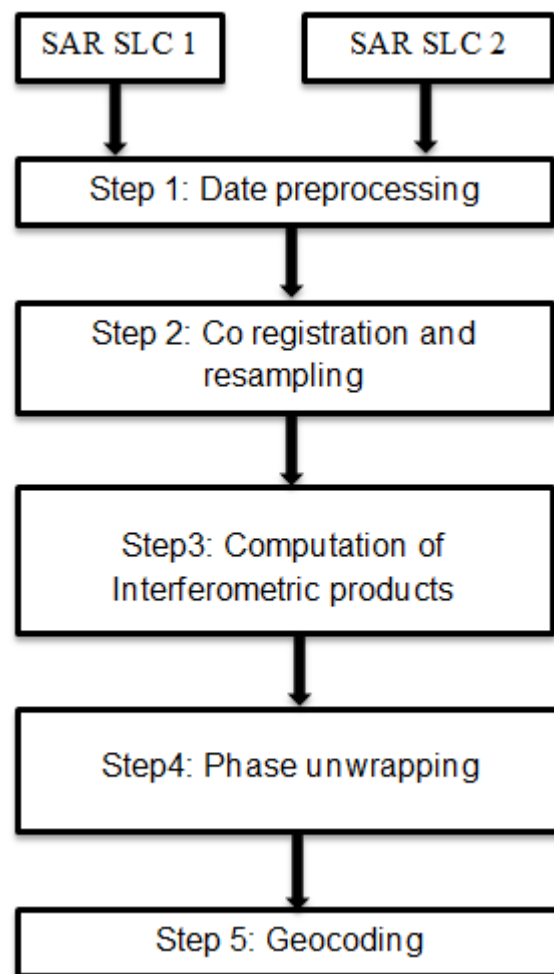


Figure (45): Flowchart of InSAR processing steps

Step1: Data pre-processing:

SLC indicates that each pixel corresponds to a single look and is a complex number. SLC images can have different formats. In this step, the SLCs must be transcribed from support media and put in a format that is understood by the interferometric processor. If necessary the orbit state vectors should be improved by interpolation method with available state vectors. Radiometric calibration of intensity images should be performed to adjust the magnitude level of the image.

Step2: Co-registration and resampling:

Co-registration step is required so that corresponding pixels in the two images perfectly match. Co-registration typically consists of computation of offsets between the two SLCs and resampling one SLC in order to match with the reference image. The offsets are used to determine the coefficients of the interpolation function needed to resample the slave image to master image grid. The precise co-registration increases the coherence of the interferogram, improves the quality of the phase unwrapping procedure, and leads to a more accurate phase in the final interferogram.

Step3: Computation of Interferometric products:

The complex interferogram is obtained from the cross-product of the co-registered SLCs and after common-band filtering. The interferogram consists of magnitude (correlation between images) and phase (InSAR phase). The correlation indicates how accurate the phase information is (fringe visibility). The lower the correlation, the noisier the phase. The InSAR phase is a combination of several contributions.

$$\phi = \phi_{\text{flat earth}} + \phi_{\text{topography}} + \phi_{\text{displacement}} + \phi_{\text{delay}} + \phi_{\text{noise}}$$

The phase is wrapped here so the InSAR phase has values between 0 and 2π .

Step4: Phase unwrapping:

Since the interferometric phase is wrapped between 0 and 2π , an integer number of 2π has to be added to recover the absolute phase difference. Unwrapping the phase means adding a correct multiple of 2π to the interferometric phase for each pixel in order to obtain sequential phase values across the entire image.

Step5: Geo coding:

In this step the unwrapped phase is converted to a height, and the pixel co-ordinates are geo referenced. The output of this step is the height for a large number of pixels at an irregular grid of longitude, latitude pair.

References:

- Louis Giglio, 2016 Giglio, Louis & Schroeder, Wilfrid & Justice, Christopher. (2016). The collection 6 MODIS active fire detection algorithm and fire products. *Remote Sensing of Environment*. 178. 31-41. 10.1016/j.rse.2016.02.054.
- Barsi, 2014 Barsi, Julia & Schott, John & Hook, Simon & Raqueno, Nina & Markham, Brian & Radocinski, Robert. (2014). Landsat-8 Thermal Infrared Sensor (TIRS) Vicarious Radiometric Calibration. *Remote Sensing*. 6. 11607-11626. 10.3390/rs61111607.
- Joshi, 2016 Joshi, Neha & Baumann, Matthias & Ehammer, Andrea & Fensholt, Rasmus & Grogan, Kenneth & Hostert, Patrick & Jepsen, Martin & Kuemmerle, Tobias & Meyfroidt, Patrick & Mitchard, Edward & Reiche, Johannes & Ryan, Casey & Waske, Björn. (2016). A Review of the Application of Optical and Radar Remote Sensing Data Fusion to Land Use Mapping and Monitoring. *Remote Sensing*. 8. 70. 10.3390/rs8010070.
- Mia, 2017 Mia, Md & Fujimitsu, Yasuhiro & Nishijima, Jun. (2017). Thermal Activity Monitoring of an Active Volcano Using Landsat 8/OLI-TIRS Sensor Images: A Case Study at the Aso Volcanic Area in Southwest Japan. *Geosciences*. 7. 118. 10.3390/geosciences7040118.
- Avdan, 2016 Avdan, Ugur & Jovanovska Kaplan, Gordana. (2016). Algorithm for Automated Mapping of Land Surface Temperature Using LANDSAT 8 Satellite Data. *Journal of Sensors*. 2016. 1-8. 10.1155/2016/1480307.
- Zhao-Liang Li, 2013 Zhao-Liang Li , Hua Wu , Ning Wang , Shi Qiu , José A. Sobrino , Zhengming Wan , Bo-Hui Tang & Guangjian Yan (2013) Land surface emissivity retrieval from satellite data, *International Journal of Remote Sensing*, 34:9-10, 3084-3127, DOI: 10.1080/01431161.2012.716540
- Md Shahid Latif, 2014 Latif, M.S. (2014) Land Surface Temperature Retrieval of Landsat-8 Data Using Split Window Algorithm—A Case Study of Ranchi District. *International Journal of Engineering Development and Research*, 2, 3840-3849.

-
- Cedeño, 2019 Cedeño, Andres & Rojo, Luis Alberto & Cardozo, Nestor & Centeno, Luis & Escalona, Alejandro. (2019). The Impact of Salt Tectonics on the Thermal Evolution and the Petroleum System of Confined Rift Basins: Insights from Basin Modeling of the Nordkapp Basin, Norwegian Barents Sea. *Geosciences*. 9. 316. 10.3390/geosciences9070316.
- Hazaymeh, 2015 Hazaymeh, Khaled & Hassan, Quazi. (2015). Fusion of MODIS and Landsat-8 Surface Temperature Images: A New Approach. *PloS one*. 10. 10.1371/journal.pone.0117755.
- Mehta, 2018 Mehta, Saaransh. (2018). Classification of high-resolution Landsat-8 time series by using lower resolution reference data. 10.13140/RG.2.2.33962.06089.
- Sofan, 2019 Sofan, Parwati & Bruce, David & Jones, Eriita & Marsden, Jackie. (2019). Detection and Validation of Tropical Peatland Flaming and Smouldering Using Landsat-8 SWIR and TIRS Bands. *Remote Sensing*. 11. 29. 10.3390/rs11040465.
- Xiong, 2009 Xiong, Xiaoxiong & Wenny, Brian & Barnes, William. (2009). Overview of NASA Earth Observing Systems Terra and Aqua moderate resolution imaging spectroradiometer instrument calibration algorithms and on-orbit performance. *Journal of Applied Remote Sensing*. 3. 10.1117/1.3180864.
- Banskota, 2014 Banskota, Asim & Kayastha, Nilam & Falkowski, Michael & Wulder, Michael & Froese, Robert & White, Joanne. (2014). Forest Monitoring Using Landsat Time Series Data: A Review. *Canadian Journal of Remote Sensing*. 40. 362-384. 10.1080/07038992.2014.987376.
- Talbot, 1980 Talbot, Christopher & Rogers, Eric. (1980). Seasonal Movements in a Salt Glacier in Iran. *Science (New York, N.Y.)*. 208. 395-7. 10.1126/science.208.4442.395.
- Lwin, 2010 Lwin, Ko. (2010). Estimation of Landsat TM Surface Temperature Using ERDAS Imagine Spatial Modeler.

-
- Sobrino, 2012 Sobrino, Jose & Jimenez-Munoz, Juan-Carlos & Brockmann, Carsten & Ruescas, Ana & Danne, Olaf & North, P.R.J. & Heckel, Andreas & Davies, William & Berger, Michael & Merchant, C. & Mitraka, Zina & Sòria Barres, Guillem. (2012). LAND SURFACE TEMPERATURE RETRIEVAL FROM SENTINEL 2 AND 3 MISSIONS.
- Meng, 2019 Meng, Xiangchen & Cheng, Jie & Cheng, Jie & Zhao, Shaohua & Liu, Sihan. (2019). Estimating Land Surface Temperature from Landsat-8 Data using the NOAA JPSS Enterprise Algorithm. *Remote Sensing*. 11. 155. 10.3390/rs11020155.
- Dalibor, 2015 Ficker, T. & Martišek, Dalibor. (2015). 3D Image Reconstructions and the Nyquist–Shannon Theorem. *3D Research*. 6. 10.1007/s13319-015-0057-4.
- Lin, 2010 Lin, Yu-nung & Simons, Mark & Hetland, E. & Musé, Pablo & DiCaprio, Christopher. (2010). A multiscale approach to estimating topographically correlated propagation delays in radar interferograms. *Geochemistry Geophysics Geosystems*. 11. 10.1029/2010GC003228.
- Zabolotskikh, 2019 Zabolotskikh, Elizaveta & Chapron, B.. (2019). Comparison of Satellite Products on Total Atmospheric Water Vapor Content over the Arctic Sea Ice. 2204-2209. 10.1109/PIERS-Spring46901.2019.9017852.
- Mechri, 2016 Mechri, Rihab & Otle, Catherine & Pannekoucke, Olivier & Kallel, Abdelaziz & Maignan, Fabienne & Dominique, Courault & Trigo, Isabel. (2016). Downscaling Meteosat Land Surface Temperature over a Heterogeneous Landscape Using a Data Assimilation Approach. *Remote Sensing*. 8. 586. 10.3390/rs8070586.
- Kallel, 2013 Kallel, Abdelaziz & Otle, Catherine & le hégarat, Sylvie & Maignan, Fabienne & Dominique, Courault. (2013). Surface Temperature Downscaling From Multiresolution Instruments Based on Markov Models. *Geoscience and Remote Sensing, IEEE Transactions on*. 51. 1588-1612. 10.1109/TGRS.2012.2207461.
- Peng, 2017 Peng, J., A. Loew, O. Merlin, and N. E. C. Verhoest (2017), A review of spatial downscaling of satellite remotely sensed soil moisture, *Rev. Geophys.*, 55, 341-366, doi:10.1002/2016RG000543

-
- Hutengs, 2014 Hutengs, Christopher & Vohland, Michael. (2014). Downscaling land surface temperatures from MODIS data to mesoscale resolution with Random Forest regression.
- Mechri, 2014 Mechri, R., C. Ottlé, O. Pannekoucke, and A. Kallel (2014), Genetic particle filter application to land surface temperature downscaling, *J. Geophys. Res. Atmos.*, 119, 2131–2146, doi:10.1002/2013JD020354.
- Por, 2019 Por, Emiel, et al. “Nyquist–Shannon Sampling Theorem.” May 2019.
- Wan, 2013 Wan, Zhengming. “Collection-6 MODIS Land Surface Temperature Products Users' Guide.” Dec. 2013.
- Rawat, 2018 Rawat, Kishan Singh, et al. “The Egyptian Journal of Remote Sensing and Space Sciences.” Dec. 2018.
- Selig and Wallick, 1966 J. Vizgirda, J.J. O'Brien, I. Lerche, Thermal anomalies on the flanks of a salt dome, *Geothermics*, Volume 14, Issue 4, 1985, Pages 553-565, ISSN 0375-6505.
- Jensen, 1983 Kenneth Petersen, Ian Lerche, Quantification of thermal anomalies in sediments around salt structures, *Geothermics*, Volume 24, Issue 2, 1995, Pages 253-268, ISSN 0375-6505.
- Berardino et al., 2002 Berardino, Paolo & Fornaro, Gianfranco & Lanari, Riccardo & Sansosti, Eugenio. (2002). A New Algorithm for Surface Deformation Monitoring Based on Small Baseline Differential SAR Interferograms. *Geoscience and Remote Sensing, IEEE Transactions on.* 40. 2375 - 2383. 10.1109/TGRS.2002.803792.
- Sentinel.esa.int [https://sentinel.esa.int/web/sentinel/user-guides/sentinel-3-slstr/overview/geophysical-measurements/land-surface-temperature#:~:text=Land%20Surface%20Temperature%20%2D%20Applications%20%2D%20Sentinel%2D3%20SLSTR%20%2D%20Sentinel%20Online&text=Land%20Surface%20Temperature%20\(LST\)%20is,land%20derived%20from%20infrared%20radiation.](https://sentinel.esa.int/web/sentinel/user-guides/sentinel-3-slstr/overview/geophysical-measurements/land-surface-temperature#:~:text=Land%20Surface%20Temperature%20%2D%20Applications%20%2D%20Sentinel%2D3%20SLSTR%20%2D%20Sentinel%20Online&text=Land%20Surface%20Temperature%20(LST)%20is,land%20derived%20from%20infrared%20radiation.)
- Britannica.com <https://www.britannica.com/science/salt-dome/Origin-of-salt-domes>

M. Pollyea, 2018	M. Pollyea, R. (n.d.). Advective Heat Transport and the Salt Chimney Effect: A Numerical Analysis. <i>Geofluids</i> , 2018.
Landsat 8 User Hand book	https://www.usgs.gov/core-science-systems/nli/landsat/landsat-8-data-users-handbook
Razaghian, G, 2015	Razaghian, G. and Arian, M. (2015) The Emergent Salt Diapirs in the East Zagros, Iran. <i>Open Journal of Geology</i> , 5, 718-726.
Frank J. Peel,2014	Frank J. Peel, How do salt withdrawal minibasins form? Insights from forward modelling, and implications for hydrocarbon migration, <i>Tectonophysics</i> , Volume 630,2014,Pages 222-235,ISSN 0040-1951.
amusing.com	https://www.amusingplanet.com/2019/03/salt-domes-and-salt-glaciers-of-iran.html
lpi.usra.edu	https://www.lpi.usra.edu/publications/slidesets/geology/sgeo/slide_19.html
(earthobservatory.nasa)	https://earthobservatory.nasa.gov/images/6465/salt-dome-in-the-zagros-mountains-iran
S. Lord, 2018	S. Lord, A. (n.d.). Diapirs and Salt Domes The Mechanism of Formation. <i>Sandia National Laboratories</i> ,SAND2015-2018C.
Bosák, P. (1998).	Bosák, P. (1998). Salt Plugs in the Eastern Zagros, Iran: Results of Regional Geological Reconnaissance. <i>Geological Institute, Academy of Sciences of the Czech Republic</i> , ISSN 1210-9606.
Usgs.gov	Landsat missions
gcos.wmo.int	https://gcos.wmo.int/en/essential-climate-variables/land-temperature
Remss.com	http://www.remss.com/measurements/brightness-temperature/
Un-spider.org	https://un-spider.org/node/10958
l3harrisgeospatial.com	https://www.l3harrisgeospatial.com/docs/BANDPASS_FILTER.html

Osmanoğlu,2016 Batuhan Osmanoğlu, Filiz Sunar, Shimon Wdowinski, Enrique Cabral-Cano, Time series analysis of InSAR data: Methods and trends, ISPRS Journal of Photogrammetry and Remote Sensing, Volume 115, 2016, Pages 90-102,ISSN 0924-2716.